Synthesis of Polymer Matrix Nanocomposites using Thermal and Optical Methods: Understanding and Controlling Nanoparticle Formation in Polymer Matrices

by

Fan W. Zeng

A dissertation submitted to The Johns Hopkins University in conformity with the requirements for the degree of Doctor of Philosophy.

Baltimore, Maryland

October, 2018

Abstract

Synthesizing polymer matrix nanocomposites (PMNCs) in a scalable way can be challenging since scaling-up the production requires stable and homogeneous reaction environments to ensure uniform quality of the nanomaterials. As a result, production of PMNCs from laboratory scale to industrial scale usually involves additional processing steps, leading to high cost of manufacturing. In this study, we focus on unique processing methodologies that have the potential for scalable processing of functional PMNCs and seek to understand the physical and chemical processes underlying the synthesis of the PMNC systems. A thermal processing technique termed chemical infusion was used to produce various metal and metal oxide nanoparticles inside the polymer matrices. The essential processing steps begin by vaporizing a chemical precursor so that the precursor can molecularly diffuse into a solid polymer matrix. Once in the matrix, the precursor is made to decompose thermally resulting in formation of nanoparticles. This chemical infusion synthesis method was studied using various characterization techniques to gain insight into the diffusion process as well as the particle nucleation and growth mechanisms. Optically-based methods were also in-

corporated to actively control the location, size, number density, and composition of the nanoparticles formed in the polymer matrix. Both linear and non-linear optical processing methods are presented, and the related photo-induced mechanisms are discussed. Having established the necessary knowledge base for both the thermal and optical processing methods, chemochromic PMNCs were synthesized to demonstrate the feasibility of applying these methods to create multifunctional nanocomposites. Study results suggest that it is possible to create unique particle systems on a micro scale as well as on a nano scale within a polymer composite, resulting in materials with desired physical, chemical, and optical properties.

Primary Reader: Prof. James B. Spicer

Secondary Reader: Prof. Howard Katz

Acknowledgments

I would like to first thank Professors Michael Bevan, Howard Katz, Sara Thoi, Susanna Thon, and Jim Spicer for serving on my thesis committee. I am thankful to my advisor, Prof. Jim Spicer, for believing in a kid from a small school, giving me various challenging opportunities, encouraging me to strive for greatness, and supporting me for the past five years.

I would also like to thank Dr. Dajie Zhang for giving me constructive suggestions and guidance in this project. I would like to thank Dr. Michael McCaffery for teaching me Microtome sectioning and TEM imaging. I would like to thank Dr. Ken Livi for acquiring the STEM micrographs in this dissertation.

I would like to thank all the students/interns that worked with me before for helping out in the lab. I would like to thank all my lab mates and my friends in the materials science department (especially Lauren, Bernard and Qingjie) for helping me and encouraging me during my time at Hopkins. I would also like to thank all my basketball teammates for playing the game that I love with me. I enjoyed every moment on and off the court.

I want to thank my parents Qing Zeng and Jin Lu. I wouldn't be the man I am

today without your love and support, and for that I am forever grateful. I hope I have made you guys proud.

Lastly, I want to dedicate this dissertation to my wife Dihui and our daughter Bella. Grad school is tough, and creating a family during school sure doesn't make it easier. Somehow, someway, I made it through. Dihui, we had some tough times, but I know for a fact that I wouldn't be able to do this without your love, support, and belief in me. I cannot thank you enough for all your sacrifices, and more importantly, for giving us the most beautiful thing on earth, Bella. Bella, you are a distraction but also my motivation. I love you and your mama, and always will. By the way, Bella, if you are reading this, I want to let you know that you broke your leg a day before my thesis defense. If this is the way for you to say good luck, you might have taken it too literally.

Contents

List of Figures

List of Tables

Chapter 1

Introduction

1.1 Background and Motivation

Polymer matrix nanocomposites (PMNCs) are multiphase materials consisting of a continuous phase made from a polymeric material and one or more nanoscale phases dispersed in the polymer matrix. The properties of PMNCs depend on the properties of the constituent phases, their relative amounts, and their distributions. In many cases, the main purpose of the continuous phase is to protect the dispersed phases from undesired environments and to provide underlying support for nanoparticles or other nanoscale structures. The chemical and optical behaviors of the embedded nanostructures determine the functionalities of PMNCs so long as the polymer matrix allows proper access to the nanocomponents. For example, nanoparticles that are designed to undergo certain photochemical reactions would be most appropriate in an optically-transparent polymer matrix. The use of nanostructures in a polymer can provide high performance materials that find applications in diverse fields, such

as automobiles, aerospace components, sporting goods, and packaging [8–12]. For each application, nanomaterials with specific properties require a thorough design and a way to incorporate them into the polymer matrix. There are two preparation methods that have been used generally for synthesis of PMNCs [13–15]: (1) physical methods that involve direct melt and mixing processing of a filler with a polymer (melt compounding and film casting), (2) chemical methods that incorporate a filler or a filler precursor into monomers of a polymer matrix followed by polymerization (*in-situ* polymerization and *in-situ* sol-gel polymerization). These processes can be complicated by nanoparticle aggregation which could cause a change in the intended functionality of the nanoparticles. To reduce the force of attraction among nanoparticles, coating the nanoparticles with a chemical surfactant is usually included among the processing steps [16]. Although these synthesis methods have proven successful in a range of nanocomposite systems, the processing requirements do not scale easily or could result in undesirable performance. For example, the presence of the surfactant at the particle-matrix interface could alter the electromagnetic/optical behavior of the material [17]. Vapor phase co-deposition processes [18–20] can also be used to produce PMNCs, but they are relatively expensive and again only a small amount of material can be produced.

The essential process used in this study is a thermal synthesis method termed chemical infusion that forms nanoparticles inside a polymer matrix and can be scaled to produce large quantities of materials with uniform quality [21]. This process differs

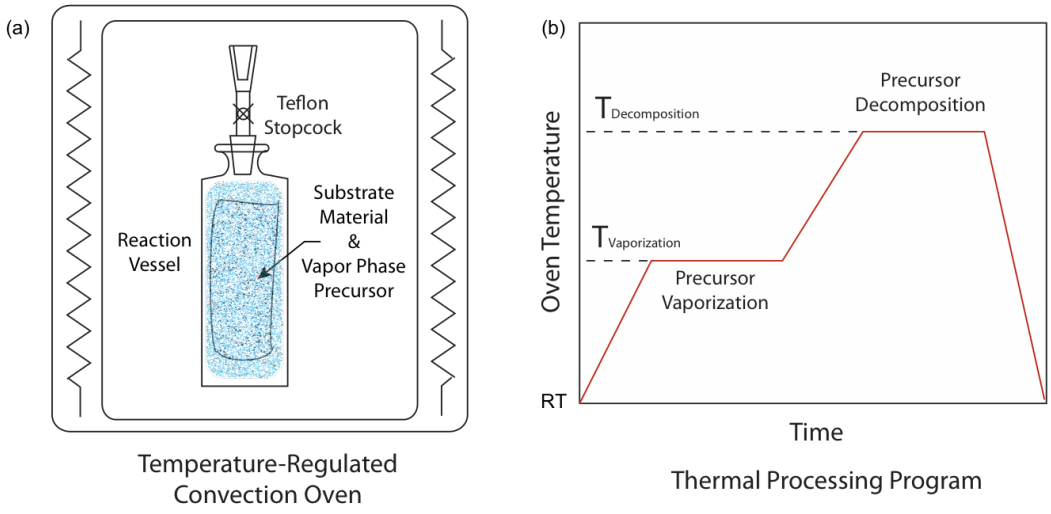

Figure 1.1: (a) A sschematic of the chemical infusion thermal processing and (b) a thermal processing heating program.

from the traditional approaches since nanoparticles are grown in a fully-formed solid polymer matrix such that net-shape materials can be processed into nanocomposites with desirable physiochemical properties. The main processing steps include placing the polymer matrix along with a particle-precursor chemical in a vacuum reaction vessel, heating up the vessel to a desired temperature so that the precursor vaporizes and diffuses into the solid polymer matrix, and increasing the temperature so that the precursor molecules decompose and produce species that form nanoparticles. Figure 1.1 (a) shows a schematic of the experiment, and Fig. 1.1 (b) displays a typical heating schedule. The actual experimental setup is shown in Fig. 1.2. A cold trap is submerged in a 4 liter Dewar filled with liquid nitrogen. The cold trap is attached to a rotary vane vacuum pump at one end, and it is connected to a Schlenk line at the other. The reaction vessel is attached to the Schlenk line with a reducing adapter

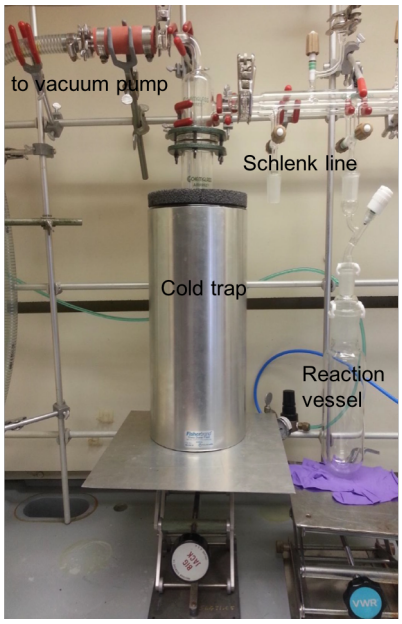

Figure 1.2: Experimental setup for the chemical infusion process.

that also has a valve to seal the reaction vessel. The reaction vessel consists of a reducing adapter and a glass vessel sealed together with Krytox high temperature vacuum grease. Once the reaction vessel is evacuated, it is sealed and removed from the Schlenk line and subsequently placed in a convection oven.

This processing technique has been demonstrated in a variety of simple systems. Figure 1.3 (a), (b), and (c) show transmission electron microscopy images of silver [1, 22], tungsten oxide [2], and palladium nanoparticles embedding in fluoropolymer matrices, respectively. Their corresponding optical images are also shown. The resulting PMNCs generally contain non-aggregated nanoparticles dispersed throughout the bulk of the polymer matrix and this is achieved without the use of any surfactants. In the case of tungsten oxide-polymer matrix nanocomposites (Fig. 1.2 (b)), the resulting materials are photochromic which automatically darken when ex-

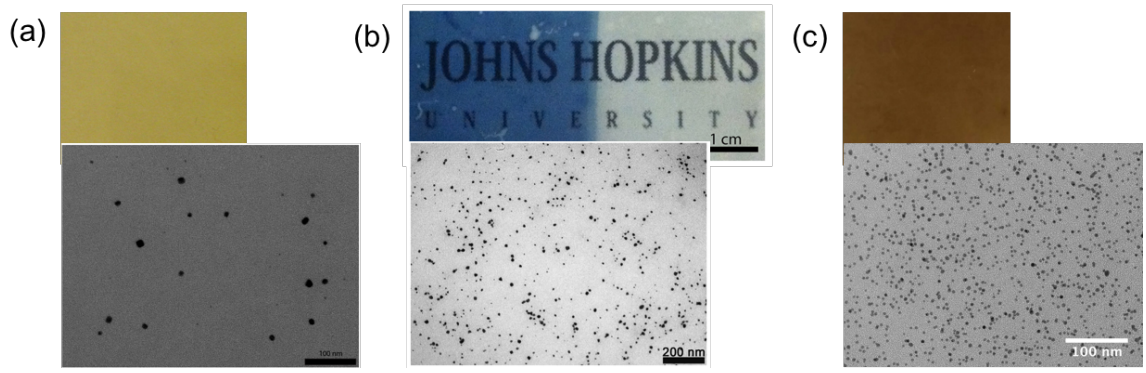

Figure 1.3: Optical images as well as transmission electron micrographs of (a) silver nanoparticles in hexaflouropropylene-co-tetraflouroethylene (FEP) [1], (b) tungsten oxide nanoparticle in FEP [2], and (c) palladium nanoparticles in poly-tetrafluoroethylene-co-(perfluoropropyl vinyl ether) (PFA).

posed to ultraviolet light. While the chemical infusion technique has the potential to produce multi-functional PMNCs in a commercially-viable and scalable way, the underlying physics and the limitations of this synthesis process are poorly understood. This type of understanding is a critical prerequisite for designing and producing PMNC materials with desired properties. In addition to the chemical infusion method, alternative processing techniques are required to actively control the particle chemistry and spatial variations inside the polymer matrix so that multifunctional materials containing hierarchical particle structures over various length scales can be created. These advanced particle control techniques could potentially be achieved by combining the chemical infusion technique with optical methods, but again, the photoinduced mechanisms and related phenomena are not well-understood.

1.2 Study outline

The first half of the thesis focuses on characterization and interpretation of the physical and chemical processes involved in the chemical infusion method. In Chapter 2, the effect of polymer structure on precursor diffusion is investigated by comparing the diffusion behavior of the precursor molecules in the as-received polymer as well as in a heat-treated polymer matrix. Results from the diffusivity measurements are described using a free volume diffusion model to gain a physical and conceptual understanding of precursor diffusion in polymers. In Chapter 3, the formation of nanoparticles is studied using transmission electron microscopy along with selective area electron diffraction to gain insight into the nucleation and growth processes. The nucleation of nanoparticles is correlated with defects in the polymer matrix, and the nanoparticle growth is interpreted using a modified diffusion-limited growth model. In addition, the effect of processing temperature on particle formation is also discussed.

The second half of the thesis focuses on using optical methods to actively control the synthesis of particles permitting the formation of particles with varying chemical composition and geometries. In Chapter 4, the modification of nanoparticle size and number density in polymer matrix nanocomposites is demonstrated using continuous wave (CW) laser irradiation. Optical excitation of nanocomposites containing nanoparticles and precursor results in decomposition of the precursor and subsequent particle modification as well as particle formation. The photo-induced chemical re-

actions are investigated under different background temperatures and pressures, and the results are used to identify the main mechanisms for CW laser-induced precursor decomposition. In Chapter 5, femtosecond pulsed laser is used at room temperature to locally produce multi-component particles with specific properties. Spatial variations in particle chemistries are achieved by decomposing the precursor in the close vicinity of the particles. These particle modification processes are described by considering the particle-mediated interactions between the nanoparticles and the precursor.

Having established the necessary knowledge base for both the thermal processing method and the optical processing methods, Chapter 6 briefly illustrates the synthesis and performance of various functional polymer matrix nanocomposites. In particular, chemochromic polymer matrix nanocomposites are synthesized. Optical gas sensors are presented for the detection of alcohol vapors as well as hydrogen gas. In addition, laser patterning of functional polymer matrix nanocomposites is demonstrated using a feasible patterning setup, presenting the opportunity to produce patterned materials with spatially varying properties.

Chapter 2

Effect of Polymer Structure on Precursor Diffusion and Particle Formation in Polymer Matrix Nanocomposites

2.1 Introduction

Most polymers consist of both crystalline and amorphous phases, and gas diffusion in semi-crystalline polymers has been studied extensively. In general, gas diffusion in a semi-crystalline polymer has two parts—diffusion in the crystalline phase as well as in the amorphous phase [23]. Gas diffusion in the crystalline phase is often neglected owing to the high polymer chain density in crystallites which obstructs the diffusion process. However, chain defect/disorder (such as row-vacancy defects) can occur within the crystalline region, and small gas molecules can penetrate through these regions if the defects are interconnected and are immobilized within the crystalline phase [24, 25]. For large diffusants, such as organometallic precursor species, the

diffusion pathway should reside in the low density amorphous region, where the free volume is relatively high [26, 27]—free volume describes the difference between the specific volume and the specific volume of the crystalline phase [28–30]. Generally, gas molecules will avoid the relatively impenetrable crystallites and diffuse through amorphous regions of relatively high free volume, and could, as a result, follow a tortuous diffusion pathway through the polymer [31]. It has been shown that high gas transport parameters relate to high free volume in polymers [32,33]. In theory, the amorphous region can be further divided into two parts: a rigid amorphous fraction (RAF) and a mobile amorphous fraction (MAF). While the MAF corresponds to the classical representation of polymer chains randomly arranged in space, the RAF is associated with the interface between the crystalline and the mobile amorphous phases [34–38]. Gas molecules can diffuse in the RAF and MAF regions, but the preferential diffusion pathway is unclear. By changing the crystallinity and morphology of a semi-crystalline polymer, and thereby the free volume of the polymer, the transport of precursor molecules in polymers of various structures can be compared and studied. Furthermore, particle formation is closely related to the diffusion of precursor species since the distribution of precursor determines where the particles can form in the polymer matrix. If the precursor transport pathways are indeed related to the free volume of the polymer, the resulting nanoparticle size distribution should be related to the free volume distribution of the polymer.

For the work presented here, a semi-crystalline fluoropolymer and a palladium

organometallic precursor were used to study the effect of polymer structure on precursor diffusion and nanoparticle formation. The polymer matrix was heat-treated to change its degree of crystallinity, and the diffusion behaviors of the palladium precursor molecules in the as-received and heat-treated polymers were analyzed and compared using a free volume diffusion model. In addition, palladium nanoparticles were grown in both the as-received and the annealed fluoropolymers, and the size distribution as well as the spatial distribution of the nanoparticles in these nanocomposites were studied.

2.2 Experimental

2.2.1 Materials

Palladium(II) acetylacetonate ($Pd(acac)_2$; 99% Pd; Sigma-Aldrich) was used as the precursor since it has a low decomposition temperature and it has been studied extensively for various deposition processes [39, 40]. Poly[tetrafluoroethylene-co-(perfluoropropyl vinyl ether)] (PFA; CS Hyde) copolymer was chosen as the matrix because this semi-crystalline polymer is chemically inert and has good thermal stability for temperatures up to 583 K. It is well known that annealing of a polymer can alter polymer crystallinity and morphology without changing its composition [41–44]. At the annealing temperature, the polymer chains are flexible enough to interact, re-align, and re-organize; crystallites can nucleate and grow and existing crystals can

thicken [42]. Two PFA films were heat-treated at 413 and 553 K ($PFA^{413\,K}$ and $PFA^{553\,K}$) for 24 hours and cooled slowly. The optical transparency of the films did not change as a result of the heat treatments.

Synthesis of palladium nanocomposites began by placing a $50 \times 100 \times 0.127$ mm^3 (measured using a micrometer caliper) as-received film (PFA) or a heat-treated film (PFA^{HT}) in a glass reaction vessel (1 L) along with ∼30 mg of $Pd(acac)_2$. The vessel was evacuated to ∼160 mTorr to remove air from the vessel as well as any volatiles present in the polymer matrix. The reaction vessel was transferred to an oven and heated to 413 K for 2 hours to sublime/vaporize the precursor and allow the precursor to diffuse into the polymer. The temperature of the vessel was then raised to 473 K and held for 2 hours to induce precursor decomposition followed by nanoparticle formation. The resulting materials are designated as Pd-PFA and Pd-PFA^{HT}. It should be noted that the volume percentage of palladium was less than 0.1% for a single infusion cycle.

2.2.2 Characterization

2.2.2.1 Thermal analysis

Dynamic mechanical thermal analysis (DMTA) was performed using a modular compact rheometer (Anton Paar MCR 302) over the temperature range 298 – 473 K. $10 \times 10 \times 0.127$ mm^3 samples were cut from the PFA and PFA^{HT} films. An amplitude sweep was carried out to determine the limit of the linear viscoelastic region, which

occurred at a strain of 0.1%. Parallel plates were used with a static force of 25 N at a frequency of 1 Hz.

Differential scanning calorimetry (DSC) was performed using a DSC Q20 apparatus (TA Instruments) in the temperature range from 315 to 673 K. All runs were performed on 3 ± 0.2 mg PFA and PFA^{HT} samples sealed in a nonhermetic aluminum holder under a nitrogen atmosphere. The mass of the samples were measured before and after analysis. Negligible mass loss ($< 1\%$) was found in all cases and was disregarded for the calculation of the heat of fusion. The degree of crystallinity was calculated according to the following equation:

$$Crystallinity(\%) = \frac{\Delta H_f}{\Delta H_0} \times 100 \tag{2.1}$$

where ΔH_0 is the reference value of heat of fusion for 100% crystalline polymer and ΔH_f is the heat of fusion determined from the area of the DSC melting peak [45].

2.2.2.2 X-ray diffraction

X-ray diffraction (XRD) data for PFA and PFA^{HT} were collected with a θ-2θ diffractometer (Philips X'Pert Pro MRD equipped with a Cu Kα X-ray source). The crystalline and amorphous peak details, such as location and width, were analyzed using standard software (MDI JADE). In addition, using a smaller X-ray spot size, XRD measurements were performed on different regions of Pd-PFA^{HT} nanocomposites to analyze the variation of crystallinity across the heat-treated polymer.

2.2.2.3 Transmission electron microscopy

Palladium nanocomposites were characterized using transmission electron microscopy (TEM) to determine particle size, particle distribution, and average particle number density. Cross sections for TEM imaging were prepared using diamond microtome methods. Samples were then mounted on copper grids and imaged on a transmission electron microscope (100 kV Philips EM 420). Standard software (ImageJ) was used to analyze the micrographs to determine particle polydispersity.

2.2.3 Measurement of precursor diffusion

A non-isothermal, desorption method [46] was combined with thermogravimetric analysis (TGA) to determine the diffusion coefficient of $Pd(acac)_2$ in PFA. In a typical experiment, a reaction vessel containing as-received and heat-treated PFA films (0.127 mm thick and 3 mm in diameter) as well as $Pd(acac)_2$ powder was first evacuated. The vessel was then heated to 413 K for 24 hours in order to fully saturate the films with precursor molecules. The samples were cleaned and were weighed before and after the saturation procedure using the high-precision scale in the thermogravimetric analyzer (SDT Q600 TA Instruments), where the lower limit of balance sensitivity for the instrument was approximately 0.1 μg. The average equilibrium precursor uptake was determined to be $\sim$15 μg per 3 mg of PFA. Thermogravimetric analysis was performed on the precursor saturated samples and on an as-received PFA sample (as a control) under argon atmosphere. Single heating curves were obtained at a constant heating

rate of 2 K/min over a temperature range of 303-413 K. All measurements were done below 413 K in order to avoid thermal decomposition of precursor, which occurs when temperature is above 443 K. The mass loss from the TGA results represents precursor desorption at various temperatures since neither PFA decomposition nor precursor decomposition occurred in the temperature range of 303 to 413 K.

Analyzing diffusion with mass transfer requires assuming that changes in diffusant concentration occur near the system's boundaries [47]. The precursor molecules and polymer are well-mixed, except near the polymer-air interface. The driving force for precursor desorption is generated by gradients in precursor concentration over such a phase boundary. Various fluoropolymers (including PFA) exhibit Fickian behavior [48, 49], so it is reasonable to assume the distribution of precursor concentration in the PFA samples follows Fick's law. Based on these appropriate assumptions, the diffusion coefficients can be expressed as follows [46],

$$D(T) = \frac{\pi}{8}\frac{h^2}{M_\infty^2}M(T)\frac{dM(T)}{dT}\frac{dT}{dt} \tag{2.2}$$

where h is the thickness of polymer films, M_∞ is the equilibrium precursor uptake of the PFA sample, $M(T)$ is the quantity of precursor desorbed at temperature T, and t is time. This equation allows us to calculate the temperature dependence of the diffusion coefficient using the mass loss results. For the type of processing that is being used in this study, mass transfer partly occurs under non-isothermal conditions, so

the diffusion coefficients obtained from the non-isothermal method can be adequately used in simulations of the overall process.

2.3 Results and discussion

2.3.1 Thermal and structural properties of PFA

The glass transition temperature (T_g) of PFA was taken from the maximum in tan δ measured using DMTA (Fig. 2.1). The maximum occurs at 372 K, which is in good agreement with the literature value of 363 K [3]. Annealing of PFA did not have a significant impact on T_g since the maximum peaks of the tan δ for the heat-treated PFA films were found near 372 $\pm$1 K. Typical DSC results for the PFA samples are shown in Fig. 2.2, where the melting point as well as the heat of fusion can be clearly defined and determined. The melting temperature is approximately 583 K, and this

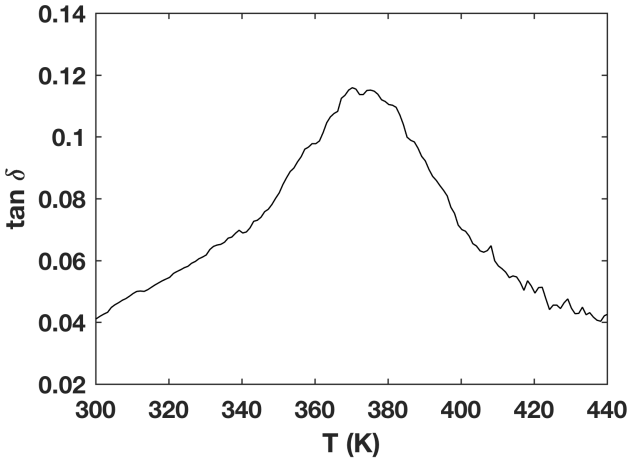

Figure 2.1: DMTA of PFA. Tan δ as a function of temperature.

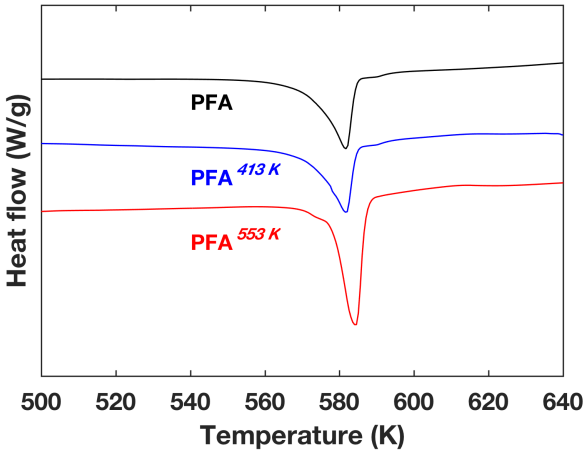

Figure 2.2: DSC scans of as-received, 413 K heat-treated, and 553 K heat-treated PFA. Results are shown offset for clarity.

value is in good agreement with the literature value of 599 K [50]. In addition to the main endotherm at 583 K, there is a shoulder at ∼573 K which could be attributed to melting of imperfect crystals in the polymer. Using Eq. (2.1) along with the measured ΔH_f values and $\Delta H_0 = 82$ J/g [50, 51], the percent crystallinity of the as-received PFA, PFA$^{413\,K}$, and PFA$^{553\,K}$ were 24.1%, 24.9%, 34.3%, respectively. Annealing PFA at 413 K did not seem to affect the percent crystallinity as much as annealing at 553 K for the dwell time used in this study. Higher annealing temperatures and longer annealing times might result in higher PFA crystallinity, but this was not the focus of this study.

The XRD results obtained for the PFA samples are shown in Fig. 2.3. Broad amorphous peaks centered at 2θ ∼16° and 38° were observed for all PFA samples. While the 38° peak can be easily seen in the inset of Fig. 2.3, the 16° peak corresponds to the tail on the left side of the most intense peak. There were no obvious changes

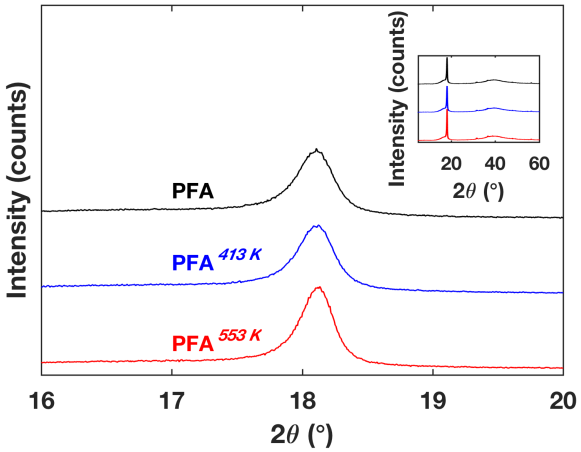

Figure 2.3: X-ray diffraction results showing the crystalline peaks of as-received, 413 K heat-treated, and 553 K heat-treated PFA. Inset figure depicts the entire XRD scan. The scans are offset for clarity.

to the widths or location of the amorphous peaks after annealing. The reflection at approximately $2\theta = 18.1°$ is associated with scattering by the (200) plane in the quasi-hexagonal crystal of PFA [52, 53]. This crystalline peak did not shift any after the heat treatment. However, the full width at half maximum (FWHM) of $PFA^{553\,K}$ was narrower than that for as-received PFA or for $PFA^{413\,K}$. The increase in FWHM corresponds to a 9% increase in crystallite dimensions of PFA calculated using the Scherrer equation [54]. This result is in good agreement with the increase of crystallinty observed previously from the DSC results.

2.3.2 Precursor diffusion study

The fractional crystallinity and the distribution of the crystallites in the polymer directly affect its gas permeability (which is the product of its sorption coefficient

and diffusion coefficient) [55–57]. The $Pd(acac)_2$ desorption results for PFA and for $PFA^{553\,K}$ ($Pd(acac)_2$-PFA and $Pd(acac)_2$-$PFA^{553\,K}$ respectively) are shown in the TGA curve (Fig. 2.4 (a)), where the ratio of the mass-loss (M) to the initial sample mass (M_0) is plotted against temperature. $PFA^{413\,K}$ was not used in the diffusion study since its crystallinity was similar to that of as-received PFA. The desorption result for as-received PFA film was included in the figure and treated as a baseline for the other two desorption results to identify effects related to the base polymer (such as sample size and humidity). The results show that the rate of mass-loss in $Pd(acac)_2$-$PFA^{553\,K}$ was much higher than that for $Pd(acac)_2$-PFA. At ∼328 K, the desorption data for $Pd(acac)_2$-PFA and for $Pd(acac)_2$-$PFA^{553\,K}$ deviate from the baseline indicating loss of absorbed $Pd(acac)_2$. At ∼373 K, the desorption process stopped because either complete desorption had occurred or any remaining precursor molecules were trapped in the polymer. Using the mass-loss data along with Eq. (2.2), the diffusion coefficients at various temperatures were obtained and are given in Fig. 2.4 (b). The diffusivity of $Pd(acac)_2$ in PFA appears to fluctuate more than that in $PFA^{553\,K}$, especially in a temperature range from 340 K to 355 K. This is because mass loss for $Pd(acac)_2$-PFA in this temperature range is minimal, resulting in a noisy appearance.

Gas diffusivity in polymers generally decreases as the crystallinity increases since transport through crystallites is low and their presence in the polymer tends to increase the tortuosity of the transport path in adjoining amorphous regions. However,

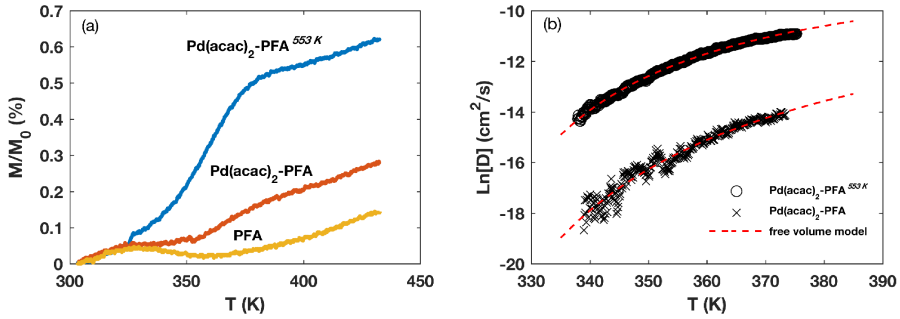

Figure 2.4: (a) TGA showing mass losses for $Pd(acac)_2$-infused PFA and $Pd(acac)_2$-infused $PFA^{553\,K}$; mass loss for as-received PFA film is provided for baseline correction. (b) Computed diffusion coefficients based on mass loss measurements along with theoretical fits using the free volume model (dashed line).

higher precursor diffusivity was found in the annealed PFA compared to the as-received PFA. While other authors have indicated that the gas diffusivity in PFA is independent of crystallinity [58], our results indicate a dependence on crystallinity. We will attempt to interpret these results with a free volume diffusion model, which also provides insight into the particle formation process.

2.3.2.1 Free volume model

The free volume model assumes diffusion occurs as a result of thermally-activated redistribution of free volume in a polymer matrix and is based on the work by Cohen and Turnbull who suggested that the rate of diffusion is directly proportional to the probability of finding a sufficiently accessible region adjacent to the diffusing molecule [59]. Fujita [60] took a similar approach and developed a free volume model

Table 2.1: Fitting Parameters and Correlation Coefficients for Free Volume Model Fit to Diffusion Measurements

System	$b\,(\mathrm{cm}^2/\mathrm{J}\cdot\,\mathrm{s})$	c	$\alpha\,(\mathrm{K}^{-1})$	$T_g\,(\mathrm{K})$	$f(T_g)$	R-squared
$Pd(acac)_2$-PFA	6.33×10^{-8}	0.362	8.14×10^{-4}	369	0.063	0.957
$Pd(acac)_2$-$PFA^{553\,K}$	1.53×10^{-7}	0.217	9.48×10^{-4}	372	0.065	0.997

that relates the diffusivity, D, to the fractional free volume, f, as follows:

$$D(T) = bRTexp[-c/f] \tag{2.3}$$

where b and c are characteristic parameters for a polymer-diffusant system, and R is the gas constant. It is widely accepted that the fractional free volume is linearly proportional to temperature and is given by

$$f(T) = f(T_g) + \alpha(T - T_g) \tag{2.4}$$

where $f(T_g)$ is the fractional free volume of the polymer matrix at T_g, and $\alpha = \alpha_l - \alpha_g$ is the difference of free volume expansion coefficients above and below T_g [61–63]. Combining Eq. (2.3) and Eq. (2.4) yields a model that can be used to interpret diffusion data, and the results are shown in Fig. 2.4 (b). Using a least-squares fitting method, the free volume model appears to agree well with measured results. The model parameters for the curve fits are given in Table 2.1.

The T_g values from the model agree well with the measured ones (372 K). While the DMTA data indicated that T_g of PFA did not change after heat treatment, the

free volume model suggests a small increase in T_g for the 553 K treated PFA. The fractional free volumes at T_g were found to be 0.063 and 0.065 for PFA and PFA$^{553\,K}$, respectively. These values are in general agreement with the fractional free volume reported by other authors, who have shown that $f(T_g)$ increased from 0.02 for polymers with $T_g = 200$ K to ∼0.08 for polymers with $T_g = 400$ K [64,65]. The fractional free volume of PFA$^{553\,K}$ is larger than that of PFA at T_g and at $T > T_g$ since the free volume expansion coefficient of PFA$^{553\,K}$ is larger. This result could be related to the re-distribution of crystalline regions that might constrain surrounding amorphous material and result in freer movement of polymer chains in these regions [43]. Cheng and Sun observed similar behavior in a different semi-crystalline polymer system using positron annihilation lifetime spectroscopy (PALS) where an increase in free volume and free volume expansion coefficient occurred after heat treatment [66]. Also, it should be noted that the results obtained here for fractional free volume and free volume expansion coefficient are comparable to those obtained by other groups using PALS [62, 63, 67].

The free volume size is another important characteristic of polymers and affects molecule transport. The average size of a free volume cavity, $\langle v \rangle$, is directly proportional to f and is given by

$$\langle v \rangle = \frac{f(T)}{N_h} \tag{2.5}$$

where N_h is the number density of free volume cavities. At 413 K, which was the temperature used in the precursor saturation process, f was calculated to be 9.6%

and 10.4% respectively for PFA and PFA$^{553\,K}$ using the free volume model. Dlubek estimated the free volume number density of PFA to be 0.27 nm^{-3} using PALS [62] and claimed that N_h is independent of temperature [63]. Using Eq. (2.5) and letting $N_h = 0.27$ nm^{-3}, $\langle v \rangle$ can be estimated to be 0.36 nm^3 for PFA and 0.39 nm^3 for PFA$^{553\,K}$. If the free volume cavities are spherical, the average diameter would be 0.88 nm for PFA and 0.90 nm for PFA$^{553\,K}$. Comparing these values to the molecular size of Pd(acac)$_2$, ∼0.85 nm in length [68], indicates that the average free volume cavities of both PFA matrices are sufficiently large for the diffusion of Pd(acac)$_2$ molecules.

2.3.3 TEM analysis of palladium nanocomposites

Palladium nanocomposites were synthesized by decomposing the Pd(acac)$_2$ precursor in the polymer matrices. Both as-received PFA and heat-treated PFA were used and the resulting nanocomposites differed significantly from each other. Indeed, as illustrated in Fig. 2.5 (a) and (b), simple visual inspection shows differences between the Pd-PFA and Pd-PFA$^{553\,K}$ nanocomposites. While the Pd-PFA material has a uniform dark-brown color, Pd-PFA$^{553\,K}$ has randomly distributed dark-brown and light-brown regions with the differences corresponding to variations in palladium particle content. TEM imaging of dark-brown nanocomposite material (Fig. 2.5 (b) and region ϵ in Fig. 2.5 (a)) shows that particle number density is significantly higher than that of the light-brown nanocomposite material (region γ in Fig. 2.5 (a)), and

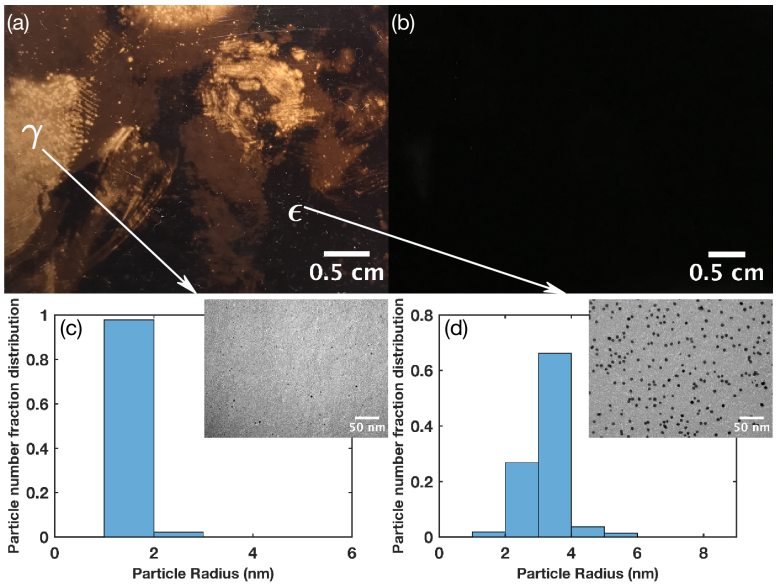

Figure 2.5: Optical reflection micrographs of (a) Pd-PFA$^{553\,K}$ and (b) Pd-PFA. Representative TEM images and their corresponding particle size distributions of (c) light-brown films and (d) dark-brown films.

the average radius of particles in the light-brown regions is about three times smaller than that of particles in the dark-brown material (Fig. 2.5 (c) and (d)).

Relatively low magnification TEM images of Pd-PFA were obtained in order to capture a large number of nanoparticles and use them to present an adequate particle size distribution. A representative low magnification TEM image of Pd-PFA is shown in Fig. 2.6 (a). The distribution of Pd nanoparticles is continuous from the material surface to the interior of the sample. These discrete particles, approximately spherical with radius from 1-8 nm, were well dispersed in the PFA matrix. Figure 2.6 (b) shows the particle size distribution. If nanoparticle formation is related to the free volume of the polymer, the resulting nanoparticle size distribution should somehow relate the free volume density function. It has been found that the free volume density function,

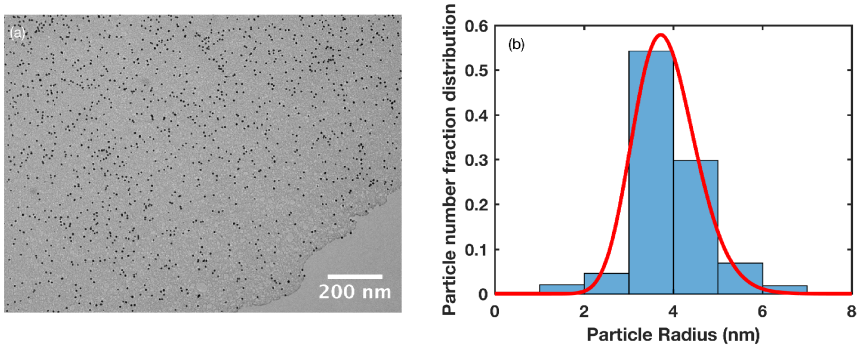

Figure 2.6: (a) TEM image of Pd-PFA (b) representative particle size distribution and its curve fit according to a modified free volume distribution function.

ζ, can be written as [62, 69–71]

$$\zeta(f) = \frac{\beta}{f_m \Gamma(\beta)} (\frac{\beta f}{f_m})^{\beta-1} exp(-\frac{\beta f}{f_m}) \tag{2.6}$$

where β is a parameter that relates to the mean fluctuations in free volume, f_m is the mean fractional free volume, and $\Gamma(\beta)$ is the gamma function [72, 73]. While the free volume distribution follows a gamma distribution, we notice that this also mutually describes the particle size distribution if we let $f = r$ and $f_m = r_{ave}$ (where r is the particle radius, and r_{ave} is the average particle radius). This modified function is identical to the Schuliz-Flory distribution function, which has been shown to describe the particle size distribution of many similar material systems [1,74–76]. The resulting fit is shown in Fig. 2.6 (b), and β, r_{ave}, and the correlation coefficient of the fit to the data were found to be 30.3, 3.8 nm, and 0.986 respectively. Note that a Gaussian function did not fit the data as well as the Schulz-Flory distribution function.

Even though the free volume distribution for the PFA used in this study was not measured, it is clear that particle size has a particular connection to free volume. A spherical Pd nanoparticle with a radius of 3.8 nm contains approximately 1.56×10^4 Pd atoms which are derived from the same number of precursor molecules as a result of decomposition. The average free volume cavity has a radius of 0.50 nm (based on the free volume model calculation for PFA at 473 K) and more than one precursor molecule occupies this volume. If each cavity contains six precursor molecules before decomposition occurs, then there needs to be more than 2.60×10^3 free volume cavities to accommodate 1.56×10^4 precursor molecules. Based on the average number density of free volume cavities in PFA ($N_h = 0.27$ nm^{-3}), these free volume cavities define a spherical region for particle formation that has a radius of 13.2 nm. This value is close to the average first neighbor shell distance of the nanoparticles, $\sim$13.7 nm. This distance was calculated by first performing Voronoi tessellation on the TEM micrographs and then equating the area of each Voronoi polygon to a circular region followed by averaging of the radii. This rough estimation indicates that the particle size distribution is mainly determined by the precursor distribution and hence the free volume distribution of the fluoropolymer—the particle size is controlled by the available free volume and the enclosed precursor molecules in the close proximity of a nucleation site.

Unlike Pd-PFA, the size distribution of Pd nanoparticles in Pd-PFA$^{553\,K}$ is not uniform throughout the bulk of the polymer matrix. While the particle size distri-

bution in the dark brown region of Pd-PFA$^{553\,K}$ is similar to that in Pd-PFA, the light brown region of Pd-PFA$^{553\,K}$ has low particle number density as well as small particle size (Fig. 2.5 (c)). The nonuniform structural change of the heat-treated PFA matrix likely contributed to the variation of particle density. To verify this, X-ray diffraction measurements were performed on the dark brown and light brown regions in Pd-PFA$^{553\,K}$ as well as on Pd-PFA, and the results are shown in Fig. 2.7. It should be noted that the volume fractions of palladium were too low for detection of diffraction from the palladium particles. Since the amorphous peaks for each sample are similar, the polymer crystallinity can be compared by measuring the area under the crystalline peaks ($2\theta = 18.1°$). Doing so indicates that the crystallinity of the dark brown region in Pd-PFA$^{553\,K}$ is similar to that of as-received PFA, and this result correlates with the corresponding particle densities observed in the TEM micrographs. The crystalline peak area for the light brown region is larger and this

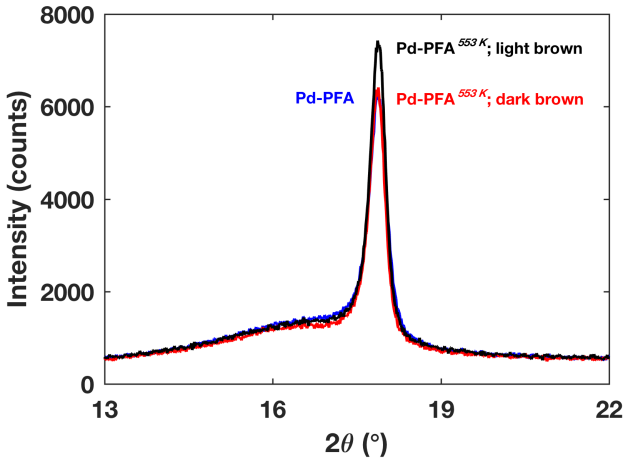

Figure 2.7: X-ray diffraction scan showing the crystalline peak for Pd-PFA as well as for the dark brown and light brown regions of Pd-PFA$^{553\,K}$.

indicates that crystallite size and spatial distribution were altered by annealing. The distribution of free volume ought to vary accordingly. While the free volume difference between the light brown and dark brown regions is unclear, the differences of the corresponding particle number density and particle size is significant. Based on the ideas developed here, the light brown region could have lower free volume and this would hinder precursor diffusion and would also limit the volume of precursor available for subsequent particle formation. However, since the precursor diffusion measurements tend to indicate that overall free volume in the annealed matrix is higher, the organization of crystalline and amorphous phases in the light brown regions must be altered in a way that enhances diffusion but inhibits particle formation. Also, this altered structural organization would impact the distribution of MAF and RAF and have a corresponding effect on the free volume [62] since RAF has higher free volume than MAF [37, 38].

2.4 Conclusion

A chemical infusion synthesis process was used to synthesize polymer matrix nanocomposites, and the effect of polymer structure on precursor diffusion and nanoparticle formation was investigated by changing the crystallinity of the polymer matrix. In particular, the diffusion of $Pd(acac)_2$ precursor and the formation of palladium nanoparticles in PFA and annealed PFA were studied. A free volume model was used to interpret the diffusion results, and the average free volume size was estimated to

be sufficiently large for the diffusion of $Pd(acac)_2$ molecules at the processing temperature. Transmission electron microscopy studies indicated that palladium particle size and spatial distributions in the as-received and annealed PFA matrices were significantly different. While monodisperse particle distribution was found in the as-received PFA matrix, nonuniform particle number density and size distribution were found across the annealed PFA matrix. The fact that both precursor diffusivity and particle formation changed as a result of modification of polymer structure indicates that particle size and spatial distribution are determined by the structure and morphology of the polymer matrix. We speculate that the particle size and size distribution are limited by the polymer free volume and the infused precursor.

Chapter 3

Palladium Nanoparticle Formation Processes in Fluoropolymers by Thermal Decomposition of Organometallic Precursors

3.1 Introduction

In the previous chapter, the structure of the polymer matrix was shown to have significant effects on precursor diffusion as well as particle formation. The connection between the precursor/particle size and the size of polymer free volume was demonstrated qualitatively based on the diffusion results, and we concluded that the formation of nanoparticles is determined by the infused precursor. However, these ideas require quantitative descriptions so that the nanoparticle formation mechanisms can be adequately interpreted. This chapter aims to provide a better understanding of the correlation between particles and polymer free volume as well as give a detailed interpretation of the particle nucleation and growth processes in the polymer matrix.

The formation of nanoparticles in polymer solutions has been studied in depth owing to the development of advanced characterization techniques, such as *in-situ* liquid cell transmission electron microscopy and time-resolved *in-situ* small angle X-ray scattering [77–79]. In general, nanoparticle synthesis in solutions can be described using the classical LaMer burst mechanism [80,81]. The LaMer mechanism is divided into three stages: (1) the solute species in solution are supersaturated but no particles are present; (2) the concentration of solute reaches a critical level of supersaturation that drives rapid nucleation which partially relieves supersaturation; (3) nanoparticle growth occurs by incorporation of the remaining solute—there is almost no additional nucleation. The growth process can continue through Oswald ripening [82] resulting in particle size dispersity, and the characteristic particle size distribution is described in the Lifshitz-Slyozov-Wagner (LSW) theory [83, 84]. At a later stage of the growth process, other particle growth phenomena can also occur, such as coalescence, orientated attachment, and intraparticle growth [85–88]. For synthesis of transition metal nanoparticles, a two-step mechanism, named Finke-Watzky mechanism, has been proposed [89]. The Finke-Watzky mechanism consists of slow continuous nucleation followed by autocatalytic surface growth ($A \rightarrow B$ followed by $A + B \rightarrow 2B$ where A is a general organometallic precursor and B is a nanocrystal). This mechanism has been shown to describe various nanoparticle systems, including platinum [90], iridium [91], and rhodium [92]. Similar to nanoparticle formation in solution, nanoparticle formation on the surface of a substrate via vapor deposition generally obeys the classical

theory of heterogeneous nucleation on defects, and particle growth is mainly governed by diffusion of adsorbed atoms. The degree of applicability of this classical approach depends on the size of the nuclei. For those involving large critical nuclei, it describes the nucleation and growth process well since the macroscopic thermodynamic properties can be appropriately assigned to the nuclei. For small critical nuclei, statistical mechanical models have been developed [93, 94] and validated experimentally for many material systems [95–99].

Although the chemical infusion technique used in this study is different from the wet chemistry or vapor deposition techniques in terms of synthesis procedures, we will show that its essential mechanism of nanoparticle formation can be interpreted by combining heterogeneous nucleation theory and various particle growth mechanisms. For the work presented in this study, palladium nanoparticles were grown in a semi-crystalline fluoropolymer using the chemical infusion technique, and the formation of palladium nanoparticles was studied by creating a series of samples that effectively captured particle size and distribution as a function of processing times and by analyzing these samples using transmission electron microscopy—imaging as well as selective area electron diffraction. Using related results, it is shown that the nucleation of nanoparticles can be connected to the free volume of polymer [100] and that the growth of the nanoparticles can be divided into four stages each with its own growth characteristics. Having established the essential aspects of the particle synthesis process, the effect of temperature as a processing variable on particle formation

can be interpreted to understand widely differing spatial distributions of particles in polymer matrices.

3.2 Experimental

3.2.1 Materials

Commercially available palladium(II) acetylacetonate ($Pd(acac)_2$; 99% Pd; Sigma-Aldrich) was used as a precursor for preparing palladium nanoparticles. The palladium precursor was used in its as-received state without further preparation. A semicrystalline poly[tetrafluoroethylene-co-(perfluoropropyl vinyl ether)] (PFA; CS Hyde) was chosen as the polymer matrix. The surfaces of the PFA films were cleaned with acetone and deionized water prior to synthesis.

3.2.2 Synthesis of Palladium nanocomposites

Palladium nanocomposites (designated as Pd-PFA) were synthesized using the chemical infusion technique. The synthesis process was started by placing a 60 $\times$ 100 $\times$ 0.127 mm^3 PFA film in a glass reaction vessel (1 L) along with $\sim$30 mg of $Pd(acac)_2$ powder dispersed around the inner wall of the vessel. The reaction vessel was evacuated to $\sim$160 mTorr in order to remove air from the vessel as well as volatiles from the PFA matrix. The vessel was heated in an oven for 2 hours at 140 °C to sublime/vaporize the $Pd(acac)_2$ precursor and allow the precursor to diffuse into the

PFA matrix. Owing to the process used to synthesize the nanocomposites, there was a large volume of palladium precursor placed on the wall of the reaction vessel, and the precursor must vaporize and be transported a significant distance (up to 20 mm) to reach the polymer. As a result, it is necessary to hold the reaction vessel at the vaporization temperature for an appropriate amount of time—two hours was determined to be adequate in this material system. The temperature of the oven was then raised to 180 °C (the lowest temperature at which the decomposition of $Pd(acac)_2$ could be observed) and held for 0.25, 0.5, 0.75, 1, 2, 6, and 8 hours to induce precursor decomposition followed by nanoparticle formation. The reaction vessel was quickly transferred to a room temperature environment in order to arrest the particle-formation-state in the sample—Pd-PFA is very stable structurally at room temperature and this can inhibit various growth processes from occurring. A series of 7 different Pd-PFA films with various dwell times for decomposition was used to study the nucleation and growth of Pd particles in PFA. A separate set of Pd-PFA was synthesized at relatively high temperatures (220 °C and 240 °C) and short processing time ($\sim$2 hours)—further particle growth was not observed after this processing time. The resulting nanocomposites were used to study the effect of temperature on particle formation.

3.2.3 Characterization

Transmission electron microscopy (TEM) images and selective area electron diffraction (SAED) patterns were obtained to provide particle size, particle distribution, average number density, and structural information about the Pd nanoparticles. Cross sectional samples ∼100 nm in thickness were prepared using diamond microtome methods. Samples were then mounted on copper grids and imaged on a 100 kV Philips EM 420 transmission electron microscope. The point-to-point resolution of the TEM was 0.33 nm. Standard software (ImageJ) was used to analyze the TEM micrographs. An Oxford energy dispersive X-ray spectroscopy (EDS) detector was used for the elemental analysis.

3.3 Results and discussion

3.3.1 Nucleation and free volume

Representative TEM micrographs illustrating a systematic time-sequence for nanoparticle formation are shown in Fig. 3.1. The energy dispersive X-ray spectroscopy analysis (inset of Fig. 3.1) indicates the presence of palladium, and the detection of fluorine comes from the PFA matrix. These palladium nanoparticles are approximately spherical, and the particle number density as well as particle size appear to increase as the processing time increases. The nanoparticle number density was measured from the TEM micrographs, and its variation with time at 180 °C is shown in

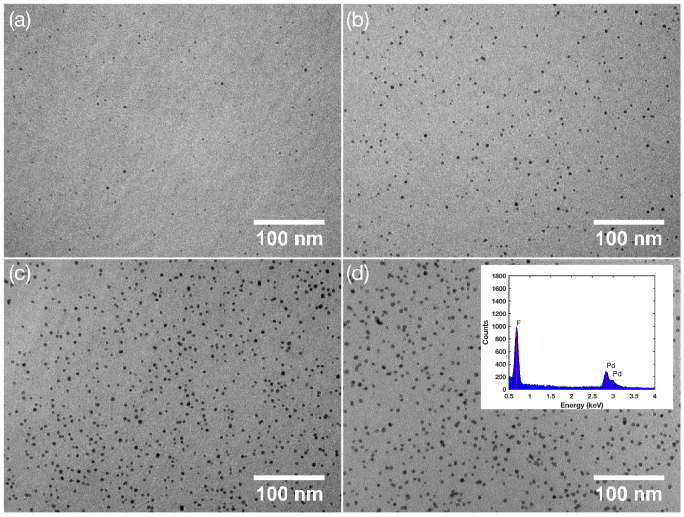

Figure 3.1: Representative TEM images of Pd-PFA processed at 180 °C with dwell time = (a) 0.25, (b) 0.5, (c) 2, and (d) 8 hours. The inset shows an EDS spectrum of Pd-PFA.

Fig. 3.2. Unlike the LaMer burst nucleation, in which the rate of nucleation is effectively infinite, the particle number density increases slowly over a period of about two hours. This slow nucleation can be attributed to the decomposition characteristics of $Pd(acac)_2$. The rate at which the palladium atoms arrive at the nucleation sites depends on the decomposition rate of the precursor and this will necessarily impact the nucleation process. The variation of particle number density in Fig. 3.2 can be best described by an exponential approach to a saturation value associated with a maximum particle number density. This is to be expected if a fixed and limited number of nucleation sites is present initially in the polymer. If the rate at which the

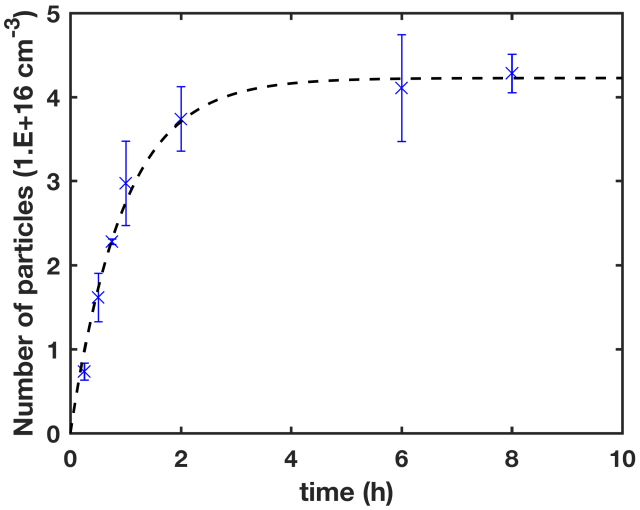

Figure 3.2: Average palladium particle number density at various dwell time for decomposition temperature of 180 °C. The error bars represent the overall distribution of the data. Dashed line represents the best fit to Eq. (3.2).

nucleation sites become occupied by particles is given by the following [95]:

$$\frac{dN}{dt} = \frac{I(N_0 - N)}{N_0} \tag{3.1}$$

where N is the number of sites occupied at time t, I is the nucleation rate, and N_0 is the maximum number of available sites, then the number of particles as a function of time is:

$$N = N_0 \left[1 - exp\left(-\frac{It}{N_0}\right)\right]. \tag{3.2}$$

Equation 3.2 can be used to fit the experimental results in Fig. 3.2 with the result shown where N_0 and I were taken to be 4.23×10^{16} cm^{-3} and 1.23×10^{13} cm$^{-3}s^{-1}$, respectively.

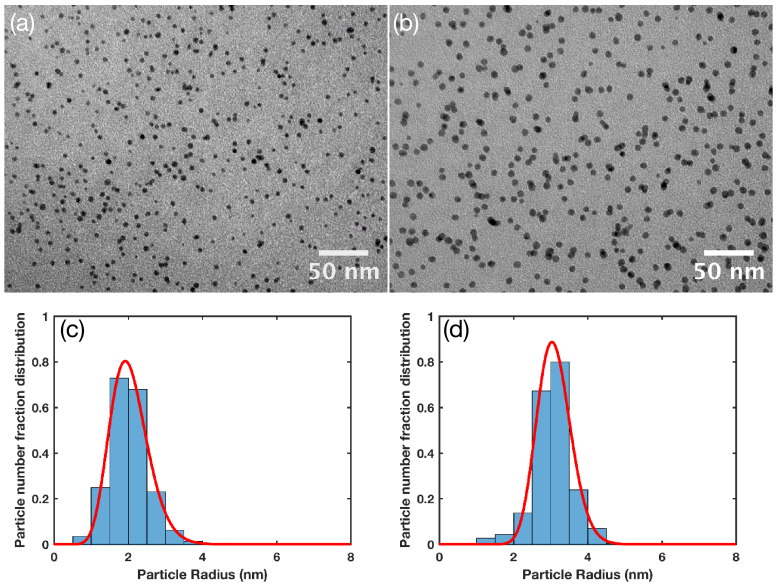

Figure 3.3: Representative TEM images of saturation concentration of Pd nanoparticles in PFA processed at (a) 180 °C for 8 hours and at (b) 220 °C for 2 hours; (c) and (d) showing their corresponding particle size distributions. Solid lines are curve fit based on Eq. (3.3).

Palladium nanocomposites were also synthesized at a relatively high temperature (220 °C), while keeping the other experimental conditions the same. Although the nucleation rate at this high processing temperature was not determined, it generally requires less time for the particle number density to reach its saturation level compared to materials processed at relatively low temperatures. The nucleation rate likely increases with temperature since the decomposition rate of the palladium precursor (and hence the incident rate of palladium atoms) also increases as temperature increases [39,40,95–97]. Figure 3.3 shows representative TEM images of Pd-PFA processed at 180 and at 220 °C as well as their corresponding particle size distributions (PSDs). The bin-width, $W = 0.5$ nm, was chosen based on Sturge's method [101] where $W = (R_{max} - R_{min})/(1 + log_2 M)$, R_{max} and R_{min} are the maximum and min-

imum particle radius and M is the number of particles. It should be noted that detection of particles less than 0.5 nm in radius was difficult owing to insufficient contrast between the background structure originating from the polymer matrix and any small particles that might be present. The radius of the nanoparticle ranges from 0.6 to 3.8 nm for Pd-PFA processed at 180 $°C$ and from 0.6 to 4.8 nm for materials processed at 220 °C. Neither a Gaussian nor a left-skewed distribution (which is a characteristic shape of the LSW theory for Ostwald ripening [102]) was found in any of the Pd-PFA samples. The Pd particle size distribution, $P(R)$, follows a model based on the Schulz-Flory distribution [74], which is given by

$$P(R) = \frac{z}{R_{ave}\Gamma(z)}(\frac{zR}{R_{ave}})^{z-1}exp(-\frac{zR}{R_{ave}}) \tag{3.3}$$

where R_{ave} is the average particle radius, and z is related to the particle polydispersity (pp) by $pp = z^{-1/2}$ and can be referred to as the width of the Schulz-Flory distribution [75]. This gamma distribution has been used in the previous chapter, and it was shown that there could be some correlation between particle size and polymer free volume. The PSDs were fit using a non-linear least squares curve fitting routine based on Eq. (3.3), and the results are shown in Fig. 3.3 (c) and (d). A one-sided Kolmogorov-Smirnov test was used to make goodness of fit analysis, and the results suggest that the Schulz-Flory gamma distribution fits the particle size distributions well. The values of z were determined to be 16 and 47, which correspond to polydispersity of 0.25 and 0.15, for material processed at 180 °C and at 220 °C, respectively. The average particle radius was determined to be 2.0 nm and 3.1 nm for Pd-PFA processed

at 180 °C and at 220 °C, respectively. Higher processing temperature resulted in larger nanoparticles. It appears that the precursor molecules do not all decompose instantaneously at the decomposition temperature (180 °C or 220 °C). The ones that have decomposed can nucleate and grow at the nearby nucleation sites, and the ones that have not yet decomposed continue the diffusion process until a concentration equilibrium is reached. More precursor molecules can dissolve in the PFA matrix at 220 °C than at 180 °C, which results in larger nanoparticles at higher temperature.

Regardless of the processing temperature, the Pd nanoparticles seem to form throughout the bulk of the polymer matrix. However, when considering heterogeneous nucleation, the preferred sites for nucleation should reside on the defects or imperfections in the polymer matrix with the result that the density of defects should somehow correlate with the apparent particle number density. The saturation particle number densities observed at different processing temperatures appear to be similar (Fig. 3.3 (a) and (b) contain approximately 450 and 375 nanoparticles, respectively) suggesting that particle nucleation possibly occurs on the existing defect sites in the PFA matrix.

Defects and imperfections in polymers have distinct definitions. For a semi-crystalline polymer, defects can be chain disorder in the crystalline region, interface between the crystalline and amorphous regions, and poor chain packing with voids in the amorphous region. These defects can be related to the free volume of the polymer. In particular, Spaepen has proposed that the fraction of defect sites, n, in a system

can be determined via a relation of the form [100]:

$$n = \Delta f exp\left(-\frac{\gamma v}{v_f}\right) \tag{3.4}$$

where Δf is the fraction of the sample volume in which potential defect sites can be found, γ is a geometrical factor that takes into account the overlap between the neighboring free volume (ranges between 0.5 and 1), v is volume, and v_f is free volume. Various studies have shown that the fractional free volume ($\frac{v_f}{v}$) increases linearly as temperature increases [62,63,67]. Consequently, according to Eq. (3.4), the volume fraction of defects, and hence volume fraction of preferential nucleation sites, should increase as temperature increases. The implication is that Pd-PFA processed at 220 °C should have higher fractional defect volume than materials processed at 180 °C. This increase in fractional defect volume can result in additional nucleation sites, relatively bigger defect size, or a combination of both. However, it is unlikely that higher processing temperature will result in additional nucleation sites since the saturation number concentration of the nanoparticles in Pd-PFA processed at 220 °C is similar to (and slightly lower than) that in materials processed at 180 °C (Fig. 3). The increase in fractional defect volume may largely come from the growth of defect size. Regardless, the increase in defect volume will allow additional precursor molecules to diffuse into the polymer matrix so that the nanoparticle size should increase accordingly. To verify this, the fractional defect volume n was calculated

using Eq. (3.4) letting $\frac{v}{v_f} = 6.1$ (for $T = 220$ °C) and 7.6 (for $T = 180$ °C)—these values were obtained from a diffusion study for a $Pd(acac)_2$-PFA system [103]. Assuming Δf remains unchanged and the geometrical factor $\gamma = 0.5$ (or 1), Pd-PFA processed at 220 °C has an n value approximately equals to 2.1 (or 4.5) times higher than for material processed at 180 °C. Compared to the total particle volume, which can be determined by assuming all the nanoparticles are spherically shaped, Pd-PFA processed at 220 °C has a total particle volume value 2.6 times higher than material processed at 180 °C. This difference in total particle volume is comparable to the difference in fractional defect volume, which was calculated to range from 2.1 to 4.5. In fact, the fractional defect volume difference equals the total particle volume difference when the geometrical factor $\gamma = 0.63$ is used.

On the basis of the observed relation between particle size and polymer defect volume, we conclude that the volume fraction of defects is directly related to the maximum particle volume fraction. By equating Eq. (3.4) to the volume fraction of spherical nanoparticles, a relation between the average particle radius and the mean fractional free volume f_m can be expressed as:

$$R_{ave} = \left[\frac{3\Delta f}{4\pi\rho_n} exp\left(-\frac{\gamma}{f_m}\right)\right]^{1/3} \tag{3.5}$$

where ρ_n is the particle number density. This result indicates that the average particle radius can be calculated from the mean fractional free volume, or vice versa. For

instance, if $\gamma = 0.63$, $\Delta f = 1$, and $\rho_n = 4.3 \times 10^{-5}$ nm^{-3} (an estimated particle number density based on TEM micrographs), nanoparticles can be grown to an average size ranging from 2.6 to 8.7 nm in diameter when the mean fractional free volume varies from 0.08 to 0.15, which are typical f_m values for fluoropolymers based on the measurements using positron annihilation lifetime spectroscopy [62, 63, 67].

3.3.2 Particle Growth

Decomposition of an organometallic precursor molecule could yield either a metal complex or a metal atom. As a result, there are two separate pathways for formation of stable nanoclusters from precursor molecules: one is for them to bond as complex metal ions then a reduction to occur, or they are reduced first and then bond as atoms. The latter is more likely since the thermogravimetric studies have indicated that the thermal decomposition of $Pd(acac)_2$ is a single-step process that yields Pd atoms and 2acac molecules [40]. After forming stable nanoclusters, the growth rate is directly related to the total flux of atoms joining a cluster [104]. However, the total flux cannot be easily determined since the concentration of atoms at a distance from the center of the particle is not known. This problem can be solved, at steady state, using the lattice approximation, where a constant density of particles is assumed to be regularly distributed on a square lattice [105, 106]. Based on these assumptions, Henry and Meunier numerically solved the rate equation showing that the growth of metal clusters on insulators can be expressed by a power law [104, 107]. However,

steady state growth conditions do not hold in our material system since the average concentration of species available for particle growth diminishes over time. In our case, the nanoparticle growth is analogous to diffusion-limited growth. Previous studies have shown that, during diffusion-limited growth, the average solute concentration $\langle C \rangle$ in a diffusion field can be expressed approximately as follows [108, 109]:

$$\langle C \rangle = (C_0 - C_f)\, exp\left(-\frac{A_D t}{\pi r_f^2}\right) + C_f, \tag{3.6}$$

indicating that the temporal variation of the mean solute concentration depends on the initial C_0 and final C_f concentrations as well as the spacing between nucleation sites r_f and the parameter A_D that is linearly proportional to the diffusion coefficient of the growth species. For our palladium nanocomposites, there are two possible mechanisms for precursor-decomposition-and-particle-growth. Growth of Pd nanoparticles at the early stage can occur by thermal decomposition of Pd precursor followed by capture of diffusing Pd atoms or by direct impingement of Pd precursor molecules on the existing nanoclusters followed by autocatalytic surface growth [89]. The temporal variations of particle size should differ between these two mechanisms (decomposition-and-transport versus transport-and-decomposition) since the diffusion coefficients of palladium atoms and palladium precursor molecules as well as the decomposition rates will likely differ. Despite the differences, the growth of nanoparticles can be estimated by modifying Eq. (3.6). Since the amount of solute that contributes to the particle growth is $1 - \langle C \rangle / C_0$, convolving it with the precursor decomposition

probability function yields an equation that can adequately describe the nanoparticle growth. This equation is given as follows:

$$\left\langle \bar{R} \right\rangle = \left\{ \left[1 - \frac{C_0 - C_f}{C_0} exp\left(-\frac{A_D t}{\pi r_f^2} \right) - \frac{C_f}{C_0} \right] * S(t) \right\}^{1/3}, \tag{3.7}$$

where $\left\langle \bar{R} \right\rangle$ is the average particle radius normalized by the maximum average particle radius, $S(t)$ is the precursor decomposition probability function, and the asterisk indicates convolution with respect to time. For the transport-and-decomposition case, the particle-mediated catalytic decomposition is likely a rapid process so that $S(t)$ can be represented by a Dirac delta function. For the decomposition-and-transport case, the probability of thermal decomposition of precursor is not known. However, a previous study has shown that 50 mg of $Pd(acac)_2$ required approximately 4 hours to be fully decomposed in a nitrogen atmosphere at 190 °C [39]. As a result, the probability function for thermal decomposition of precursor is likely a broad Gaussian distribution under the assumption of normality. For our material system, since the nucleation and growth rates appear to be highest when the processing time is ∼0.5 hour and greatly diminish after ∼1 hour, the mean and the standard deviation of the Gaussian probability density function can both be assumed to be 0.5.

Figure 3.4 shows the time evolution of particle size distributions of Pd-PFA processed at 180 °C. The average particle radii were determined by fitting the particle size distributions with Eq. (3.3). Figure 3.5 shows the change of particle radius as a function of processing times, where the error bars represent ± 1 standard deviation

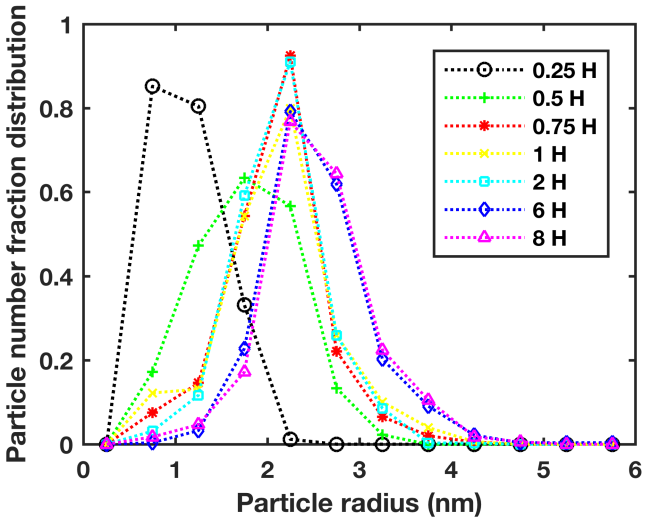

Figure 3.4: Particle size, population distribution of Pd-PFA synthesized at 180 °C with various dwell time.

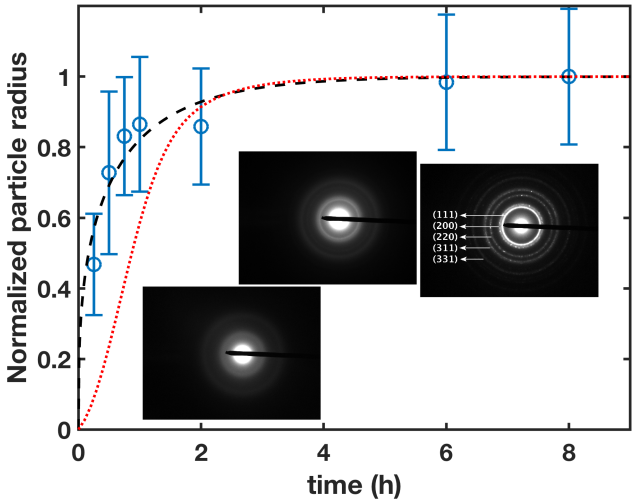

Figure 3.5: Evolution of normalized palladium particle radius at decomposition temperature of 180 °C. The error bars represent ± 1 standard deviation. Dashed line is the curve fit based on Eq. (3.7) with $S(t)$ equals a Dirac delta function; the sum of squared errors of the curve fit is 0.0211. Dotted line is the curve fit based on Eq. (3.7) with $S(t)$ equals a Gaussian probability density function. Inset figures depict representative SAED patterns of Pd-PFA with short (left), medium (middle). and long (right) processing times.

of the radii. In order to use Eq. (3.7) to describe the growth of the nanoparticles, a couple of parameters (C_f and r_f) have to be adequately determined beforehand. First, the final concentration of the growth species, C_f, can be assumed to be 0 since no further particle growth was observed when the dwell time exceeded 8 hours. Second, the radius of the diffusion field, r_f, was taken to be 9 nm, and this value was determined by treating each nanoparticle as a diffusion sink and by employing Voronoi approximation. Specifically, Voronoi tessellation was first performed on the TEM micrographs, and then the area of each Voronoi polygon was approximated by a circular region with an area equal to the polygon. Figure 3.6 shows a TEM image and its corresponding Voronoi diagram where five circles are displayed to demonstrate the area approximation. Finally, the average value of the radii of the circular regions was taken to be r_f. It should be noted that this Voronoi approximation is a two dimensional approach to estimate the radius of the diffusion field. If the average inter-particle distance is 18 nm ($2r_f$) in a 100 nm thick sample, the TEM images would show approximately 6 particle layers on top of each other. As a result, this rough estimation of r_f represents the smallest average first neighbor shell distance of nanoparticles. Under these appropriate assumption and approximation, the growth of the nanoparticles can now be fit using Eq. (3.7). Since the main growth mechanism (decomposition-and-transport versus transport-and-decomposition) is undetermined, the precursor decomposition probability function, $S(t)$, can be taken either as a Dirac delta function or a Gaussian probability density function. Using a least-squares fit-

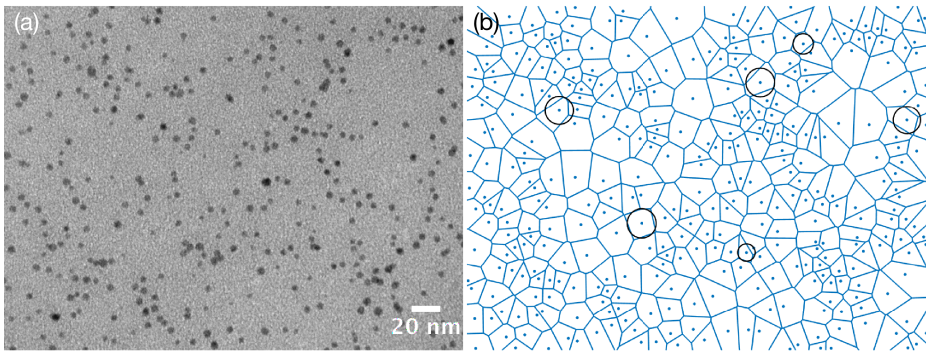

Figure 3.6: (a) Representative TEM image of Pd-PFA synthesized at 180 °C for 8 hours and (b) its corresponding Voronoi diagram. The spaces closest to the diffusion sinks, represented by the Voronoi polygons, are approximated by circular regions with areas equal to those of the polygons. For clarity, selective circular regions are displayed in the diagram.

ting method, Eq. (3.7) appears to fit the growth of particle radius well when the precursor decomposition probability function was the Dirac delta function (Fig. 3.5 dashed line). In contrast, a poor fit was found when the precursor decomposition probability function was taken to be the Gaussian function (Fig. 3.5 dotted line). These results suggest that the transport-and-decomposition process likely dominates over the decomposition-and-transport process. In the case when $S(t)$ was taken as the Dirac delta function, the parameter A_D was found to be 205.5 nm^2/hour, and this parameter is linearly proportional to the diffusion coefficient D such that $A_D = \alpha D$ where α is a coefficient of proportionality [108]. Unfortunately, the values of α and D cannot be determined independently from a single fit. However, it is possible to estimate the diffusion coefficients (and the activation energy) by studying additional sets of particle growth behavior at different processing temperatures and by assuming α is independent of temperature.

It is interesting to note that the nanoparticle growth presented in this study (Fig. 3.5) is similar to the nanocrystal growth proposed by Wang *et al.* [110], which includes classical nucleation and growth followed by aggregative nucleation and growth. The authors illustrated that the classical regime usually produces primary nanocrystals (often ranged in 1 to 3 nm in diameter), and that regime is followed by a second induction and growth period associated with primary nanocrystals diffusion and coalescence (aggregative nucleation and growth). In the final regime, Oswald ripening may or may not be present. The authors also suggested that the aggregative-growth kinetics can be fit using a modified Kolmogorov-Johnson-Mehl-Avrami (KJMA) method. However, since the fitting parameters (a "rate" parameter and the Avrami exponent) possess no physical meaning for nanoparticle formation [111], the fitting results will only be useful in comparison studies [112]. For this reason, even though the KJMA expression can fit the nanoparticle growth profile in Fig. 3.5 reasonably well (but not as well as Eq. (3.7)), the fitting results are not provided here [113].

While interpretation of the particle growth is challenging, we will attempt to describe its growth process by dividing Fig. 3.5 into four different stages. In stage I ($0 < t < 1$ H), the particles have a fast growth rate since the concentration of species available for inclusion in particles is high at the beginning. Both decomposition-and-transport and transport-and-decomposition processes are expected to take place in this stage, but the transport-and-decomposition mechanism likely dominates. In stage II ($1 < t < 2$ H), the average particle size is approximately unchanged, and one

possible explanation is that the Pd nanoparticles begin to crystallize at this stage. During crystallization, atoms in nanoparticles arrange themselves in a close-packed fashion causing a decrease in the sizes of the nanoparticles. However, this decrease in particle size might be accommodated by the growth species that have yet to be bonded to the nanoparticles. As a result, the variation of particle size is small in this stage. Although the crystallization temperature of palladium is up to ∼500 °C [114], crystallization of nanoparticles is known to be size dependent—the smaller the particle the lower the crystallization temperature [115–117]. Electron diffraction measurements were performed on the Pd-PFA samples with short (0.75 H), medium (2 H), and long (6 H) processing times, and representative SAED patterns are shown in Fig. 3.5. As expected, when the processing time is short, the SAED patterns exhibit diffuse rings (left), indicating that the Pd nanoparticles are amorphous. As the processing time increases, the diffraction rings are more distinct (middle). At long processing times, the SAED patterns (right) show relatively sharp rings indicating that the Pd nanoparticles are crystalline [118]. These Pd nanoparticles are polycrystalline, and the SAED patterns exhibit five sharp rings assigned to (111), (200), (220), (311), and (331) lattice planes with spacing 2.2 Å (111), 1.9 Å (200), 1.3 Å (220), 1.2 Å (311), and 0.9 Å (331) of face centered cubic Pd. In stage III ($2 < t < 6$ H), crystallization continues accompanied by a small growth rate. This slow growth could be related to exhaustion of the remaining growth species as well as particle coalescence and oriented attachment (aggregative growth). Occasionally, if the nanoparticles are in close

proximity to each other, they can merge and combine into one large particle in order to reduce their surface area. However, this phenomenon is greatly hindered because of the network structure of the polymer chains. Figure 3.7 shows a particular case of two Pd nanoparticles that have undergone oriented attachment—the lattice fringes at the particle boundary were perfectly aligned. The shape of the PSD is also an indication of aggregative growth of nanoparticles. Grillo *et al.* described the growth of platinum nanoparticles in atomic layer deposition and devised a dynamic model that accounts for single atoms and nanoparticles diffusion and coalescence [119]. In that coalescence model, the characteristic PSD exhibits a right-skewed distribution. This characteristic shape of the PSD is also found in our nanoparticle system, especially at the later stage of particle growth (Fig. 3.4). Neither Oswald ripening nor other types of particle growth was observed in stage IV ($7 > t > 8$ H). The optical properties of the Pd-PFA films remained unchanged even after prolonged processing (up to 18 H). The driving force for Ostwald ripening is the difference in chemical potential between particles of difference sizes. However, Ostwald ripening is likely suppressed since the disperse phase (nanoparticles) has a very low solubility in the continuous phase (polymer matrix). Also, further aggregative growth is unlikely to occur since the nanoparticles can be stabilized by the polymer matrix via steric interaction. While metal nanoparticles have strong van der Waals forces and tend to aggregate when in inert nonpolar media, aggregation is usually prevented by coating the nanoparticles with a tightly bound polymer [120]. The Pd nanoparticles synthesized in this study

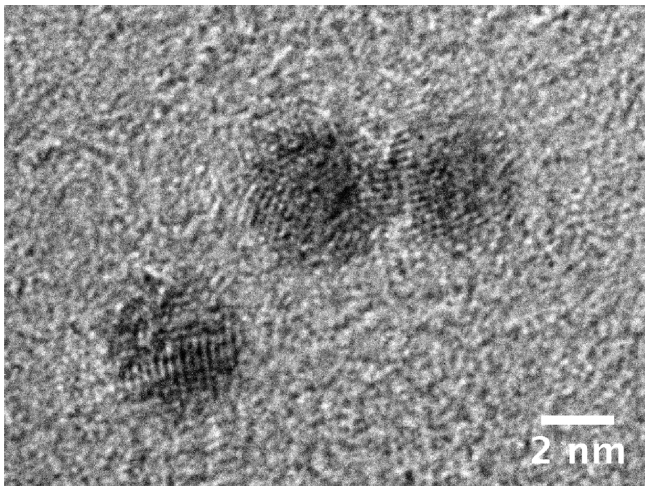

Figure 3.7: High resolution TEM image showing the oriented attachment of two palladium nanoparticles. Materials were synthesized at 180°C for 8 hours.

were not coated with any surfactants. However, these nanoparticles were grown on or in the vicinity of the fluoroalkyl chains of the PFA matrix, and the fluoroalkyl end-capped oligomers are known to be able to encapsulate and stabilize fine metal particles.

3.3.3 Surface percolation of nanoparticles

At a low processing temperature, the four stages of nanoparticle growth are quite evident. However, the time needed to accomplish each stage at higher processing temperatures might be less than at 180 °C. It appears that these nanocomposites can be synthesized in shorter periods of time at higher temperatures. In order to determine the highest temperature that will retain homogeneous particle size and spatial distributions throughout the bulk of the polymer matrix, Pd-PFAs were synthesized at elevated temperatures. However, when the processing temperature was

increased to 240 °C, surface percolation of nanoparticles was observed, and this result is shown by the TEM image in Fig. 3.8 (a). In contrast, Pd-PFA synthesized at 220 °C displays similar particle number densities at the surface as are found in the bulk (see Fig. 3.8 (b)). Although high particle densities in the near surface region have been observed previously with multiple infusions [121], in this work a single infusion at high temperature showed a clear distinction between surface and bulk nanoparticles densities. This is important since we demonstrated that surface-loaded nanocomposites can be synthesized without extended processing. The radius of the nanoparticles in the bulk ranged from 1 to 2 nm, and the bulk exhibits a relatively low particle number concentration compared to the surface. The average radius of the near-surface nanoparticles is approximately 4 nm, more than twice that of bulk nanoparticles. These near-surface nanoparticles are often interconnected so that a randomly percolated structure is formed. While the polymer surface has slightly higher free volume than the bulk [122], it is unlikely that the small difference in free volume is a critical contributing factor for the surface percolation of nanoparticles since PMNCs processed at low temperatures exhibit rather uniform particle number densities in the entire sample. Alternatively, high processing temperatures (≥ 240 °C) cause high precursor decomposition rates, and the resulting palladium atoms build up near the surface since there is not enough time for the precursor concentration to reach equilibrium inside and outside of the polymer matrix—the surface of the polymer possesses higher precursor concentration than the bulk. Therefore, a dense

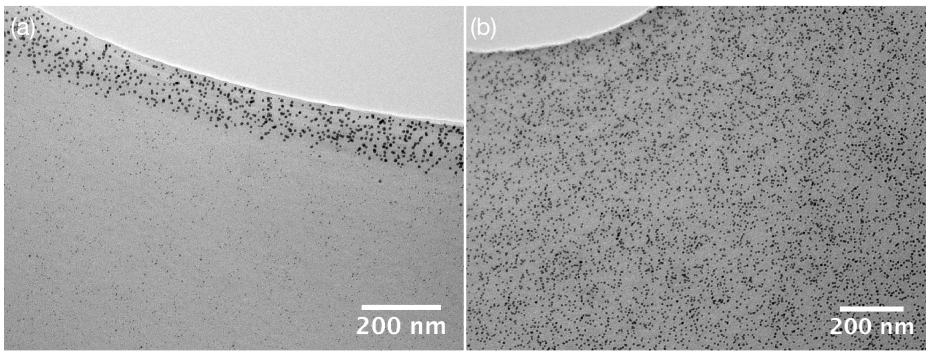

Figure 3.8: TEM images of near surface region of Pd-PFA processed at (a) 240 °C for 2 hours and (b) 220°C for 2 hours.

layer of particles is formed near surface when the processing temperature is relatively high. In addition, the subsurface layer of the Pd particles are formed at the early stage of the decomposition process, and this dense layer of particles obstructs further diffusion of precursor molecules (that have not yet decomposed) into the polymer matrix and consequently relatively small particles are formed in the bulk.

3.4 Conclusion

The formation of palladium nanoparticles in PFA using thermal decomposition of organometallic precursor molecules dispersed inside of a PFA matrix was studied. Detailed TEM studies indicated that the nucleation and growth of palladium nanoparticles in the PFA matrix depended strongly on the processing temperature and the structural characteristics of the polymer matrix. Heterogeneous nucleation of palladium nanoparticles on polymer defects was considered, and it was correlated to the free volume of the polymer matrix. Predictions were in quantitative agreement

with experiment suggesting that nucleation occurs preferentially in the defect/free volume of the polymer matrix. A simple relation between the mean free volume fraction of the polymer and the average particle size was derived. The temporal evolution of the particle radius was interpreted using a modified diffusion-limited growth model. In addition, a four-stage particle growth process was illustrated, which can be summarized as (1) fast growth, (2) crystallization, (3) aggregative growth, and (4) stabilization by steric hindrance. The growth duration of each stage can be shortened by processing at elevated temperatures, and the average particle size increases with temperature. However, when the synthesis temperature is sufficiently high, near-surface percolation of nanoparticles occurs because of high precursor decomposition and diffusion rates. The results obtained here demonstrate that the fundamental limitations of growing nanoparticles in a solid polymer matrix are the processing temperature and the morphology of the polymer matrix. By carefully adjusting the processing temperature, not only monodisperse nanoparticles can be obtained but surface-loaded nanocomposites can also be synthesized. More importantly, it is possible to manipulate the nanoparticle size and spatial distributions by varying the free volume of the polymer matrix.

Chapter 4

CW Laser-induced Precursor Decomposition for Palladium Nanoparticle Modification in Polymer Matrix Nanocomposites

4.1 Introduction

The chemical infusion method involving precursor diffusion, precursor decomposition, as well as particle formation were investigated in detail in the previous two chapters. While this processing method has the potential to produce functional polymer matrix nanocomposites in a scalable way, it cannot actively control the size, number density, composition, and location of the nanoparticles. Forming nanoparticles at selective locations in a polymer matrix can be achieved using optical methods. In many cases, optical excitation is performed using either a continuous wave (CW) or a pulsed laser light source. This chapter focuses on CW laser processing of polymer matrix nanocomposites.

The CW laser irradiation has advantages over pulsed laser irradiation since it precludes the involvement of multi-photon absorption, and a purely photothermal process can be usually singled out. A few studies have reported on production and modification of metal nanoparticles using CW laser irradiation. In particular, Bagratashvili *et al.* synthesized silver-polymer matrix nanocomposites by decomposition of silver precursors in fluoropolymer films using a 532 nm CW laser. However, various photosensitizers were used to increase the optical interactions [123]. In the case of nanoparticle modification, Setoura *et al.* demonstrated CW-laser-induced morphological changes of a single gold nanoparticle, and they contributed the morphological changes to photothermal surface evaporation [124]. Hubenthal *et al.* applied a similar approach to alter the axial ratio of gold and silver nanoparticles using intense CW laser irradiation [125]. In both of these studies, modification of nanoparticles was achieved by illuminating the nanoparticles with light that corresponds to its localized surface plasma resonance (LSPR) which results in an increase in particle temperature and the subsequent surface evaporation. This type of modification is limited to particle size reduction, and results were only demonstrated on a glass or quartz substrate. To the best of our knowledge, *in situ* processing of nanoparticles in a polymer matrix by use of a CW laser has not been reported before.

In this chapter, *in situ* modification of palladium nanoparticles in fluoropolymers using the chemical infusion method along with CW laser irradiation is presented. Specifically, palladium nanoparticles were synthesized using the chemical infusion

method, and these nanoparticles served as seed nanoparticles. To modify the size and number density of the palladium nanoparticles at selective locations, an additional infusion of palladium precursor was performed, followed by CW laser irradiation. During the laser exposure, various background temperatures were applied in order to explore the particle modification processes. The changes of particle size and number density were examined using transmission electron microscopy, and results were interpreted by considering the roles of precursor photolysis, photothermal particle heating, and photocatalytic interactions. In particular, temperature rises resulting from optical absorption of the palladium nanoparticles were calculated and were used as criteria for identifying the main photo-induced mechanism.

4.2 Optical heating of nanoparticles

4.2.1 Background

A system with spherical symmetry consisting of a palladium nanoparticle of radius R enclosed in a PFA matrix is considered. The nanoparticle is photothermally excited, and the optical energy deposition is assumed to be uniform throughout the nanoparticle since the optical penetration depth in palladium is relatively large compared to the nanoparticle size. For the particle-matrix system under consideration, the classical thermal diffusion models can be used to describe the heating of the particle and the thermal diffusion into the polymer matrix. In particular, two differential

equations can be used to describe the thermal diffusion in the polymer matrix as well as in the particle, and two boundary conditions at the particle/polymer interface can be applied to specify the continuity of temperature and conductive heat flux. These equations are given by [126]:

$$\begin{aligned}
\rho_m c_{vm} \frac{\partial T_m}{\partial t} &= \frac{1}{r^2}\frac{\partial}{\partial r}\left(r^2 \cdot \kappa_m \frac{\partial T_m}{\partial r}\right), \quad r > R \\
\rho_p c_{vp} \frac{\partial T_p}{\partial t} &= \frac{1}{r^2}\frac{\partial}{\partial r}\left(r^2 \cdot \kappa_p \frac{\partial T_p}{\partial r}\right) + S, \quad r < R \\
T_m|_{r=R} &= T_p|_{r=R} \\
\kappa_m \frac{\partial T_m}{\partial r}\bigg|_{r=R} &= \kappa_p \frac{\partial T_p}{\partial r}\bigg|_{r=R}
\end{aligned} \tag{4.1}$$

where ρ, c_v, and k are the material density, specific heat capacity, and thermal conductivity, respectively. The subscript m and p refer to matrix and particle, respectively. All the material parameters are assumed to remain constant since extreme thermodynamic conditions are not considered. Temperature, time, radial distance from particle center, and heat source power density are represented by T, t, r, and S, respectively. In addition, the whole material system has a uniform initial temperature distribution such that $T_p = T_m$ when $t = 0$.

4.2.2 CW laser illumination

4.2.2.1 Single nanoparticle heating

A CW laser light source at an angular frequency $\omega = 2\pi c/\lambda_0 = kc$ is used, where c is the speed of light, λ is laser wavelength, and k is angular wavenumber. When the

laser light penetrates the polymer matrix, the speed of light in the material changes because the refractive index of the polymer matrix (n_m) is different than that of air. The wavenumber (or wavelength) experienced by the nanoparticle should be modified such that $k_p = 2\pi/\lambda_p = n_m/k$. At the very beginning of CW laser particle heating, the transient temperature profile of the nanoparticle is very different than that of the surrounding polymer matrix since the thermal diffusivity of the nanoparticle is much higher than that of the polymer matrix—the thermalization inside the nanoparticle occurs much faster. Consequently, the establishment of the steady-state temperature profile of the particle-matrix system can be considered to be governed by the time scale associated to the evolution of the temperature profile in the polymer matrix. The characteristic time of the transient heating process can be approximated by $\tau_{nano} = R^2/D_m$, where D_m is the thermal diffusivity of the surrounding matrix. After the transient period, a steady state temperature profile is reached for CW laser particle heating since the absorbed heat will be balanced by heat dissipation to the polymer matrix. In the steady state regime, the two differential equations in Eq. (4.1) can be written as follows:

$$\begin{aligned} \frac{\kappa_m}{r^2}\frac{\partial}{\partial r}\left(r^2\frac{\partial T_m}{\partial r}\right) &= 0, \quad r > R \\ \frac{\kappa_p}{r^2}\frac{\partial}{\partial r}\left(r^2\frac{\partial T_p}{\partial r}\right) &= -S, \quad r < R \end{aligned} \tag{4.2}$$

The solution for Eq. (4.2) has a simple form and is given in the following [126]:

$$\begin{aligned} T_m &= \frac{\sigma_{abs} I}{4\pi\kappa_m r}, \quad r > R \\ T_p &= \frac{\sigma_{abs} I}{4\pi\kappa_m R}\left[1 + \frac{\kappa_m}{2\kappa_p}\left(1 - \frac{r^2}{R^2}\right)\right], \quad r < R \end{aligned} \tag{4.3}$$

where σ_{abs} is the absorption cross section and I is laser intensity. It should be noted that the interface resistivity at the particle/polymer interface is assumed to be 0 in Eq. (4.3). The presence of interface resistivity requires modification of boundary condition (continuity of temperature), and the direct consequence of this modification is temperature drop/discontinuity at the interface boundary [126]. This scenario is not considered since the temperature of the polymer in direct contact with the surface of the nanoparticle should be the same temperature as the nanoparticle in steady state. Furthermore, since the thermal conductivity of the metallic particle is much higher than the polymer matrix (i.e. $\kappa_m/\kappa_p \approx 0$), the temperature is essentially uniform throughout the particle volume so that T_p can be simplified to:

$$T_p = \frac{\sigma_{abs} I}{4\pi\kappa_m R}. \tag{4.4}$$

4.2.2.2 Multiple particles heating

Under CW laser irradiation, a large number of dispersed nanoparticles can produce a significant global temperature rise owing to the overlap of numerous temperature fields. For an ensemble of nanoparticles, two additional time scales must be

considered: (1) the time needed for the temperature fields from neighboring particles to overlap, which can be approximated as $\tau_0 = \Delta^2/D_m$ where Δ is the average particle-particle separation; (2) the time scale for heat diffusion across the entire material volume that contains the heated nanoparticles, which can be expressed by $\tau_{global} = L_H^2/D_m$ where L_H is the spatial extent of the heated region.

The global temperature rise can be estimated by considering the nanoparticles as homogeneous heat sources distributed throughout the heated region. Under this condition, superposition of the thermal fields from the heated nanoparticles leads to a global temperature rise, and it is given by [127]:

$$T = \frac{N_p L_H^2 \sigma_{abs} I}{2\kappa_m} \tag{4.5}$$

where N_p is the particle number concentration.

4.3 Experimental Methods

4.3.1 Materials, thermal processing, and characterization

Palladium nanocomposites were produced using palladium(II) acetylacetonate ($Pd(acac)_2$; 99% Pd; Sigma-Aldrich) as a precursor for synthesis of palladium nanoparticles in a [tetrafluoroethylene-co-(perfluoropropyl vinyl ether)] (PFA; CS Hyde) matrix. Palladium nanocomposites, Pd-PFA, were synthesized using the chemical infusion technique [21]. The synthesis process was started by placing a $50 \times 50 \times 0.127$

mm^3 PFA film in a glass reaction vessel (1 L) along with ∼10 mg of $Pd(acac)_2$ powder dispersed around the inner wall of the vessel. The reaction vessel was evacuated to ∼160 mTorr in order to remove air from the vessel as well as volatiles from the PFA matrix. The sublimation/vaporization temperature and decomposition temperature were approximately 413 K and 473 K, respectively. The reaction vessel was transferred to an oven and heated to 413 K for 2 hours to sublime/vaporize the precursor and allow the precursor to diffuse into the polymer. The temperature of the oven was then raised to 473 K and held for 2 hours to induce precursor decomposition followed by nanoparticle formation.

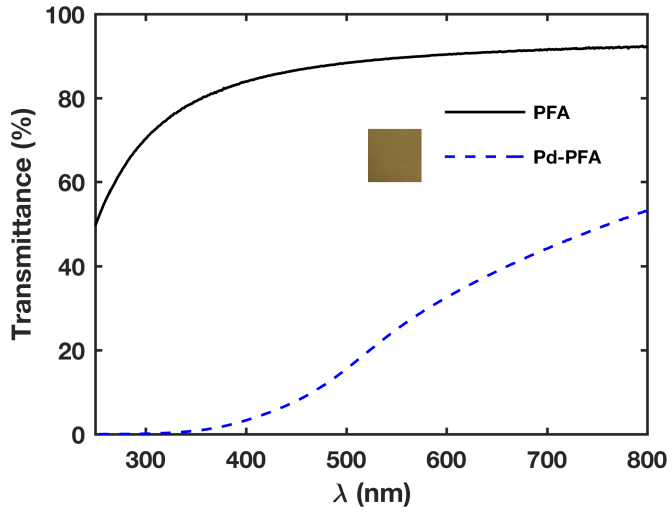

Figure 4.1: Optical transmission spectra for Pd-PFA and the as-received PFA matrix. The inset shows an optical image of Pd-PFA.

Optical transmission spectra shown in Fig. 4.1 for PFA and Pd-PFA were taken using a PerkinElmer Lamda 950UV/Vis spectrophotometer for wavelengths between 250 to 800 nm. While the as-received PFA transmits well throughout the visible re-

gion, the presence of palladium particles produces strong absorption in the ultraviolet (UV) region and a broad absorption in the visible region. The Pd-PFA exhibits a homogeneous light brown color (inset image) suggesting that the particles are uniformly distributed. To verify the distribution and the presence of palladium nanoparticles, cross sections for transmission electron microscopy (TEM) imaging and energy dispersive X-ray spectroscopy (EDS) analysis were prepared using room-temperature diamond microtome methods. These sections were mounted on copper grids and imaged on a 100 kV FEI Tecnai 12 transmission electron microscope, and an Oxford EDS detector was used for the elemental analysis. Figure 4.2 (a) shows a representative TEM image of Pd-PFA. Discrete nanoparticles having average radius 1.6 nm are distributed throughout the bulk of the PFA film. Figure 4.2 (b) shows an EDS spectrum, and a relatively small amount of palladium is present, which is consistent with the estimated value of volume percentage of palladium ($< 0.05\%$). The carbon, oxygen, and fluorine peaks come from the PFA matrix.

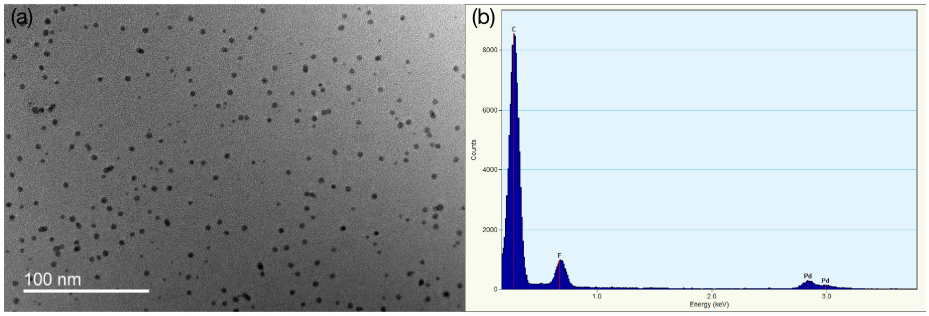

Figure 4.2: (a)Representative transmission electron micrographs of Pd-PFA. (b) Energy dispersive X-ray spectroscopy analysis for Pd-PFA.

A second infusion process was performed by heating a vacuum reaction vessel

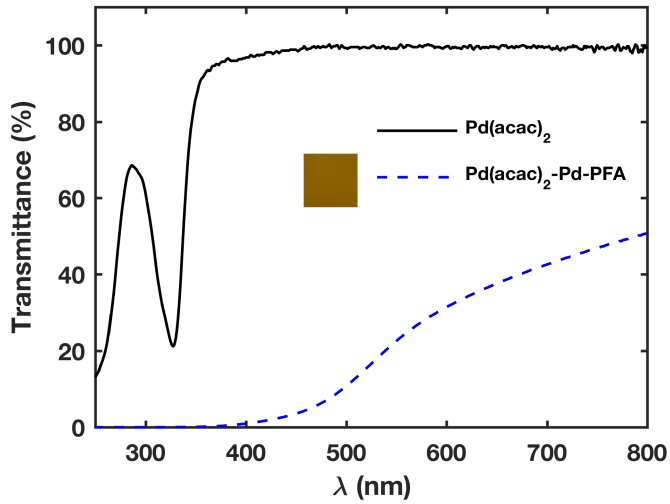

Figure 4.3: Optical transmission spectra for $Pa(acac)_2$-Pd-PFA and $Pa(acac)_2$. The inset shows an optical image of $Pa(acac)_2$-Pd-PFA.

that contained Pd-PFA as well as ∼10 mg of $Pd(acac)_2$ at the precursor vaporization temperature for two hours. The resulting material is designated as $Pd(acac)_2$-Pd-PFA. Figure 4.3 shows the optical transmission spectra for $Pd(acac)_2$-Pd-PFA and $Pd(acac)_2$. Based on the homogeneous color of the film shown in the inset of Fig. 4.3, $Pd(acac)_2$ is believed to be distributed uniformly in the film. The absorption spectra of $Pd(acac)_2$-Pd-PFA and Pd-PFA are similar. However, the color of the $Pd(acac)_2$-Pd-PFA film did appear to be slightly darker than Pd-PFA. This slight darkening is most likely caused by the palladium chemical precursor since it absorbs well near the ultraviolet region and no darkening was found for Pd-PFA in the same processing environment (without the presence of the chemical precursor). The $Pd(acac)_2$-Pd-PFA film was used as the starting material for CW laser processing.

4.3.2 CW laser processing and characterization

Choosing an appropriate laser light source is an important step for optical processing. In general, the characteristics of the excitation laser (i.e. wavelength) should be chosen to provide direct interaction with the particles or the precursor. The palladium precursor has a strong absorption below 350 nm (Fig. 4.3), and the LSPR of palladium nanoparticles is also located in the deep ultraviolet region [128]. However, ultraviolet laser light source was not chosen since UV lasers could result in photodegradation of fluoropolymers [129, 130]. Fortunately, palladium nanoparticles exhibit moderate absorption in the visible region (Fig. 4.1).

In this study, a 532 nm CW laser (Coherent DPSS) was used, and the average intensity of the laser beam was 1.59×10^4 W/m^2. A few controlled experiments were done on Pd-PFA in order to identify the proper processing conditions. In particular, Pd-PFA was treated with the laser in air and in vacuum (∼160 mTorr). After about 2 seconds of illumination at room temperature, a shallow deformation on the surface

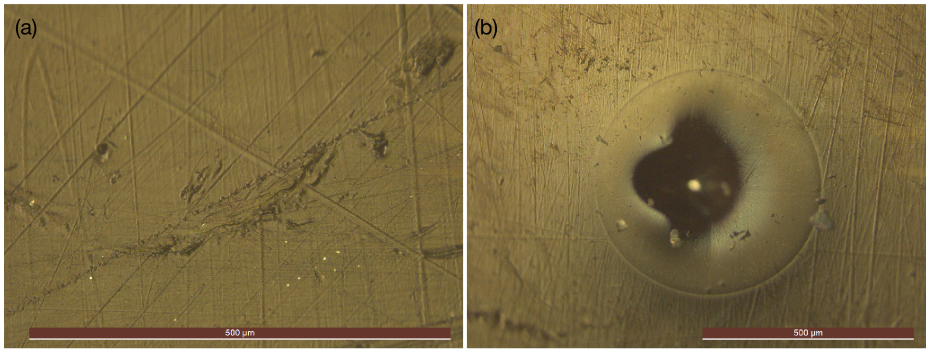

Figure 4.4: Optical micrographs of Pd-PFA after 2 seconds of 500 mW 532 nm CW laser irradiation: (a) in air and (b) in vacuum.

(dent) was found on the illuminated region when Pd-PFA was placed in air, and an ablated hole was observed when the film was put in an evacuated glass vessel. While the surface of the dent region appears to be protruded along surface scratches (Fig. 4.4 (a)), the ablated region consists of a circular hole approximately 250 μm in diameter. It should be noted that the as-received PFA did not exhibit any physical damage when the same laser irradiation conditions were used. The deformation and degradation of the polymer matrix likely involve polymeric bond scission as well as photooxidation when irradiating in air [131, 132]. In order to avoid photodegradation of the polymer matrix, the laser beam size was expanded so that the average intensity was lowered to 307 W/cm^2. The resulting beam did not induce any physical change to the Pd-PFA.

Laser processing of Pd(acac)$_2$-Pd-PFA was performed in vacuum to avoid photo-oxidation. In a typical experiment, synthesis began by placing the sample in a glass

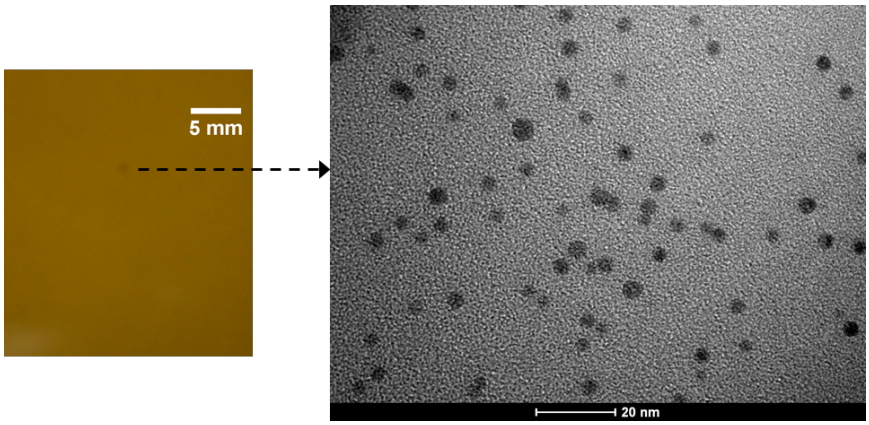

Figure 4.5: An optical image of Pd(acac)$_2$-Pd-PFA showing a small dark spot after 20 minutes of CW laser irradiation at room temperature. A representative TEM image shows the distribution of palladium nanoparticles at the laser-processed region.

reaction vessel. The vessel was evacuated to 160 mTorr. The CW laser beam was then directed to the $Pd(acac)_2$-Pd-PFA material. After more than 20 minutes of exposure at room temperature, a small dark spot appeared. Figure 4.5 shows an optical image of the laser-processed material as well as a TEM image of the laser-processed region. This darkening is related to the change of optical cross section of the nanoparticles; the size and the number density of the nanoparticles increase as a result of precursor decomposition. In order to accelerate the process, the background temperature was increased by placing the reaction vessel in a custom-made oven equipped with an optical window that allowed for laser processing. Increasing the background temperature would accelerate the precursor decomposition and the particle modification processes since polymer chain mobility as well as precursor diffusivity increase with temperature [103]—the time needed for the precursor molecules to diffuse to the precursor depletion zone would be reduced [76]. Figure 4.6 (a) shows an optical image of $Pd(acac)_2$-Pd-PFA after laser exposure at background temperature 353 K. When the exposure time exceeded 2 minutes, a small dark spot started to appear. As the processing time increased, the size of the dark spot increased. Representative TEM micrographs are presented for the corresponding dark regions in Fig. 4.6 (a). Both particle size and particle number density increased with the processing time. When the exposure duration was 2, 5, and 10 minutes, the average particle radius was approximately 1.6, 2.0, and 2.9 nm, respectively. Although a majority of the nanoparticles were isolated, there were a few regions where the particles seemingly

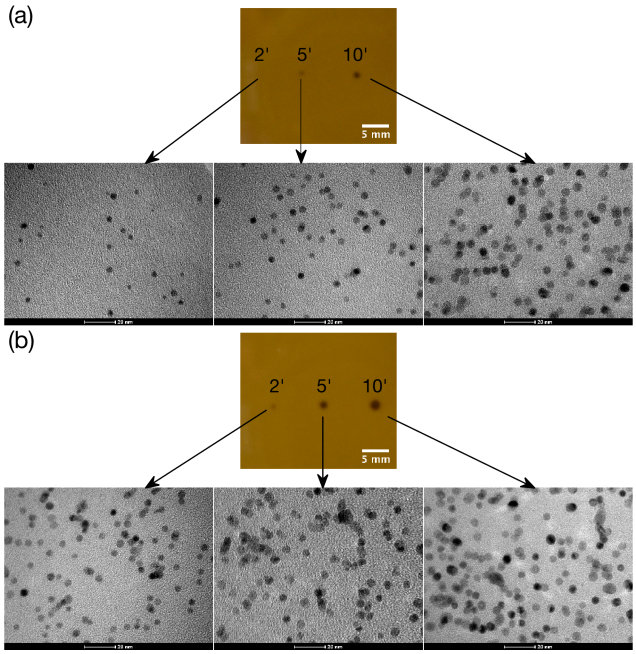

Figure 4.6: Optical images of $Pd(acac)_2$-Pd-PFA showing dark spots after 2, 5, and 10 minutes of CW laser irradiation at background temperature (a) 353 K and (b) 433 K. Representative TEM images show the distribution of palladium nanoparticles at their corresponding locations.

grew into each other. When the background temperature was increased to 433 K, the dark spots on the optical images appeared to be roughly twice as big as those processed at 353 K for each laser duration (Fig. 4.6 (b)). While the TEM images also show that the particle size and number density increased as the irradiation time increased, processing at 433 K exhibited faster particle formation and growth rates than at 353 K. At background temperature 433 K, the average particle radius was approximately 2.1, 2.7, and 2.9 nm when the exposure time was 2, 5, and 10 minutes, respectively. In addition, string-like nanostructures were more noticeable in materials processed at high temperature.

4.4 Results

4.4.1 Mechanisms

The mechanism for precursor decomposition is important since the changes of particle size and particle number density (Fig. 4.2 versus Fig. 4.5 and 4.6) are directly related to it. All the possible photo-induced chemical reactions should be considered, and they include: (1) direct photolysis of the precursor; (2) photothermal heating of the seed nanoparticles driving decomposition of nearby precursor; (3) photocatalytic precursor decomposition; (4) photocatalytic interactions with the polymer matrix producing reactive radicals that induce precursor decomposition. Although direct photolysis of precursor is unlikely based on the absorption characteristics of $Pd(acac)_2$ at the laser wavelength (Fig. 4.3), this photo-induced interaction should be examined since various metal precursors are photosensitive and no studies have been reported on the photolysis of $Pd(acac)_2$. In particular, laser irradiation was performed on PFA matrix containing only $Pd(acac)_2$—this material was made by heating an as-received PFA and 10 mg of $Pd(acac)_2$ in vacuum at 413 K for 2 hours. The transmission characteristics of the irradiated region remained unchanged after extended exposure. This result together with results obtained in Fig. 4.5 and 4.6 indicate that precursor decomposition is not caused by photolysis but some type of particle-mediated reactions. Identifying the main particle-mediated mechanism for precursor decomposition (photothermal versus photocatalytic reactions) could be

challenging. However, in the following, we will present model results for temperature rises via photothermal particle heating in Pd-PFA and compare them to the decomposition temperature of $Pd(acac)_2$. The role of photocatalytic reactions for precursor decomposition will also be considered.

4.4.2 Photothermal particle heating

For the precursor-particle-matrix system considered here, the thermal excitation of the precursor follows the matrix temperature. The particle (and its surrounding matrix) temperature rise resulting from the CW laser heating can be estimated using Eq. (4.4). In order to use this equation, the particle absorption cross section σ_{abs} has to be determined beforehand. For very small spherical nanoparticles ($R < 15$ nm), the optical absorption cross section can be approximated as follows [133, 134]:

$$\begin{aligned} \sigma_{abs} &= k_p \, \mathrm{Im}(\alpha) - \frac{k_p^4}{6\pi} \left|\alpha\right|^2 \\ \alpha &= \frac{4\pi R^3 (\epsilon_p - \epsilon_m)}{(\epsilon_p + 2\epsilon_m)} \end{aligned} \tag{4.6}$$

where ϵ_p and ϵ_m are relative permittivity of the particle and the matrix, respectively. Using the values provided in Table 4.1, the absorption cross section was calculated to be $4.97\times\ 10^{-19}$ m^2. In addition to the theoretical approximation, the absorption cross section can also be determined based on the absorbance spectroscopy results in Fig. 4.1. Assuming the scattering cross section is 0 (an appropriate assumption for very small nanoparticles), the absorption cross section of the nanoparticles can be

Table 4.1: Material Constants of PFA Matrix [3, 4] as well as Palladium [5] and Specification for Laser Intensity and Wavenumber

ϵ_p	ϵ_m	κ_m (W/(m*K))	n_m	D_m (m^2/s)	k_p (1/m)	I (W/m^2)
-6.89 + 7.62 i	1.82	0.195	1.35	7.70×10^{-8}	1.59×10^{7}	1.43×10^{3}

approximated according to the Beer-Lambert law as [135]:

$$\sigma_{abs} = \frac{A \,\mathrm{Ln}10}{NL} \tag{4.7}$$

where A is the absorbance, N is the number concentration of nanoparticles, and L is the pathlength or thickness of the material. Considering $A = 0.66$ (obtained from Fig. 4.1), $L = 0.0127$ cm (thickness of the nanocomposites), and $N = 1.75 \times 10^{16}$ cm^{-3} (an average value based on the TEM analysis), the absorption cross section was calculated to be $6.84\times\ 10^{-19}$ m^2, which is very similar to the theoretical estimate based on Eq. (4.6). The theoretical and experimental values of the absorption cross section were averaged, and this value was used for calculation of temperature increase resulting from the photo-excited particle.

According to Eq. (4.4), a 1.6 nm palladium nanoparticle in a PFA matrix is expected to have an increase in temperature of only 4.9×10^{-8} K, and the time needed to heat the particle surface to the steady state temperature is less than 50 ps (τ_{nano}). Even though the temperature rise for a single nanoparticle is negligible, the temperature rise of a system containing a large number of nanoparticles in close proximity

could be greatly enhanced. For this material system, the palladium nanoparticles are rather uniformly dispersed, so the mean inter-particle distance can be estimated by performing Voronoi tessellation on the TEM micrographs and then equating the area of each Voronoi polygon to a circular region followed by averaging of the radii—the average distance among palladium nanoparticles Δ is $\sim$23 nm. Based on this approximation, it takes less than 10 ns (τ_0) for the temperature fields to reach the surfaces of the neighboring nanoparticles, and the temperature of the heated region will start to increase subsequently.

At later times, the global temperature rise dominates the total temperature change, and the final steady state is reached in a few tens of seconds. According to Eq. (4.5) and taking $L_H = 4$ mm (radius of the heated region), the steady-state, global temperature rise in the nanocomposite in the irradiated region is $\sim$130 K. In the cases when the background temperatures were set to 433 and 353 K, the heated region are expected to have temperatures as high as 563 and 483 K, respectively. While these temperatures are not high enough to deteriorate the PFA matrix, they can readily decompose the palladium precursor since its decomposition temperature is above 453 K [39,40]. When the precursor decomposition is driven by thermal activation, the decomposition rate depends on the probability for thermal decomposition of palladium precursor [136]. Higher temperature generally yields higher precursor decomposition rate. As a result, faster particle formation can be expected at higher processing temperature. This is supported by the optical as well as the TEM images in Fig.

4.6, where new particle formation and particle growth occurred noticeably faster at background temperature 433 K than at 353 K. It should be noted that, based on the global temperature calculation, the ablation of Pd-PFA in Fig. 4.4 (b) is caused by photothermal particle heating. The laser beam used in the controlled experiments was ∼50 times more intense than the one used for $Pd(acac)_2$-Pd-PFA (1.59×10^4 versus 307 W/m^2). According to Eq. (4.5) and having $L_H = 1.1$ mm, this intense laser beam can induce a steady-state temperature rise above 500 K in the irradiated region, which can easily decompose the PFA matrix.

In the case when the background temperature was at room temperature, the irradiated region is expected to have a temperature of 428 K. While this temperature is not high enough to thermally decompose the palladium precursor [39], CW laser-induced darkening of $Pd(acac)_2$-Pd-PFA was observed (Fig. 4.5). As a result, it is unlikely that precursor decomposition is a purely thermal process when the background temperature is relatively low.

4.4.3 Photocatalytic processes

Palladium is a well-known catalyst for a great number of chemical reactions [137–141], and its photocatalytic behaviors have been demonstrated in various studies, which showed significantly higher reaction rates when conducted under illumination than in dark conditions [142, 143]. The proposed mechanism for photocatalytic reactions consists of a series of electron excitation and electron transfer processes.

Specifically, the absorption of visible light and UV light by palladium nanoparticles can excite electron interband transitions, and these light-excited electrons at the surface of the nanoparticles can then transfer to species adsorbed on the nanoparticles. This type of electron transfer can weaken the chemical bonds of the adsorbed species and hence facilitate the activation of chemical reactions. At elevated background temperatures and/or high irradiation intensities (such as the processing conditions used in this study), a large number of electrons can populate the upper energy levels of the palladium nanoparticles. Electron transfer and hence photocatalytic reactions can be readily achieved if the reactant $Pd(acac)_2$ molecules are physically attached to the seed palladium nanoparticles. The growth of the nanoparticles should be limited by the diffusion of chemical precursor onto the surface of the seed nanoparticles. Consequently, the photocatalytic reaction rate should be faster at higher temperature since mass diffusion coefficient has a temperature dependence. In addition, the precursor diffusivity depends on the structure of the polymer matrix [103]. The glass transition temperature (T_g) of the PFA matrix is $\sim$363 K [3]. Above this temperature, the polymer chain mobility is sufficiently high to facilitate the diffusion of precursor; below T_g, diffusion of the precursor molecules is likely hindered by the rigid polymer chains. This is supported by comparing the processing times needed to see changes in materials at different background temperatures.

While the average particle size increases with the processing time (Fig. 4.6), the particle number density increases as well. At high background temperatures (433

K and 353 K), the formation of additional particles could be attributed to thermal decomposition of precursor followed by particle nucleation and growth. At a low background temperature (room temperature), neither photothermal particle heating nor photocatalytic precursor decomposition could explain the increase in particle number density. One possible interpretation is that photocatalytic reactions also occur between the photo-excited palladium nanoparticles and the PFA matrix. It is well-known that deep UV light with high photon flux can induce chain scission reactions and defluorination of the backbone of fluoropolymers [131]. While the laser light source used in this study is not capable of direct photolysis of the polymer, it is possible that photocatalytic interactions occur between the palladium nanoparticles and the surrounding PFA matrix producing active intermediates such as CFx and F radicals [144]. These radicals could react with the precursor molecules resulting in formation of palladium atoms. In addition, the regions where the polymer bonds/chains break could serve as heterogeneous nucleation sites for nanoparticle formation [136]. This hypothesis suggests that nanoparticles would tend to form close among each other as the processing time increases since the length scale of the photocatalytic reaction zone is likely in the range of nanometers or less. An ensemble of particles could merge to form agglomerated nanostructures, such as string-like particles.

4.5 Discussion

Three particle-mediated, precursor decomposition mechanisms have been proposed based on the sizes and geometries of nanoparticles obtained from the TEM micrographs as well as calculations of CW-laser induced temperature rises near particles. All three mechanisms likely facilitate the precursor decomposition processes. However, at high background temperatures, precursor decomposition is dominated by thermal activation. At low background temperatures, photocatalytic reactions would most likely dominate initially, but as the average particle size and particle number density increase, photothermal particle heating would become the primary contributor to precursor decomposition. For example, if the average particle size is 2 nm and the particle number concentration is 2.0×10^{16} cm^{-3}, the steady-state temperature rise in the illuminated region would be $\sim$200 K. It is difficult to measure the exact contribution of the proposed mechanisms to the overall precursor decomposition and particle modification processes. However, we have identified the dominating mechanisms under various processing environments and also described the limiting factors for each of the mechanisms. For photothermal particle heating and photocatalytic precursor decomposition, the growth of palladium nanoparticles is limited by the thermal decomposition probability of palladium precursor and the diffusion of palladium precursor, respectively; for photocatalytic interactions with the polymer matrix, precursor decomposition would depend on the likelihood of producing reactive radicals

and the probability of radicals encountering the precursor molecules.

The increased size of palladium nanoparticles for materials photoprocessed for increasing times suggests that the surface of the palladium particles remain accessible to palladium atoms and palladium precursor. The increased particle number concentration for increased processing time indicates that additional nucleation sites are available in the polymer matrix. Furthermore, the particle size differences between the seed nanoparticles and the newly formed nanoparticles are minimal suggesting that the growth of nanoparticles slows down as they become bigger, and this is likely caused by the steric effect among the fluoroalkyl chains in the PFA matrix—the repulsion among chains prevents particles from growing beyond the nanometric size.

4.6 Conclusion

This work has reported the modification of nanoparticles in polymer matrix nanocomposites containing palladium nanoparticles and palladium precursor using continuous wave laser excitation. Optical excitation of the seed palladium nanoparticles resulted in decomposition of palladium precursor and subsequent growth of seed nanoparticles as well as formation of additional palladium nanoparticles. Transmission electron micrographs show that both nanoparticle size and particle number concentration increase as the processing time increases, and string-like nanostructures can be found within the polymer matrix after extended laser exposure. Temperature rises in the irradiated regions were approximated, and results indicate that the temperature

increase can facilitate the precursor diffusion and precursor decomposition. Photocatalytic processes were also considered, and we believe that photothermal and photocatlytic reactions all contribute to palladium precursor decomposition and subsequent particle formation as well as particle modification. However, we conclude that the thermal decomposition processes dominate at high temperatures, while the catalytic processes dominate initially at low temperatures. The processing approach here demonstrates that it is possible to modify the size, number density, and shape of nanoparticles *in situ* inside the polymer matrix using a continuous wave laser light source. By regulating the irradiation period, intensity, and spot size, interesting nanostructures can be created leading to the possibility of patterning nanocomposites with spatially-varying properties.

Chapter 5

Femtosecond Pulsed Laser-induced Palladium Precursor Decomposition in Tungsten Oxide Polymer Matrix Nanocomposites

5.1 Introduction

In the previous chapter, we demonstrated a CW laser processing method that allowed us to control the particle size and particle number density spatially via photothermal particle heating. In this chapter, the same processing approach is applied, but a femtosecond pulsed laser is used as the photo-activation source for *in situ* particle modification of polymer matrix nanocomposites. Pulsed laser processing has the potential to create highly localized heating since a large amount of energy can be provided to a material system in a short amount of time. If the duration of the optical pulse is shorter than the time needed for heat to diffuse the distance of the average inter-particle spacing, the temperature fields from surrounding particles will

not overlap significantly and the temperature fields will be localized to the close vicinity of the particle. In addition, pulsed laser processing can often trigger nonlinear optical responses that could facilitate the particle modification processes.

Numerous studies have shown that pulsed lasers can be used to synthesize nanoparticles at selective locations in a polymer matrix. Fragouli *et al.* grew cadmium sulfide nanocrystals in a polymer matrix by diffusing cadmium sulfide chemical precursor into a polymer and subsequently decomposing the precursor by laser photolysis using a nanosecond pulsed ultraviolet laser [145]. A similar approach was used by Watanabe *et al.* to synthesize gold and iron-platinum alloy nanoparticles in polyvinylpyrrolidone [146]. Femtosecond pulsed laser irradiation has also been used to selectively grow silver [147] and lead sulfide [148] nanoparticles in polymer matrices by multiphoton processes. Unfortunately, these photo-induced unimolecular decomposition and photoreduction reactions provide little control over particle size, and large nanosized particles as well as aggregation of nanoparticles are often produced. Previous studies have demonstrated a method to modify the composition of nanoparticles locally. In these studies, multi-component nanoparticles were synthesized by combining the chemical infusion method with femtosecond laser irradiation to decompose the chemical precursors near the seed nanoparticles in fluoropolymers [1, 76]. While the combination of chemical infusion and femtosecond laser processing allows for a high degree of control of particle composition and location, modification of nanoparticles could only be achieved at high processing (background) temperatures ($\sim$400 K).

In situ particle composition modification in silicone matrices using the chemical infusion method along with femtosecond pulsed laser irradiation at room temperature is demonstrated here. In particular, the silicone matrix nanocomposites containing tungsten oxide particles along with a palladium precursor were synthesized using the chemical infusion method. These nanocomposites were photo-excited using femtosecond laser pulses to decompose the palladium precursor in the near-particle environment. Temperature increases resulting from the femtosecond-pulsed optical heating of tungsten oxide nanoparticles were modeled and used to determine the likelihood of thermal decomposition of palladium precursor. Photocatalytic processes were also considered since tungsten oxide is a well-known photocatalyst. The nanocomposites were examined using transmission electron microscopy as well as energy-dispersive X-ray spectroscopy to provide additional insights related to this processing method.

5.2 Experimental Methods

5.2.1 Materials, thermal processing, and characterization

The tungsten oxide nanocomposites were produced using tungsten hexacarbonyl ($W(CO)_6$; 97%; Sigma-Aldrich) as a precursor for synthesis of tungsten oxide particles in a high-temperature silicone rubber (McMaster-Carr Supply) matrix. This silicone matrix is optically transparent and has good thermal stability for temperatures up to 490 K. Tungsten hexacarbonyl was used as the precursor because it has a

low decomposition temperature and has been used extensively for study of chemical deposition [149, 150].

Tungsten oxide nanocomposites (designated as WO_3-Silicone) were synthesized using the chemical infusion technique [21]. The synthesis was begun by placing a 100 $\times$ 60 $\times$ 0.5 mm^3 silicone rubber sheet in a glass reaction vessel along with $\sim$200 mg of $W(CO)_6$ powder dispersed around the inner wall of the vessel. The reaction vessel was evacuated to $\sim$160 mTorr in order to remove air from the vessel as well as volatiles from the silicone matrix. The sublimation/vaporization temperature and decomposition temperature of tungsten hexacarbonyl were approximately 403 K and 453 K, respectively. The reaction vessel was heated to 403 K for 2 hours to sublime/vaporize the precursor and allow the precursor to diffuse into the polymer, and the temperature was then raised to 453 K and held for 3 hours to induce precursor decomposition and permit particle formation. These processing steps were repeated three times in order to increase tungsten oxide content. The volume percentage of tungsten oxide was roughly 0.5% after 3 infusion cycles. Cross sections of WO_3-silicone were prepared using room-temperature diamond microtome methods. These sections were mounted on copper grids and imaged on a 100 kV FEI Tecnai 12 transmission electron microscope.

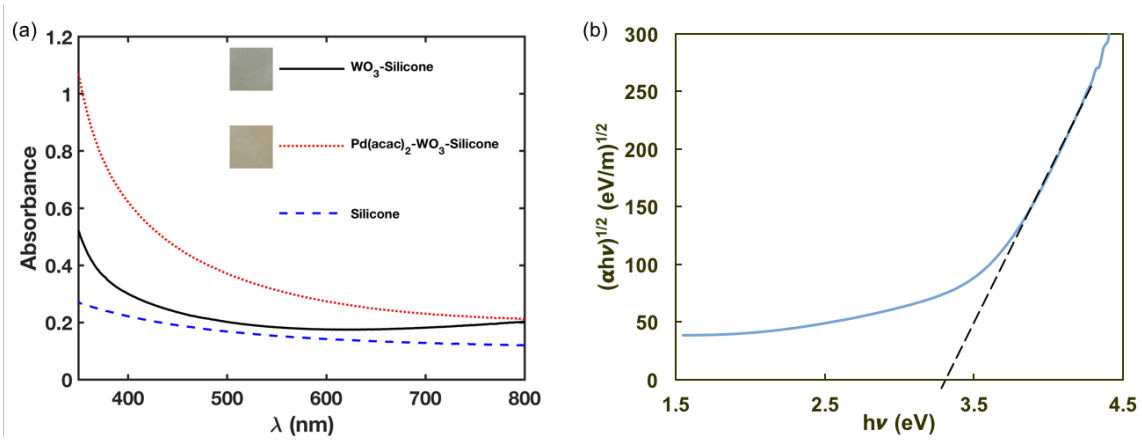

Figure 5.1: (a) Optical absorption spectra for $Pd(acac)_2$-WO_3-silicone, WO_3-silicone, and silicone. The inset shows optical images of $Pd(acac)_2$-WO_3-silicone and WO_3-silicone. (b) Band gap of the WO_3-silicone nanocomposite is determined using the Tauc method.

The infusion of palladium precursor was performed by heating a 10 × 10 × 0.5 mm^3 WO_3-silicone and ∼2 mg of $Pd(acac)_2$ in vacuum at the palladium precursor vaporization temperature (∼413 K) for one hour. The resulting material is designated as $Pd(acac)_2$-WO_3-silicone. Figure 5.1 (a) shows the optical absorption spectra for $Pd(acac)_2$-WO_3-silicone, WO_3-silicone, and silicone for wavelengths between 350 to 800 nm. While the as-received silicone rubber transmits moderately well throughout the visible region, the presence of tungsten oxide particles produces additional absorption in the ultraviolet (UV) and the near infrared (IR) regions causing the material appears to be slight blue (inset image). The blue color indicates that the tungsten oxide is partially reduced since fully oxidized tungsten oxide is relatively transparent in the visible region [151]. The band gap of the WO_3-silicone nanocomposite was determined to be ∼3.2 eV using the Tauc method [152], as shown in Fig. 5.1

(b). After the infusion of $Pd(acac)_2$, the $Pd(acac)_2$-WO_3-silicone sample appeared to have strong absorption in the UV region, and the material became light brown. This change of color comes from the infusion of the $Pd(acac)_2$ chemical precursor since no change in color was found for WO_3-silicone under the same processing environment. The $Pd(acac)_2$-WO_3-silicone sample was taken out of the reaction vessel and cleaned with soap and water. The resulting material was used as the starting material for femtosecond pulsed laser processing.

5.2.2 Pulsed laser processing and characterization

A Ti:sapphire laser (Spectra-Physics Tsunami) operating at the wavelength of 800 nm was used for the optical processing. This wavelength was chosen in order to avoid direct photolysis of the palladium precursor—the palladium precursor does not absorb at 800 nm (Fig. 5.1). The laser pulse duration was approximately 100 fs. The pulse repetition rate was 80 MHz, and the pulse fluence was approximately 6 nJ/cm^2 yielding an average photon flux of 480 mW/cm^2. The $Pd(acac)_2$-WO_3-silicone sample was placed in an evacuated glass vessel ($\sim$160 mTorr), and the sample was irradiated with femtosecond laser pulses at room temperature. The irradiated region turned dark brown after less than three seconds of optical processing indicating significant changes to the material. It should be noted that the irradiated region was damaged and a small hole appeared in the center of the irradiated spot when the optical processing time exceeded three seconds. Similar damage was found on the WO_3-silicone sample.

However, when the silicone rubber was infused with $Pd(acac)_2$ precursor only and the same optical processing conditions were used, there were neither physical nor optical changes to the material.

Since a small amount of palladium precursor was used during the infusion process, verification of the presence of palladium could be challenging. For this reason, imaging and elemental analysis were performed on the irradiated region using scanning transmission electron microscopy (STEM) and energy dispersive X-ray spectroscopy (EDS) allowing high spatial resolution and signal-to-noise ratio. High-angle annular dark-field (HAADF) imaging and EDS analysis were carried out using a 300 kV FEI Tecnai TF-30 transmission electron microscope equipped with a HAADF detector as well as an Oxford EDS detector. The sample drift was minimized by correcting for drift during data acquisition.

5.3 Results and discussion

5.3.1 Particle characterization

Figure 5.2 shows a representative transmission electron microscopy image of WO_3-silicone. Large numbers of spherical and ellipsoid-like tungsten oxide particles were observed throughout the bulk of the silicone matrix. The ellipsoidal particles were relatively large compared to the spherical particles. However, the sizes of the ellipsoidal particles vary considerably—the semi-major axes of the ellipsoidal particles range

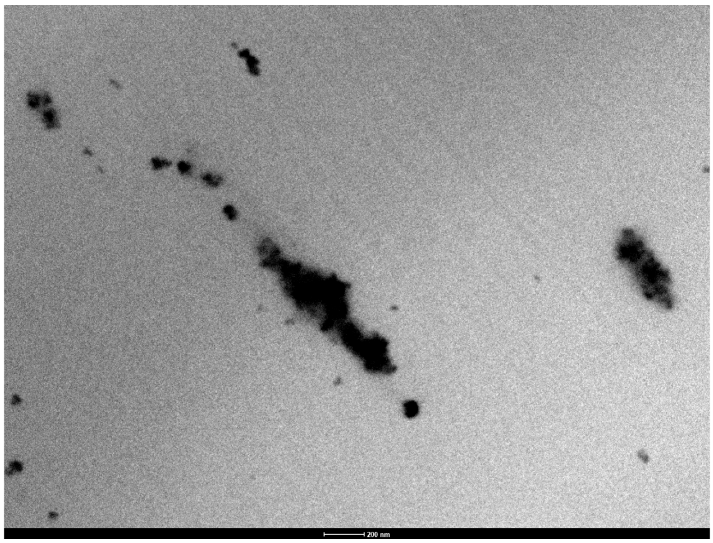

Figure 5.2: A representative transmission electron micrograph of WO_3-silicone.

from 5 to 600 nm. In contrast, the radii of the spherical particles are sized between 5 and 60 nm. These vast differences in particle size and shape are most likely caused by the structure of the silicone matrix [103]. Since the glass transition temperature of the silicone matrix is rather low (∼153 K), the mobility of the polymer chain is high even at room temperature. As a result, the tungsten oxide nanoparticles can move accordingly, and they tend to agglomerate and form larger nanostructures to reduce surface area and surface energy.

Figure 5.3 (b) shows a representative STEM image of the cross section of the irradiated region (dark-brown point in (a)) . Both spherical and ellipsoidal particles are still present in the irradiated region, and the particle spatial and size distributions are similar to that of the WO_3-silicone. Figure 5.3 (c) shows the corresponding EDS spectrum, and the results indicate the presence of palladium, tungsten, and oxygen. The silicon peak resulting from the silicone matrix is also displayed, but unfortunately,

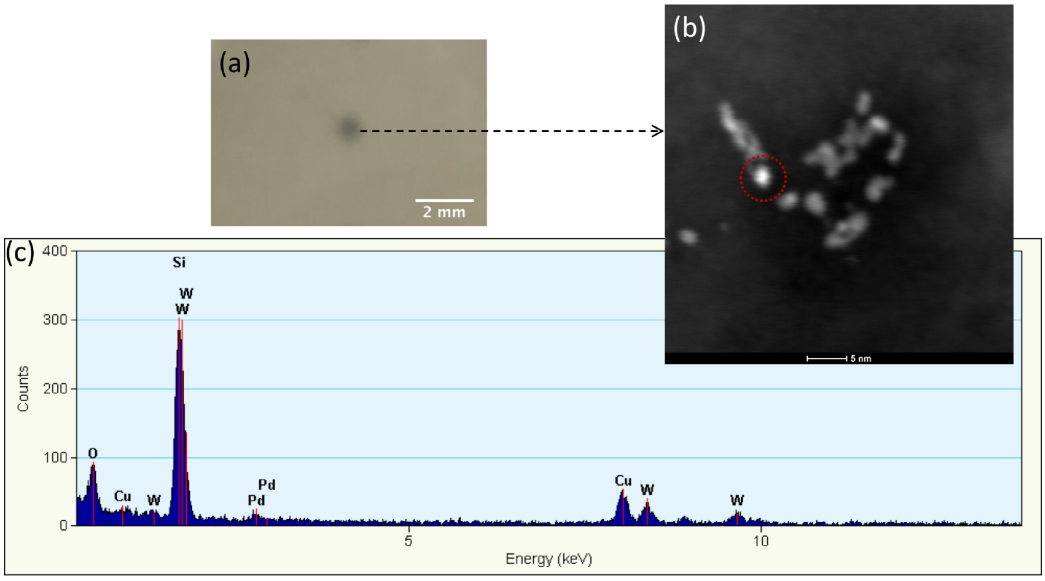

Figure 5.3: (a) Optical images of $Pd(acac)_2$-WO_3-silicone showing a dark spot after less than three seconds of femtosecond pulsed laser irradiation at room temperature; (b) representative HAADF-STEM image showing nanoparticles in the irradiated region; (c) an EDS spectrum showing the detection of palladium, tungsten, and oxygen in the irradiated region.

it overlaps with one of the tungsten peaks. The detection of copper comes from the TEM copper grid. Although the exact location of palladium is undetermined owing to image drift induced by charging, the palladium should appear with bright contrast since it is the heaviest scatterer in this material system. As a result, the relatively bright spot in Fig. 5.3 (b) (marked with a dotted circle) likely consists of palladium, and it appears to be located at the tip of the ellipsoid. The palladium peaks in Fig. 5.3 (c) could only be detected in the irradiated region indicating that the decomposition

of palladium precursor and the subsequent formation of palladium nanostructures are induced by the femtosecond pulsed laser irradiation.

5.3.2 Photo-induced precursor decomposition mechanism

The mechanism for precursor decomposition is some sort of particle-mediated interactions since no evidence supports direct laser photolysis of the precursor. Catalytic decomposition of the precursor could be involved since tungsten oxide is a well-known photocatalyst [153–155], but photothermal particle heating could also lead to precursor decomposition. To identify the main decomposition mechanism, photothermal temperature rises in this system will be calculated in the following sections and use them to assess the likelihood of a photothermal process.

Based on the TEM analysis, the tungsten oxide-silicone nanocomposites consist of mainly spherical and ellipsoidal particles. Because of the differences in sizes and shapes, the photo-induced temperature rises might vary greatly for various particles, and it could be very challenging to adequately describe the temperature fields for each particles. To generalize and simplify the problem, photothermal heating of a spherical particle and an ellipsoidal particle will be considered.

5.3.2.1 Photothermal heating of spherical particle

We consider a system with spherical symmetry consisting of a tungsten oxide nanoparticle and $Pd(acac)_2$ precursor molecules enclosed in a silicone matrix. The nanoparticle is assumed to be spherical with radius of 30 nm (an average spherical par-

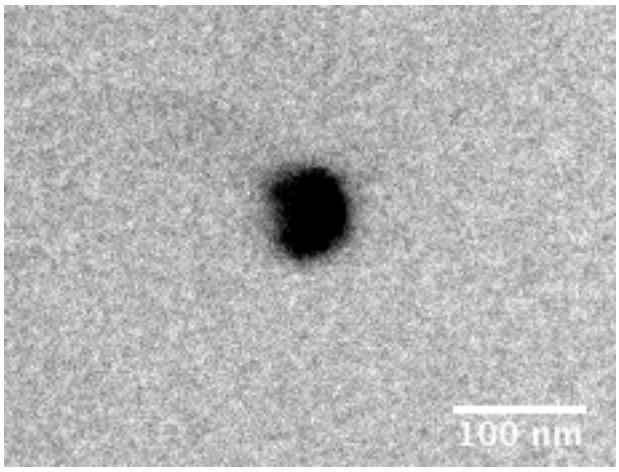

Figure 5.4: A representative transmission electron micrograph of a spherical-like WO_3 nanoparticle.

ticle size obtained from TEM analysis). Figure 5.4 shows a representative TEM image of a spherical-like tungsten oxide nanoparticle. The nanoparticle is photo-excited by a femtosecond laser pulse. This excitation is a series of energy exchange processes that include photon-electron interactions, electron-electron scattering, electron-phonon interactions, and phonon-phonon coupling between the particle and the polymer matrix [156–158]. Thermal excitation of the precursor is assumed to follow the matrix temperature. In addition, the laser pulse is assumed to produce impulse heating of the entire particle. While this is not entirely accurate considering the photon-electron interactions, this assumption is acceptable for time scales related to the chemical reactions that result. Under these assumptions, the material system can be described using the classical thermal diffusion theory, which was detailed in the previous chapter (Chapter 4), and the governing heat diffusion equations can be solved by assuming an initial particle temperature corresponding to adiabatic heating, T_{p0}, which is given

by:

$$T_{p0} = \frac{\Phi \sigma_{abs}}{c_{vp} \rho_p V_p} H(R_p - R) \tag{5.1}$$

where Φ is the laser pulse fluence, σ_{abs} is the absorption cross section of the particle, c_{vp} is the specific heat capacity of the particle, ρ_p is the density of the particle, V_p is the particle volume, $H(R)$ is the Heaviside step function, R_p is the particle radius, and R is the radial distance from the center of the particle. In order to calculate the initial particle temperature, the optical absorption cross section of the particle is needed. For small spherical nanoparticles with radii much smaller than the wavelength of the incident light but larger than 15 nm, the optical absorption cross section can be estimated using Mie theory, and the dipole approximation is given as [134, 159]:

$$\sigma_{abs} = \frac{18\pi V_p \epsilon_m^{3/2}}{\lambda} \frac{\epsilon_2}{(\epsilon_1 + 2\epsilon_m)^2 + \epsilon_2^2} \tag{5.2}$$

where λ is the laser wavelength, and ϵ_1 and ϵ_2 are the real and imaginary parts of the dielectric constant of tungsten oxide, respectively (ϵ_p in Table Table 5.1). Using Eq. (5.2) and the values provided in Table 5.1, the absorption cross section is calculated to be 2.24×10^{-16} m^2 for a $R = 30$ nm spherical tungsten oxide particle.

Table 5.1: Optical Properties of Tungsten Oxide [6] particle as well as Silicone [7] matrix and Specification for Laser Fluence and wavenumber

ϵ_p	ϵ_m	n_m	k_p (1/m)	Φ (nJ/cm^2)
$5.73 + 0.86\,\mathrm{i}$	2.3	1.52	1.19×10^7	6

Calculation of the initial particle temperature is done using the physical property values provided in Table 5.2. While these values are temperature dependent, the variations are small for the temperatures of interest. According to Eq. (5.1), the initial particle temperature resulting from an 800 nm femtosecond laser pulse with a fluence of 6 nJ/cm^2 is expected to be only 4.49 $\times$ 10^{-5} K. However, accumulative heating could be achieved if the time period between laser pulses is shorter than the characteristic relaxation time of the particle. As a result, the spatiotemporal temperature profiles of the material system must be considered.

To construct these temperature profiles, the heat diffusion equation together with the initial and boundary conditions are solved numerically. Results in Fig. 5.5 display 2-D spatial temperature profiles at selected times after particle irradiation, and Fig. 5.6 shows the temporal temperature profiles for various regions inside and outside of the particle. It should be noted that the temperatures have been normalized to the initial particle temperature. These results indicate that only precursor molecules in the close vicinity of the nanoparticle experience increased temperatures. Since the laser pulse repetition rate is 80 MHz (pulse separation is 12.5 ns) and, according to

Table 5.2: Physical Property Values of Tungsten Oxide and Silicone

Material	ρ (kg/m^3)	c_p (J/(kg*K))	κ (W/(m*K))
WO_3	7160	370	1.63
Silicone	1700	1175	1.4

Fig. 5.6, the residual single pulse temperature rise after this time is 2.2% of the initial adiabatic temperature rise in the particle. At regions ∼100 nm away from the particle center, there remains ∼1% of the initial particle temperature before the next pulse arrives. If the system behaves linearly, the peak temperature of the particle for the following pulse will be raised accordingly. However, a steady-state maximum temperature rise for a continuous pulse train will be achieved generally in less than 1 μs. In addition, since the laser pulse width (∼100 fs) is much smaller than the average time needed for heat to diffuse to the neighboring particles (>10 ns), the temperature fields do not overlap. Except maybe In some particular regions where the particles

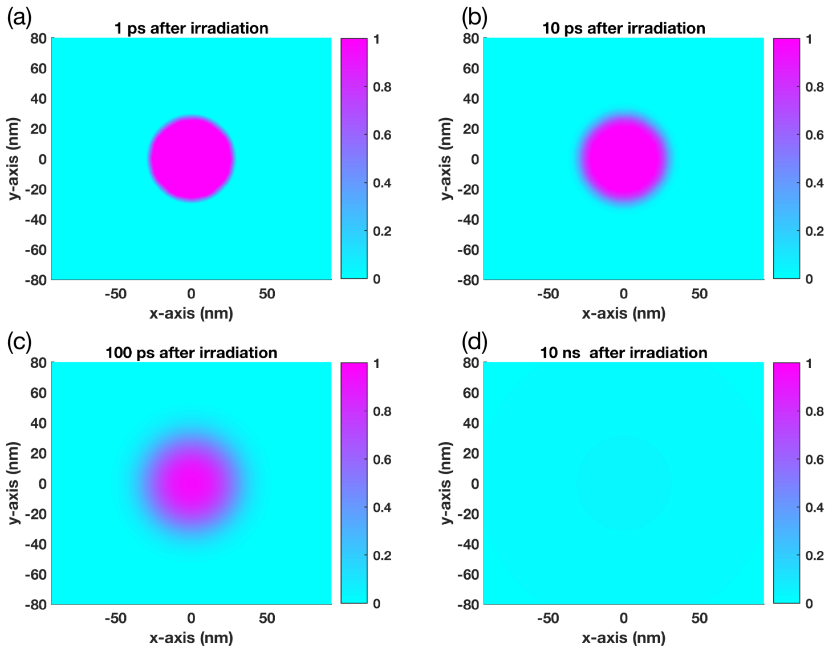

Figure 5.5: Temperature maps showing temperature distribution near a heated nanoparticle (30 nm radius) for (a) 1 ps, (b) 10 ps, (c) 100 ps, and (d) 10 ns after particle irradiation. Temperatures have been normalized by the initial adiabatic temperature rise in the particle, approximately 4.49×10^{-5} K for the conditions assumed in this work.

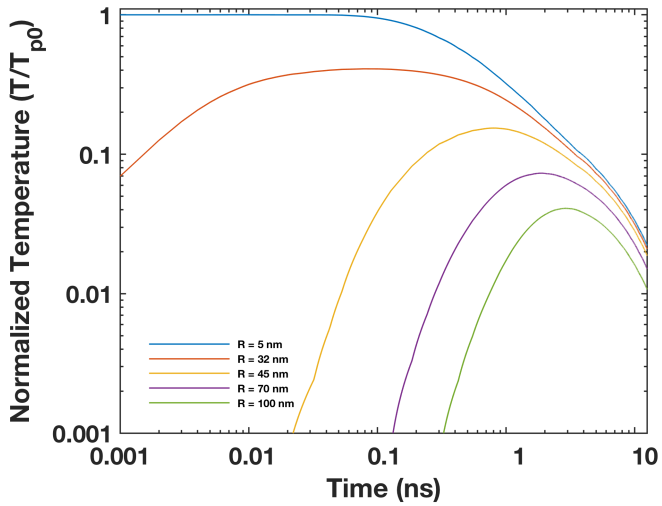

Figure 5.6: Temperature as a function of time for regions 5 nm, 32 nm, 45 nm, 70 nm, and 100 nm away from the particle center (30 nm radius). Temperatures have been normalized by the initial adiabatic temperature rise in the particle.

are very close among each other, the temperature fields could be increased marginally. Figure 5.7 (a) shows two 30 nm nanoparticles 62 nm apart (center to center) 50 ps after a single pulse particle irradiation. The temperature fields overlap causing a relatively slow temperature decrease in the region between these two particles. Approximately 3.6% of the initial particle temperature is retained in this region before the next pulse arrives (Fig. 5.7 (b)). Even when the temperature fields overlap, the corresponding steady-state temperature rise is estimated to be a small fraction of the palladium precursor decomposition temperature. As a result, it is unlikely that decomposition of palladium precursor is induced by photothermal heating of spherical nanoparticles.

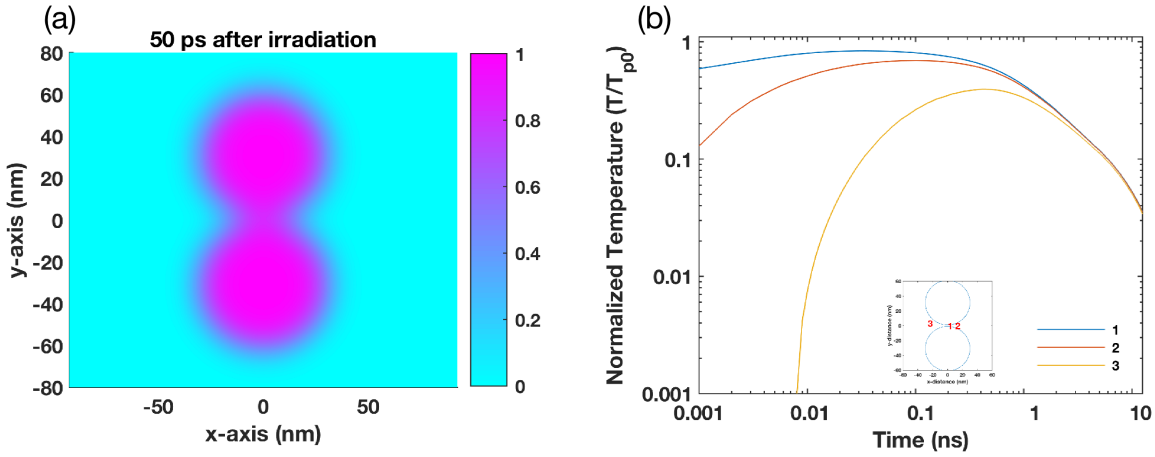

Figure 5.7: (a) A normalized temperature map showing temperature distribution near two heated nanoparticles ($R = 30$ nm), 62 nm apart (center to center), 50 ps after particle irradiation; (b) temperature as a function of time for regions in between two particles. Inset image shows regions of interest.

5.3.2.2 Photothermal heating of ellipsoidal particle

In addition to spherical WO_3 particles, large ellipsoidal WO_3 particles were observed throughout the silicone matrix. Figure 5.8 shows a representative ellipsoid-like WO_3 particle, where the length of the major axis is four times longer than the minor axis. To estimate the adiabatic temperature rise for the ellipsoidal WO_3 particle resulting from a single laser pulse, Eq. (5.1) can be used, but the Heaviside step function has to change from the spherical coordinate to the cylindrical coordinate ($H(R_p - R) \rightarrow H(M^2 + N^2 - R^2)$ where M and N are the semi-major and semi-minor axes of the ellipsoid, respectively). The initial temperature profile is considered uniform inside the ellipsoidal particle since the electron-phonon thermalization occurs faster than the external heat diffusion. To calculate the initial particle temperature using Eq. (5.1), the absorption cross section of the particle is required. However, the

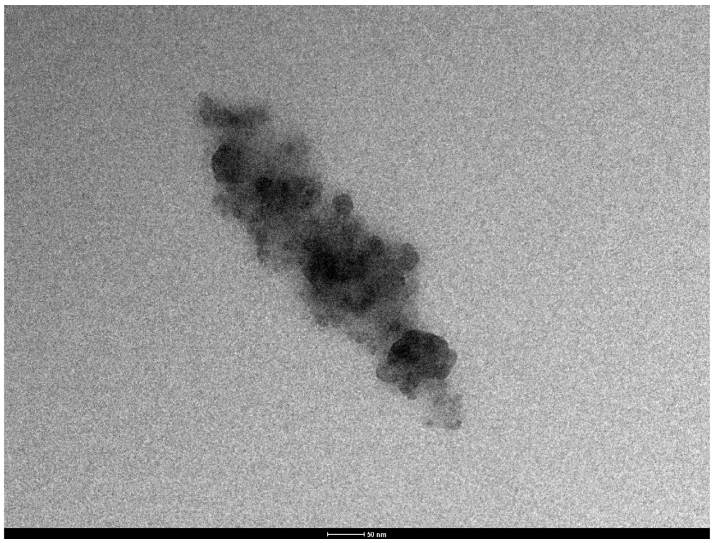

Figure 5.8: A representative ellipsoidal tungsten oxide particle.

previous formalism (Eq. (5.2)) for absorption cross section becomes inadequate since it only applies to spherically-shaped particles. Fortunately, the Mie theory was modified by Gans to describe the dependence of absorption cross section on the aspect ratio of an ellipsoid. The Mie-Gans theory has been successfully applied to various ellipsoidal particle systems [126, 159–162]. Within this model, the absorption cross section is given by:

$$\sigma_{abs} = \frac{2\pi V_p}{3\lambda}\epsilon_m^{3/2}\sum_{j=1}^{3}\frac{(1/P_j^2)\epsilon_2}{\left(\epsilon_1 + \frac{(1-P_j)\epsilon_m}{P_j}\right)^2 + \epsilon_2^2} \tag{5.3}$$

where the depolarization factors, P_j, for the major axis and two minor axes of the ellipsoid are given by:

$$\begin{aligned} P_1 &= \left(\frac{1-e^2}{e^2}\right)\left[\frac{1}{2e}ln\left(\frac{1+e}{1-e}\right) - 1\right], \\ P_2 &= P_3 = \frac{1-P_1}{2} \end{aligned} \tag{5.4}$$

where $e = \left(1 - \frac{N^2}{M^2}\right)^{1/2}$ is the eccentricity. The absorption cross section of an ellipsoidal particle with $M = 285$ nm and $N = 67$ nm (Fig. 5.8) is calculated to be 1.6 $\times$ 10^{-13} m^2 based on Eq. (5.3). As a result, according to Eq. (5.1), this particle is expected to have an initial adiabatic temperature rise of approximately 1.6 $\times$ 10^{-4} K.

Having determined the initial particle temperature and boundary conditions (continuity of temperature and conductive heat flux), numerical simulation is performed to analyze the heat transfer of an ellipsoidal tungsten oxide particle (resembling the one in Fig. 5.8) embedded in a silicone matrix. Results in Fig. 5.9 show 2-D spatial

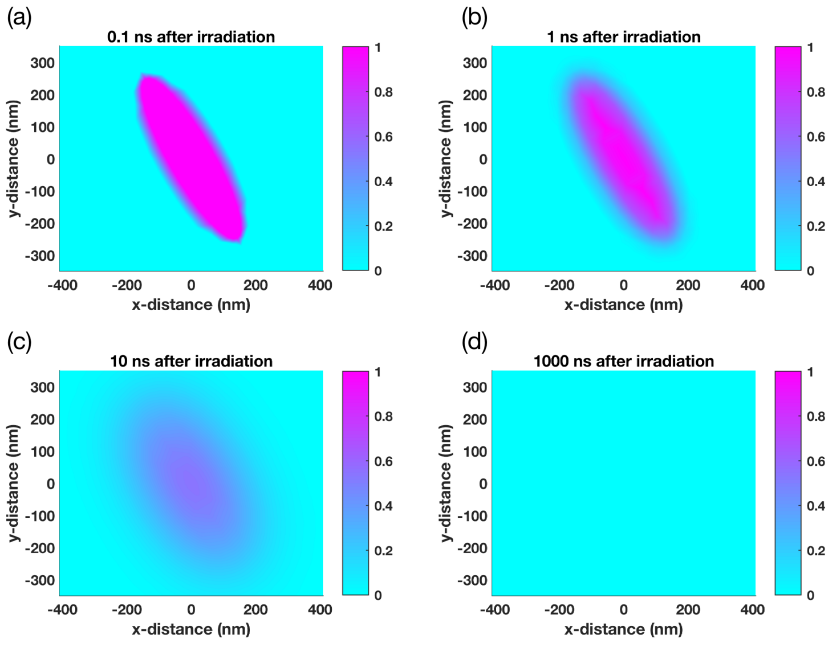

Figure 5.9: Temperature maps showing temperature distribution near a heated ellipsoidal particle ($L = 285$ nm and $W = 67$ nm) for (a) 0.1 ns, (b) 1 ns, (c) 10 ns, and (d) 1000 ns after particle irradiation. Temperatures have been normalized by the initial adiabatic temperature rise in the particle, approximately 1.6 10^{-4} K for the conditions assumed here.

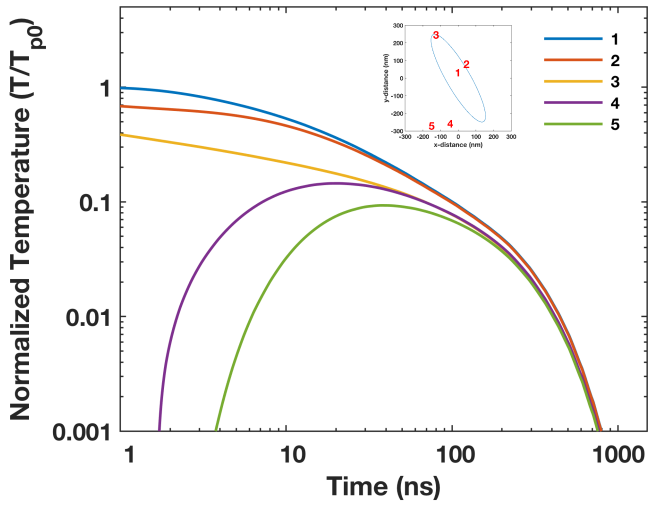

Figure 5.10: Temperature as a function of time for various regions (1-5) inside and outside of the ellipsoidal particle. Inset image shows regions of interest. Temperatures have been normalized by the initial adiabatic temperature rise in the particle.

temperature profiles at selected times after particle irradiation. Figure 5.10 displays the temporal temperature profiles for regions inside and near the particle. The thermal equilibrium between the ellipsoidal particle and the matrix is reached after almost 1 μs. As a result, accumulative heating could be significant since the laser repetition rate is high (80 MHz). Before the arrival of the subsequent laser pulse, different locations relative to the particle exhibit different temperatures: the particle (position 1 in Fig. 5.10) retains nearly 50% of the initial particle temperature; near the surface of the particle (position 2 and 3 in Fig. 5.10) the temperature varies between 20% and 40% of the initial particle temperature; at ∼100-200 nm away from the particle surface (such as position 4 and 5 in Fig. 5.10), these regions possess 5 to 10% of the initial particle temperature. Although the residual single pulse temperate rise is high, a steady-state maximum temperature rise for the ellipsoidal particle is reached after

a few tens of picoseconds and the temperature fields for various ellipsoidal particles do not overlap. Similar to the the spherical particle case, the temperature rise is estimated to be a fraction of the palladium precursor decomposition temperature. As a result, decomposition of palladium precursor is not caused by photothermal heating of ellipsoidal tungsten oxide nanoparticles.

5.3.2.3 Photocatalytic processes

Based on the model results for temperature rises for both spherical and ellipsoidal tungsten oxide particles, thermally induced decomposition of the palladium precursor is highly unlikely and other mechanisms must be considered. Since tungsten oxide is a well-known photocatalyst [153, 155, 163, 164], some type of catalytically driven decomposition of precursor could be accomplished through particle irradiation. The band gap of the tungsten oxide nanocomposites was determined to be ∼3.2 eV (Fig. 5.1 (b)), and this value is within the literature value range of stoichiometric WO_3, between 3.0 eV and 3.3 eV [165, 166]. However, since stoichiometric WO_3 is optically transparent, the blue color of WO_3-silicone indicates that the presence of oxygen vacancies (non-stoichiometric WO_3) [167]. These oxygen vacancies result in defect states in the band gap of WO_3 and act as optical centers involved in sub-gap electronic transitions. To photo-excite the WO_3 particles, single photon energy is not sufficient—the wavelength of the laser corresponds to the excitation photon energy of 1.55 eV. This value is well below the band gap of tungsten oxide. However, multiphoton excitation could be involved. The nonlinear optical response of tungsten oxide

has been studied and is known to be strong for the wavelength used here [168–170]. In addition, pulsed illumination can increase multiphoton absorption efficiency owing to its square dependence on intensity [171]. Unfortunately, the photocatalytic processes in tungsten oxide nanoparticles have not been studied in sufficient detail, the mechanisms responsible for precursor decomposition can only be inferred for this material system. However, regardless of the photo-induced decomposition mechanisms, the catalytic decomposition processes occur fairly fast—the palladium nanoparticles formed within a few seconds of laser irradiation. Further laser exposure could deteriorate the silicone matrix, and this is most likely caused by photothermal heating of the palladium nanoparticles as well as photocatalytic scission of the silicone polymer chains.

5.4 Conclusion

In this chapter, we modified the particle composition in silicone matrix nanocomposites containing tungsten oxide particles as well as a palladium precursor using femtosecond pulsed laser excitation. Optical excitation of the nanocomposites resulted in local decomposition of precursor and subsequent deposition of palladium in the vicinity of the tungsten oxide particles. On the basis of interpretation of the transmission electron micrographs as well as elemental analysis, the surfaces of the tungsten oxide particles were decorated with palladium nanoparticles. Temperature rises in the near-particle regions was calculated, and the results indicate that

photothermal processes are not responsible for precursor decomposition. Multiphoton, photocatalytic processes are most likely the main cause for the decomposition. The overall processing approach here demonstrates the potential for localized, *in situ* modification of nanostructures in polymer matrices.

Chapter 6

Functional Polymer Matrix Nanocomposites

6.1 Introduction

The aim of this chapter is to demonstrate the technical feasibility of creating functional polymer matrix nanocomposites using the thermal and optical processing methods described in the previous chapters. In particular, optically-based sensing materials for gas sensing applications were synthesized using the chemical infusion method. Tungsten oxide and molybdenum oxide-based polymer matrix nanocomposites were chosen as the sensing materials since these oxides can be readily reduced, changing their optical absorption behaviors [172–174]. The alcohol vapor sensing ability was demonstrated in PMNCs containing tungsten oxide nanoparticles, molybdenum oxide nanoparticles, and a mixture of the oxide nanoparticles. For hydrogen gas sensing, a mixture of palladium and tungsten oxide nanoparticles were synthesized since palladium has the ability to dissociate hydrogen molecules. These hybrid nanoparticles are embedded in two different polymer matrices to study the effect

of polymer matrix on detection of hydrogen gas. In the case of optical processing, formation of palladium nanoparticles was performed at selective regions of the tungsten oxide-based nanocomposites using a femtosecond pulsed laser source, forming patterned structures of functional materials.

6.2 Materials, processing, and characterization

Tungsten hexacarbonyl ($W(CO)_6$; 97%; Sigma-Aldrich), molybdenum hexacarbonyl ($Mo(CO)_6$; 97%; Sigma-Aldrich), and palladium(II) acetylacetonate ($Pd(acac)_2$; 99% Pd; Sigma-Aldrich) were used as precursors for preparing tungsten oxide, molybdenum oxide, and palladium nanoparticles, respectively. These precursors were used in their as-received state without further preparation. A semicrystalline tetrafluoroethylene-co-hexafluoropropylene (FEP; CS Hyde) and a high-temperature silicone rubber (McMaster-Carr Supply) were chosen as the polymer matrices.

Five different polymer matrix nanocomposites were synthesized using the chemical infusion technique, and these materials were designated as MoO_3-FEP, WO_3-FEP, MoO_3-WO_3-FEP, Pd-WO_3-silicone, and Pd-WO_3-FEP. The synthesis conditions for each precursor used are shown in Table 6.1. In general, ∼100 mg of tungsten hexacarbonyl and molybdenum hexacarbonyl were used for each infusion. A small amount (∼2-5 mg) of palladium(II) acetylacetonate was used since palladium nanoparticles exhibit strong optical absorption, and producing excessive palladium would result in complete darkening of the nanocomposites. For materials containing two parti-

cle components, such as MoO_3-WO_3-FEP, two subsequent infusion processes were performed.

Table 6.1: Synthesis conditions for precursor chemicals used in the chemical infusion processes

Precursor	T_{vap} (°C)	t_{vap} (hour)	T_{decomp} (°C)	t_{decomp} (hour)
$Mo(CO)_6$	120	2	160	2
$W(CO)_6$	130	2	180	3
$Pd(acac)_2$	140	2	200	2

For femtosecond pulsed processing, similar to synthesis described in the previous chapter, tungsten oxide-silicone matrix nanocomposites containing $Pd(acac)_2$ was used as the starting materials. Figure 6.1 shows the experimental setup for patterning of polymer matrix nanocomposites. A mode-locked Ti:sapphire laser (Spectra-Physics Tsunami) beam was used as the optical excitation source. The laser light was collimated with a fiber optic collimation lens (not shown in Fig. 6.1), and the resulting beam was then coupled into a multi-mode optical fiber. The optical fiber was placed on a fiber adapter, and the adapter was fixed on a two-axis motorized stage. The position and the movement of the fiber-coupled laser can be remotely controlled by programming the motorized stage. A vacuum-sealed vessel (containing the starting materials) was placed behind the motorized stage, and patterning of polymer matrix nanocomposites was achieved by directing the laser beam across the nanocomposites.

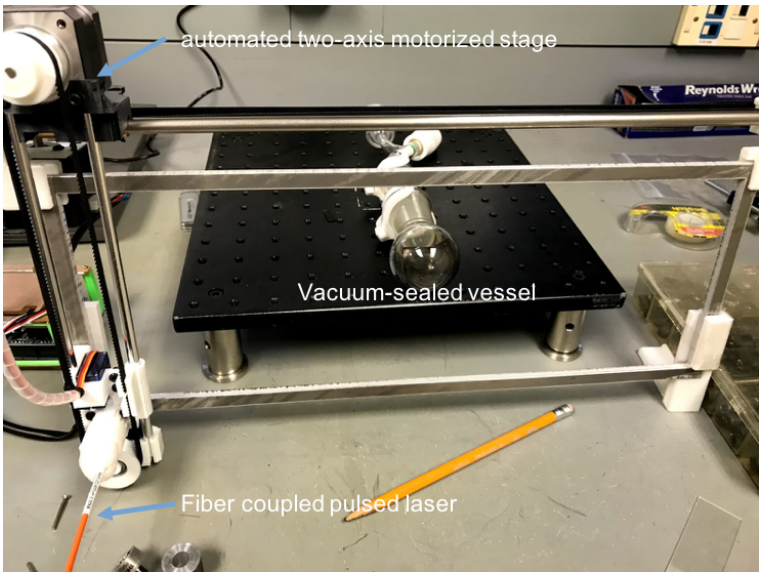

Figure 6.1: Experimental setup for patterning of polymer matrix nanocomposites.

Three different nanocomposites, MoO_3-FEP, WO_3-FEP, and MoO_3-WO_3-FEP, were used as alcohol vapor sensing materials (Methanol, ethanol, and isopropanol solutions were used). In a typical experiment, the nanocomposite was placed in a glass beaker (with lid) along with a few drops of alcohol. The container was then put in a 100 °C oven to vaporize the alcohol—all the alcohols used have boiling points less than 100 °C. After less than 5 minutes, the nanocomposites were taken out of the container to examine their optical absorption characteristics using UV-Vis spectroscopy (PerkinElmer Lamda 950UV/Vis). For the detection of hydrogen gas, Pd-WO_3-silicone and Pd-WO_3-FEP nanocomposites were used. These materials were placed in a glass reaction vessel that was backfilled with forming gas (5 vol% of H_2 and 95% of Ar). The color changes of the nanocomposites were recorded. Nanocomposites were characterized using transmission electron microscopy (TEM)

and scanning transmission electron microscopy (STEM).

6.3 Results and discussion

6.3.1 Optical sensing materials for alcohol vapors

As-synthesized MoO_3-FEP, WO_3-FEP, and MoO_3-WO_3-FEP are optically transparent. Figure 6.2 (a) shows their optical transmission spectra for wavelengths between 350 to 800 nm. The as-received FEP is also included for comparison purposes. All the metal oxide nanocomposites exhibit strong absorption in the UV region (below 400 nm) indicating the presence of metal oxide particles. Figure 6.2 (b) shows a representative TEM image of WO_3-FEP. These nanoparticles are roughly spherical with radii ranging from 2 to 8 nm.

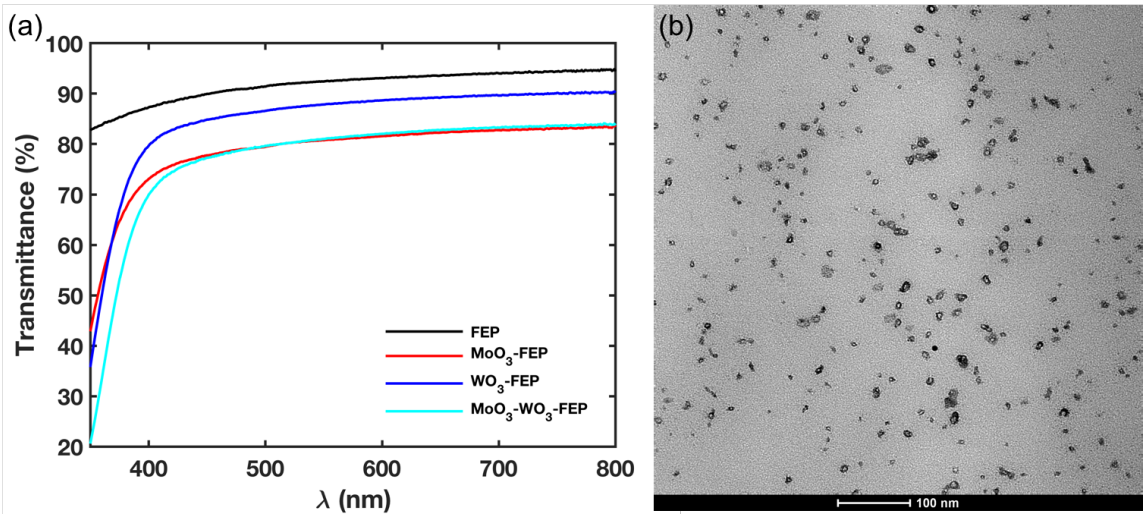

Figure 6.2: (a) Optical transmission spectra for FEP, MoO_3-FEP, WO_3-FEP, and MoO_3-WO_3-FEP; (b) a representative TEM image showing tungsten oxide nanoparticles.

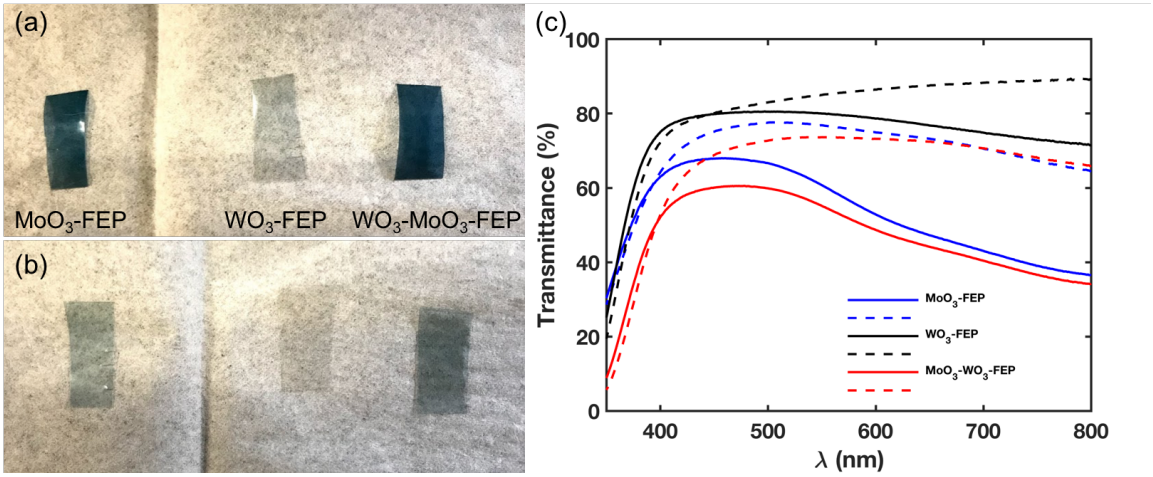

Figure 6.3: Optical images of MoO_3-FEP, WO_3-FEP, and MoO_3-WO_3-FEP (a) after placing in a methanol vapor environment and (b) after heating in a 160 °C, air circulating oven. (c) Optical transmission spectra for MoO_3-FEP (blue curves), WO_3-FEP (black curves), and MoO_3-WO_3-FEP (red curves); solid lines represent colored states, and dashed lines represent bleached states.

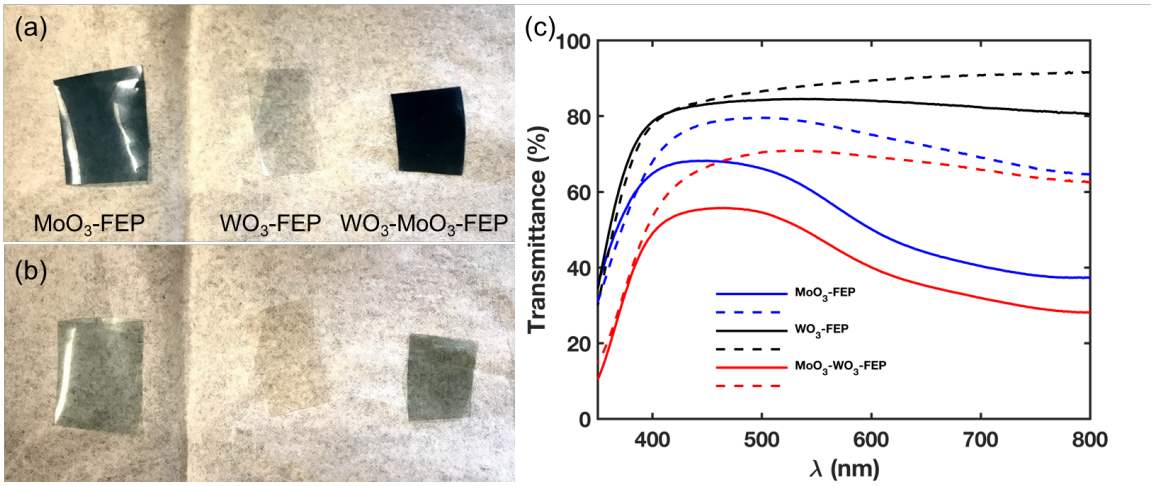

Figure 6.4: Optical images of MoO_3-FEP, WO_3-FEP, and MoO_3-WO_3-FEP (a) after placing in an ethanol vapor environment and (b) after heating in a 160 °C, air circulating oven. (c) Optical transmission spectra for MoO_3-FEP (blue curves), WO_3-FEP (black curves), and MoO_3-WO_3-FEP (red curves); solid lines represent colored states, and dashed lines represent bleached states.

Figure 6.3, 6.4, and 6.5 display the gasochromic behaviors of the metal oxide nanocomposites in methanol, ethanol, and isopropanol vapors, respectively. Regard-

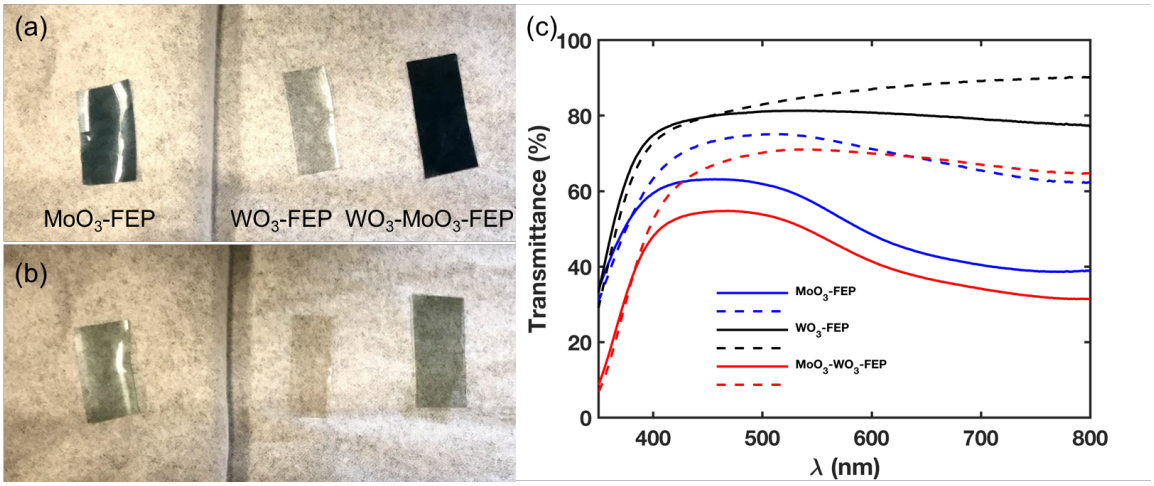

Figure 6.5: Optical images of MoO_3-FEP, WO_3-FEP, and MoO_3-WO_3-FEP (a) after placing in an isopropanol vapor environment and (b) after heating in a 160 °C, air circulating oven. (c) Optical transmission spectra for MoO_3-FEP (blue curves), WO_3-FEP (black curves), and MoO_3-WO_3-FEP (red curves); solid lines represent colored states, and dashed lines represent bleached states.

less of the alcohol used, changes in coloration are similar (Fig. 6.3 (a), 6.4 (a), and 6.5 (a)): MoO_3-WO_3-FEP turned deep blue; MoO_3-FEP turned moderate blue; WO_3-FEP turned slight blue. At room temperature, these nanocomposites remain in their colored states. Switching to their bleached states requires putting the nanocomposites in a high-temperature environment. Figure 6.3 (b), 6.4 (b), and 6.5 (b) show optical images of materials in their bleached states after heating in a 160 °C oven for ∼5 minutes. Although the materials could not transform back to their initial transparent states (complete bleaching), significant transmission changes between the bleached and colored states can be observed. The optical absorption variations are illustrated in the UV-Vis spectra (Fig. 6.3 (c), 6.4 (c), and 6.5 (c)), and the largest changes between the bleached and colored states are found in MoO_3-WO_3-FEP. The col-

oration/bleaching transition was repeated over ten cycles, and no loss of gasochromic effect was observed.

The complete mechanism of the gasochromic processes is not fully understood. However, there are two models widely accepted and referenced in the literature. One suggests that the coloration/bleaching is related to the injection/extraction of hydrogen ions and electrons [175–177], while the other suggests the creation/annihilation of oxygen vacancies [178]. When the tungsten oxide particles are exposed to the alcohol vapors (reducing gases), the alcohol molecules adsorb on the surface tungsten atoms of the tungsten oxide particles via the oxygen atoms of the hydroxyl groups. The alcohol molecules act as electron donors, which interact with electron holes in the valence bands of tungsten oxide. The oxidation of alcohol with the electron holes produces hydrogen ions (H^+) and aldehydes or ketone. The resulting hydrogen ions can interact with the electrons in the conduction bands to generate hydrogen atoms [179, 180]. Depending on the model, the hydrogen atoms can either diffuse into the interior of the tungsten oxide lattice and form H_xWO_3 or react with the surface-oxygen and create oxygen vacancies that diffuse into the material. Figure 6.6 illustrates the two possible alcohol sensing mechanisms of tungsten oxide. The formation of tungsten bronze (H_xWO_3) and vacancy-defected tungsten oxide can both result in the coloration of materials. To bleach the nanocomposites, the reactions have to be reversed and sufficient oxygen is needed. The self-bleaching processes are unlikely at room temperature since the oxygen solubility in the FEP matrix is fairly

low (2.4×10^3 cm^3 (STP)/(cm^3 cmHg) [181]). Bleaching can be achieved at elevated temperature (> the glass transition temperature of FEP) so that oxygen molecules can readily reach the tungsten oxide particles. However, complete recovery of the original transparent state could not be accomplished, and this is possibly due to that the hydrogen ions or oxygen vacancies trapped in the tungsten oxide particles [182].

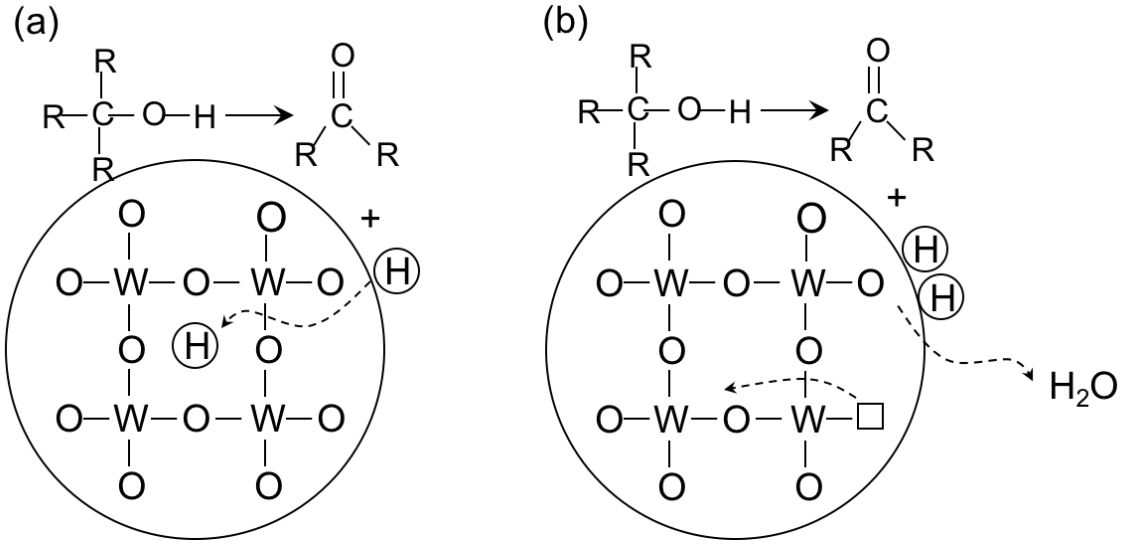

Figure 6.6: Two possible coloration mechanisms for tungsten oxide particles exposing to alcohol vapors: (a) injection of hydrogen atoms and (b) creation of oxygen vacancies. R is a functional group that attaches to the carbon atom. Depending on the alcohol molecule, the R group can be an alkyl group or a hydrogen.

6.3.2 Optical sensing materials for hydrogen gas

As-synthesized Pd-WO_3-silicone and Pd-WO_3-FEP are brown and slightly brown, respectively. After exposing the materials to the forming gas at room temperature, Pd-WO_3-silicone and Pd-WO_3-FEP turned dark green and blue, respectively. While it takes ~3 seconds for the Pd-WO_3-silicone change to its colored state in ambi-

ent conditions, Pd-WO_3-FEP takes roughly 15 seconds. The gasochromic effect on both materials is reversible, and it takes about the same amount of time to transform back to their bleached states as to their colored states. Figure 6.7 and 6.8, respectively, show optical images of Pd-WO_3-silicone and Pd-WO_3-FEP in their (a) bleached states and (b) colored states. Unlike the optical sensing materials for alcohol vapors, Pd-WO_3-silicone and Pd-WO_3-FEP are able to fully recover their initial optical transparency upon bleaching. The gasochromic effect did not weaken after repeated coloration/bleaching cycles.

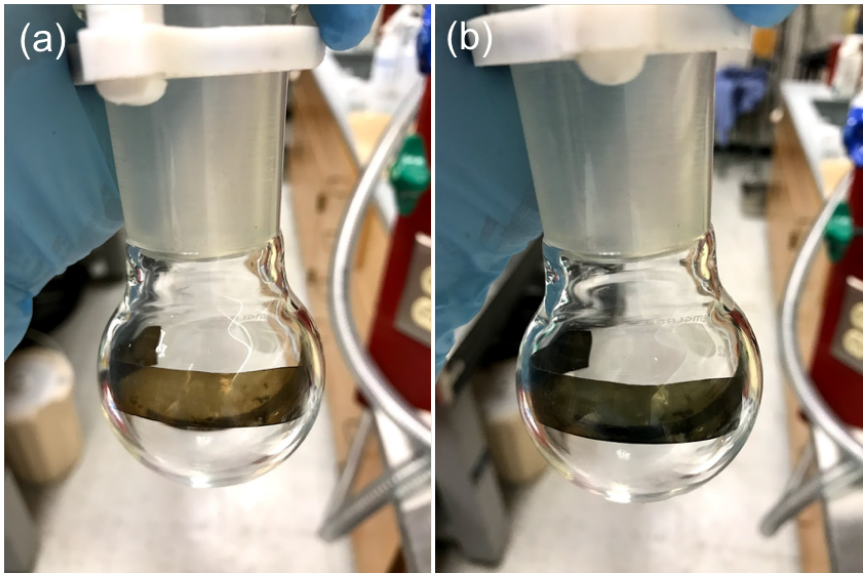

Figure 6.7: Optical images of Pd-WO_3-silicone (a) after exposing to forming gas (5 vol% of H_2 and 95% of Ar) and (b) to air at room temperature.

Figure 6.9 shows a patterned, hydrogen gas sensing material, where a letter "H" was directly written on it using a controlled fiber-coupled laser. The optical transmission of the patterned material changes significantly from air (a) to forming gas (b)—the letter "H" changes from light brown to dark. The gasochromic responses of this

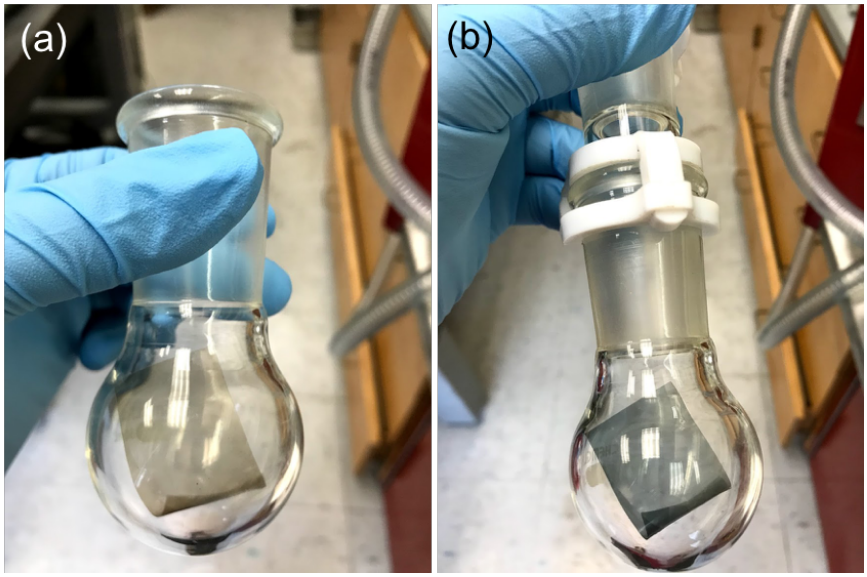

Figure 6.8: Optical images of Pd-WO_3-FEP (a) after exposing to forming gas (5 vol% of H_2 and 95% of Ar) and (b) to air at room temperature.

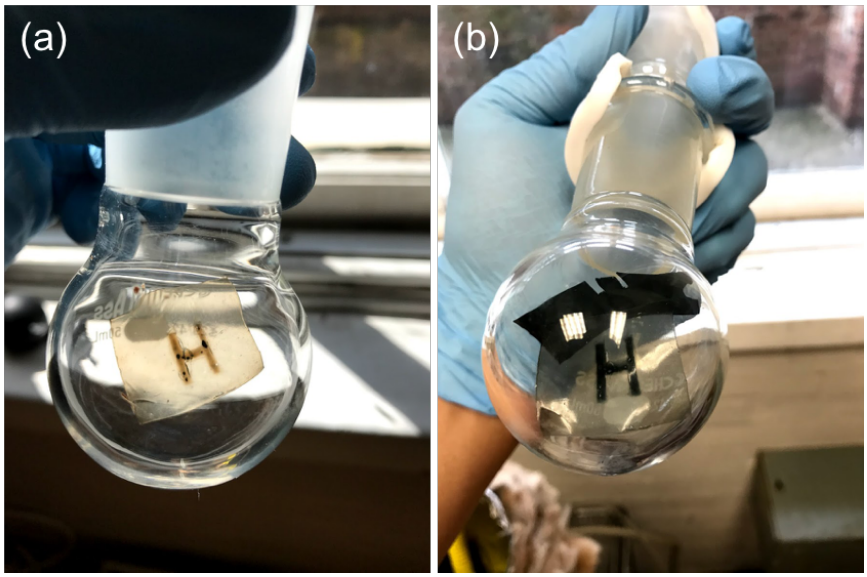

Figure 6.9: (a) A laser-patterned, optical hydrogen sensing material (Pd-WO_3-silicone) in air and (b) in forming gas (5 vol% of H_2 and 95% of Ar).

patterned material are fully reversible and repeatable at room temperature, and both the coloring as well as bleaching reactions occur within five seconds. Figure 6.10 shows

representative STEM images of (a) a thermally processed Pd-WO_3-silicone (Fig. 6.7) as well as (b) a laser-processed Pd-WO_3-silicone (Fig. 6.9). Both nanocomposites contain a large amount of string-like or ellipsoidal particles dispersed throughout the bulk of the materials, and they exhibit similar particle size and spatial distribution. However, different distributions of palladium nanoparticles were found by locating the bright regions on the STEM images—these regions are believed to consist of palladium. For the optically-processed materials, the palladium nanoparticles were in the immediate vicinity of the tungsten oxide particles. For the thermally-processed materials, while the majority of the palladium nanoparticles were located near the tungsten oxide particles, some were also found in regions consisting of no tungsten oxide.

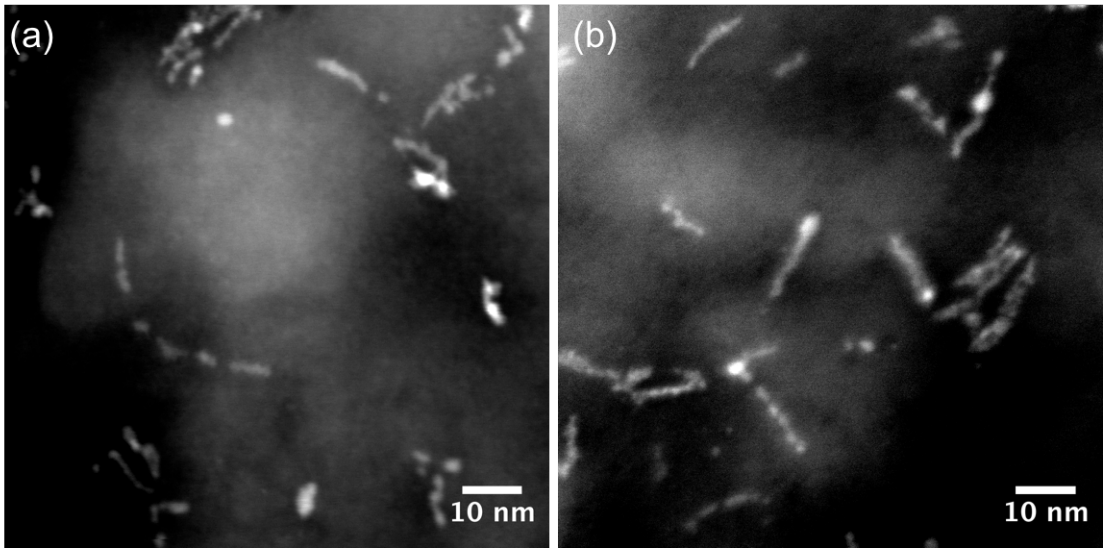

Figure 6.10: Representative STEM images of (a) thermally processed Pd-WO_3-silicon and (b) optically processed Pd-WO_3-silicone.

The gasochromic response for hydrogen gas is different than that for alcohol vapors

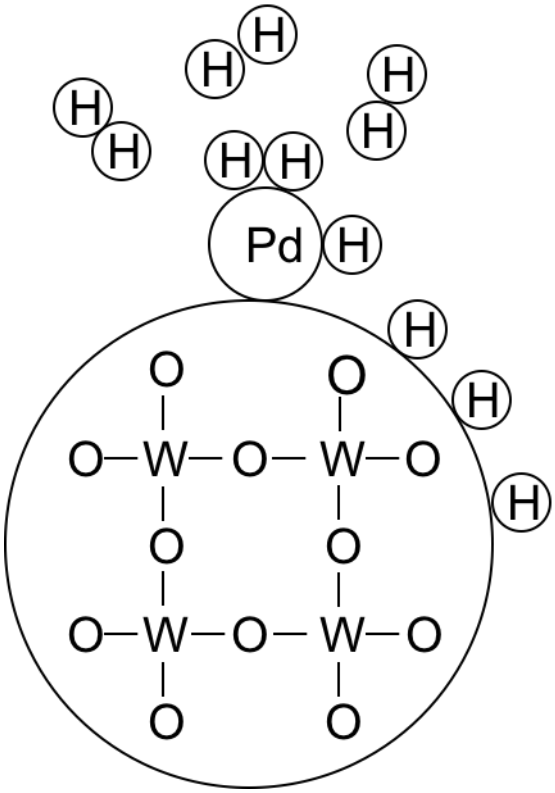

Figure 6.11: Gasochromic mechanism for palladium-decorated tungsten oxide particles exposing to hydrogen gas.

since the material for hydrogen sensing is a hybrid of tungsten oxide and palladium. It is well known that palladium can dissociate hydrogen molecules since the Pd-H bonds are more stable than the H-H bonds [183, 184]. Even at room temperature, the H_2 molecules can readily dissociate on the palladium surface. If the palladium particles are attached to the tungsten oxide particles, the dissociated hydrogen can diffuse onto the surface or subsurface of the tungsten oxide particles forming H_xWO_3 [185]. Figure 6.11 illustrates the gasochromic mechanism for hydrogen gas. Since the reactions occur at room temperature, the probability of hydrogen atoms having sufficient energy to diffuse into the interior of the tungsten oxide lattice (or oxygen

vacancies in tungsten oxide) is low. As a result, the hydrogen can readily desorb from the tungsten oxide surface after placing the nanocomposites in the atmosphere, and the nanocomposites can subsequently recover to their initial optical transparency. The coloration/bleaching response time is different for Pd-WO_3-FEP and Pd-WO_3-silicone, and this difference is mainly caused by the difference in gas permeability between the silicone and FEP matrices. Pd-WO_3-silicone responds faster than that for Pd-WO_3-FEP because the gas permeability for silicone is much greater than that of FEP—the hydrogen permeability of silicone and FEP is, respectively, 65×10^{-9} and 1.3×10^{-9} cm^3 (STP) cm/(cm^2 cmHg s) [186].

6.4 Conclusion

Gasochromic polymer matrix nanocomposites were synthesized using the chemical infusion method and the femtosecond pulsed laser processing method. Optical sensing of alcohol vapors as well as hydrogen gas were demonstrated, and the associated coloration/decoloration processes were discussed. Results indicate that multifunctional polymer matrix nanocomposites can be made by incorporating specific particles into the polymer matrices, allowing optimization of particle chemistries for particular applications. Macroscopic patterning of functional polymer matrix nanocomposites was also demonstrated, and the results suggest that it is possible to achieve micro or even nano-scaled patterning with precise and sophisticated control of thermal and optical processing.

Chapter 7

Conclusion

This thesis focused on the experimental design and data interpretation of the thermal and optical processing effects on nanoparticle formation in polymer matrices. These studies were pursued in an attempt to gain a better understanding of the material physics that are involved in various processing conditions. This understanding can provide valuable information for scalable implementation as well as designing and creating polymer matrix nanocomposites with desired properties.

The objective of the first half of the thesis was to thoroughly characterize and interpret the physical and chemical processes involved in the thermal synthesis of polymer matrix nanocomposites. This highly scalable thermal processing method termed chemical infusion consists of vaporizing particle-precursor, infusing the precursor into a polymer matrix, decomposing the precursor, and subsequently forming nanoparticles within the polymer. Palladium-PFA nanocomposites were chosen to study the phenomena of precursor diffusion as well as particle formation. It was

found that the structure of the polymer matrix plays an important role on precursor diffusion and consequently particle formation. Significant differences in precursor diffusion behaviors as well as particle size and spatial distribution were observed between nanocomposites synthesized using as-received PFA and heat-treated PFA. These differences were interpreted using a polymer free volume model to develop insight into the precursor diffusion processes. In addition to studying precursor diffusion, the nucleation and growth of palladium nanoparticles in PFA were investigated by creating a series of TEM samples that effectively capture particle sizes and distributions as a function of processing times. The nucleation of nanoparticles was correlated with defects in the polymer matrix, and the growth of nanoparticles was described using a modified diffusion-limited growth model. It was also found that processing temperature is an important factor for nanoparticle formation. When an appropriate processing temperature is used, nearly monodisperse particles are formed throughout the polymer matrix. Higher processing temperatures result in larger particles, however, if the synthesis temperature is sufficiently high, near-surface percolation of nanoparticles occurs because of high precursor decomposition and diffusion rates.

The objective of the second half of the thesis was to study the linear and nonlinear optical processing methods for *in situ* modification of nanoparticles. Optical excitation was performed on polymer matrix nanocomposites containing nanoparticles as well as precursor. The photo-induced, particle-mediated interactions result in decomposition of the precursor in the irradiated region and subsequently modifi-

cation of the particles. In particular, continuous wave laser was used to modify the particle size and number density in polymer matrix nanocomposites containing palladium nanoparticles and palladium precursor. The steady-state temperature rises in the irradiated regions were calculated, and results suggested that the temperature rises can facilitate the precursor diffusion as well as precursor decomposition. In addition to continuous wave laser processing, femtosecond pulsed laser excitation was also used to modify the particle composition locally in silicone matrix nanocomposites containing tungsten oxide particles as well as palladium precursor. TEM and EDS studies suggested that the tungsten oxide particles were decorated with the palladium nanoparticles in the silicone matrix. Expected temperature rises in the near-particle regions were found to be far too low to cause changes in materials. Decomposition of palladium precursor most likely occurred as a result of photocatalytic interactions with the tungsten oxide particles.

Optically-based gas sensing materials were produced using both thermal and optical processing methods. Tungsten oxide and molybdenum oxide nanoparticles were synthesized in the FEP as well as silicone matrices, and the resulting materials exhibited excellent gasochromic performance for alcohol vapors. Polymer matrix nanocomposites consisting of both palladium and tungsten oxide nanoparticles presented fast and reversible gasochromic responses for hydrogen gas. In addition, it was found that optical patterning of nanocomposites can be achieved by controlling and moving the laser excitation source. Instead of gasochromic materials, other functional polymer

matrix nanocomposites can also be synthesized by choosing the particle material and polymer matrix appropriately. For example, photocatalytic nanocomposites for water purification applications can be synthesized by growing photocatalytic particles (such as titanium oxide) in hydrophilic polymer matrices (such as Nafion).

In summary, a scalable and versatile chemical infusion method was shown to be capable of producing various multifunctional polymer matrix nanocomposites since a wide variety of chemical precursors are readily available. The processing temperature and the morphology of the polymer matrix are critical factors for growing nanoparticles in a solid polymer matrix. Both linear and nonlinear optical excitation can be used to modify particle size, number density, and composition. Macroscopic optical patterning of polymer matrix nanocomposites has been successfully demonstrated, and these promising results indicate that laser direct-writing of periodic structures on a micro scale and on a nano scale inside a polymer composite could be achieved if the spatial and temporal profiles of the laser irradiation are precisely controlled.

References

[1] T. J. DeJournett, J. B. Spicer, Laser-induced, in situ, nanoparticle shell synthesis in polymer matrix nanocomposites, Physical Chemistry Chemical Physics 15 (45) (2013) 19753.

[2] T. J. DeJournett, J. B. Spicer, The influence of oxygen on the microstructural, optical and photochromic properties of polymer-matrix, tungsten-oxide nanocomposite films, Solar Energy Materials and Solar Cells 120 (2014) 102–108.

[3] DuPont, Teflon ® PFA Properties Handbook, DuPont, 1996.

[4] R. French, J. Rodríguez-Parada, M. Yang, R. Derryberry, N. Pfeiffenberger, Optical properties of polymeric materials for concentrator photovoltaic systems, Solar Energy Materials and Solar Cells 95 (8) (2011) 2077–2086.

[5] P. Johnson, R. Christy, Optical constants of transition metals: Ti, V, Cr, Mn, Fe, Co, Ni, and Pd, Physical Review B 9 (12) (1974) 5056–5070.

[6] H. Demiryont, K. E. Nietering, Tungsten oxide films by reactive and conven-

tional evaporation techniques, Applied Optics, Vol. 28, Issue 8, pp. 1494-1500 28 (8) (1989) 1494–1500.

[7] L. Yu, F. B. Madsen, S. Hvilsted, A. L. Skov, Dielectric elastomers, with very high dielectric permittivity, based on silicone and ionic interpenetrating networks, RSC Adv. 5 (61) (2015) 49739–49747.

[8] J. Njuguna, K. Pielichowski, Polymer Nanocomposites for Aerospace Applications: Properties, Advanced Engineering Materials 5 (11) (2003) 769–778.

[9] A. K. Naskar, J. K. Keum, R. G. Boeman, Polymer matrix nanocomposites for automotive structural components, Nature Nanotechnology 11 (2016) 1026.

[10] A. Rasheed, F. A. Khalid, Fabrication and properties of CNTs reinforced polymeric matrix nanocomposites for sports applications, in: International Symposium on Advanced Materials, 2014, p. 012009.

[11] F. Gao, Clay/polymer composites: the story, Materials Today 7 (11) (2004) 50–55.

[12] Gao F. (Ed.), Advances in polymer nanocomposites : types and applications, Woodhead, 2012.

[13] S. Li, M. Meng Lin, M. S. Toprak, D. K. Kim, M. Muhammed, Nanocomposites of polymer and inorganic nanoparticles for optical and magnetic applications, Nano reviews 1 (2010) 5214.

[14] F. Hussain, Polymer-matrix Nanocomposites, Processing, Manufacturing, and Application: An Overview, Journal of Composite Materials 40 (17) (2006) 1511–1575.

[15] M. Oliveira, A. V. Machado, Preparation of polymer-based nanocomposites by different routes, Nanocomposites: synthesis, characterization and applications (2013) 1–22.

[16] E. M. Hotze, T. Phenrat, G. V. Lowry, Nanoparticle Aggregation: Challenges to Understanding Transport and Reactivity in the Environment, Journal of Environment Quality 39 (6) (2010) 1909.

[17] S. Qu, C. Du, Y. Song, Y. Wang, Y. Gao, S. Liu, Y. Li, D. Zhu, Optical nonlinearities and optical limiting properties in gold nanoparticles protected by ligands (2002).

[18] U. Schurmann, W. Hartung, H. Takele, V. Zaporojtchenko, F. Faupel, Controlled syntheses of Agpolytetrafluoroethylene nanocomposite thin films by co-sputtering from two magnetron sources, Nanotechnology 16 (2005) 1078.

[19] L. Rosenthal, H. Greve, V. Zaporojtchenko, T. Strunskus, F. Faupel, M. Bonitz, Formation of magnetic nanocolumns during vapor phase deposition of a metal-polymer nanocomposite: Experiments and kinetic Monte Carlo simulations, Journal of Applied Physics 114 (4) (2013) 044305.

[20] A. Biswas, Z. Marton, J. Kanzow, J. Kruse, V. Zaporojtchenko, T. Strunskus, M. Czank, F. Faupel, Nanocomposites of Vapour Phase Deposited Teflon AF Containing Ni Clusters, Solid State Phenomena 94 (2003) 285–294.

[21] T. Koloski, T. Vargo, Polymer and inorganic-organic hybrid composites and methods for making same (1999).

[22] K. C. See, J. B. Spicer, J. Brupbacher, D. Zhang, T. G. Vargo, Modeling Interband Transitions in Silver Nanoparticle-Fluoropolymer Composites, J. Phys. Chem. B 2005, 109 (2005) 2693.

[23] J. A. Horas, M. G. Rizzotto, Gas diffusion in partially crystalline polymers part I: Concentration dependence, Journal of Polymer Science Part B: Polymer Physics 34 (9) (1996) 1541–1546.

[24] W. Vieth, W. F. Wuerth, Transport properties and their correlation with the morphology of thermally conditioned polypropylene, Journal of Applied Polymer Science 13 (4) (1969) 685–712.

[25] M. Galizia, C. Daniel, G. Fasano, G. Guerra, G. Mensitieri, Gas Sorption and Diffusion in Amorphous and Semicrystalline Nanoporous Poly(2,6-dimethyl-1,4-phenylene)oxide, Macromolecules 45 (8) (2012) 3604.

[26] L. Masaro, X. X. Zhu, Physical models of diffusion for polymer solutions, gels and solids, Progress in Polymer Science 24 (5) (1999) 731.

[27] C. Nagel, K. Gu, D. Fritsch, T. Strunskus, F. Faupel, Free Volume and Transport Properties in Highly Selective Polymer Membranes, Macromolecules 35 (6) (2002) 2071.

[28] A. K. Doolittle, Studies in Newtonian Flow. II. The Dependence of the Viscosity of Liquids on Free-Space, Journal of Applied Physics 22 (12) (1951) 1471.

[29] T. G. Fox, P. J. Flory, Second-Order Transition Temperatures and Related Properties of Polystyrene. I. Influence of Molecular Weight, Journal of Applied Physics 21 (6) (1950) 581.

[30] T. G. Fox, P. J. Flory, Further Studies on the Melt Viscosity of Polyisobutylene., The Journal of Physical Chemistry 55 (2) (1951) 221–234.

[31] M. Karimi, Diffusion in Polymer Solids and Solutions, in: Mass Transfer in Chemical Engineering Processes, InTech, 2011, p. 17.

[32] A. Alentiev, Y. Yampolskii, V. Shantarovich, S. Nemser, N. Plate, High tranSport parameters and free volume of peruorodioxole copolymers, Journal of Membrane Science 126 (1997) 123.

[33] P. N. Patil, D. Roilo, R. S. Brusa, A. Miotello, S. Aghion, R. Ferragut, R. Checchetto, Free volumes and gas transport in polymers: amine-modified epoxy resins as a case study, Phys. Chem. Chem. Phys. Phys. Chem. Chem. Phys 18 (18) (2016) 3817–3824.

[34] P. Huo, P. Cebe, Dielectric relaxation of poly(phenylene sulfide) containing a fraction of rigid amorphous phase, Journal of Polymer Science Part B: Polymer Physics 30 (3) (1992) 239–250.

[35] P. Huo, P. Cebe, Temperature-dependent relaxation of the crystal-amorphous interphase in poly(ether ether ketone), Macromolecules 25 (2) (1992) 902–909.

[36] G. Calleja, A. Jourdan, B. Ameduri, J.-P. Habas, Where is the glass transition temperature of poly(tetrafluoroethylene)? A new approach by dynamic rheometry and mechanical tests, European Polymer Journal 49 (8) (2013) 2214–2222.

[37] J. Lin, S. Shenogin, S. Nazarenko, Oxygen solubility and specific volume of rigid amorphous fraction in semicrystalline poly(ethylene terephthalate), Polymer 43 (17) (2002) 4733–4743.

[38] B. G. Olson, J. Lin, S. Nazarenko, A. M. Jamieson, Positron Annihilation Lifetime Spectroscopy of Poly(ethylene terephthalate): Contributions from Rigid and Mobile Amorphous Fractions, Macromolecules 36 (20) (2003) 7618.

[39] V. Cominos, a. Gavriilidis, Sublimation and deposition behaviour of palladium (II) acetylacetonate, The European Physical Journal Applied Physics 15 (01) (2001) 23–33.

[40] B. Janković, S. Mentus, Model-fitting and model-free analysis of thermal decom-

position of palladium acetylacetonate [Pd(acac)2], Journal of Thermal Analysis and Calorimetry 94 (2) (2008) 395–403.

[41] G. S. Y Yeh, R. Hosemann, J. Loboda-C, Annealing effects of polymers and their underlying molecular mechanisms, Polymer 17 (4) (1976) 309.

[42] E. W. Fischer, Effect of Annealing and Temperature on the Morphological Structure of Polymers, Pure and Applied Chemistry 31 (1) (1972) 1365.

[43] T. Nyuui, A. Fujimori, Effect of Fixed Annealing and free shrinkage to the crystalline fluorinated copolymer film with high transparency, Transactions of the Materials Research Society of Japan 36 (2) (2011) 137.

[44] Y. Srithep, P. Nealey, L.-S. Turng, Effects of annealing time and temperature on the crystallinity and heat resistance behavior of injection-molded poly(lactic acid), Polymer Engineering & Science 53 (3) (2013) 580–588.

[45] R. L. Blaine, Determination of Polymer Crystallinity by DSC, TA Instrument Publication: New Castel, DE, 2010.

[46] A. Teverovsky, A Rapid Technique for Moisture Diffusion Characterization of Molding Compounds in PEMs, Tech. rep., QSS Group, Inc./Goddard Operations (2002).

[47] E. L. Cussler, Fundamentals of Mass Transfer, in: Diffusion, Cambridge University Press, Cambridge, 2009, pp. 237–273.

[48] S. Lee, K. S. Knaebel, Effects of mechanical and chemical properties on transport in fluoropolymers. I. Transient sorption, Journal of Applied Polymer Science 64 (3) (1997) 455–476.

[49] T. M. Aminabhavi, R. S. Munnolli, W. M. Stahl, S. V. Gangal, Sorption and diffusion of organic esters into fluoropolymer membranes, Journal of Applied Polymer Science 48 (5) (1993) 857–865.

[50] T. R. Dargaville, G. A. George, D. J. T. Hill, A. K. Whittaker, An Investigation of the Thermal and Tensile Properties of PFA Following γ-Radiolysis, Macromolecules 36 (19) (2003) 7132.

[51] F. Cardona, D. Hill, G. George, J. Maeji, R. Firas, S. Perera, Thermal characterization of copolymers obtained by radiation grafting of styrene onto poly(tetrafluoroethylene-perfluoropropylvinylether) substrates: thermal decomposition, melting behavior and low-temperature transitions, Polymer Degradation and Stability 74 (2) (2001) 219–227.

[52] A. Fujimori, M. Hasegawa, T. Masuko, Spherulitic structures of poly [tetrafluoroethylene-co-(perfluoroalkyl vinyl ether)], Polymer International 56 (10) (2007) 1281–1287.

[53] M. Endo, A. Ohnishi, S. Kutsumizu, T. Shimizu, S. Yano, Crystallization in Binary Blends of Polytetrafluoroethylene with Perfluorinated Tetrafluoroethylene Copolymer, Polymer Journal 36 (2004) 716.

[54] S. Thomas, D. Ponnamma, A. Zachariah, Polymer Processing and Characterization, Technology & Engineering, 2012.

[55] J. Bitter, Effect of crystallinity and swelling on the permeability and selectivity of polymer membranes, Desalination 51 (1) (1984) 19–35.

[56] S. W. Lasoski, W. H. Cobbs, Moisture permeability of polymers. I. Role of crystallinity and orientation, Journal of Polymer Science 36 (130) (1959) 21–33.

[57] V. Mittal, Crystallinity, mechanical property and oxygen permeability of polypropylene: Effect of processing conditions, nucleating agent and compatibilizer, Journal of Thermoplastic Composite Materials 26 (10) (2013) 1407–1423.

[58] G. Matsuba, T. Nyuui, S. Sato, K. Nagai, Estimation of Crystalline Structure and Gas Transport Properties of Crystalline Fluorinated Copolymer, Meeting Abstracts MA2015-01 (40) (2015) 2109.

[59] D. Turnbullmorrel, H. Cohen, D. Turnbull, M. H. Cohen, Free-Volume Model of the Amorphous Phase: Glass Transition, The Journal of Chemical Physics 34 (1).

[60] H. Fujita, Diffusion in polymer-diluent systems, in: Fortschritte Der Hochpolymeren-Forschung, Springer-Verlag, Berlin/Heidelberg, 1961, pp. 1–47.

[61] K.-i. Okamoto, K. Tanaka, M. Katsube, H. Kita, O. Sueoka, Y. Ito, Correlation

between Positron Annihilation and Gas Diffusion Properties of Various Rubbery Polymers, Polymer Journal 25 (3) (1993) 275–284.

[62] G. Dlubek, A. Sen Gupta, J. Pionteck, R. Häßler, R. Krause-Rehberg, H. Kaspar, K. H. Lochhaas, Glass transition and free volume in the mobile (MAF) and rigid (RAF) amorphous fractions of semicrystalline PTFE: a positron lifetime and PVT study, Polymer 46 (16) (2005) 6075.

[63] G. Dlubek, M. A. Alam, K. Saarinen, J. Stejny, H. M. Fretwell, Relations between Hole Volume and Macroscopic Volume in Various Polymers, ACTA PHYSICA POLONICA A 95 (1999) 521.

[64] R. Srithawatpong, Z. L. Peng, B. G. Olson, A. M. Jamieson, R. Simha, J. D. Mcgervey, T. R. Maier, A. F. Halasa, H. Ishida, Positron Annihilation Lifetime Studies of Changes in Free Volume on Cross - Linking Cis - Polyisoprene , High - Vinyl Polybutadiene , and their Miscible Blends, J Polym Sci B : Polym Phys 37 (1999) 2754–2770.

[65] R. Simha, P. S. Wilson, Thermal Expansion of Amorphous Polymers at Atmospheric Pressure. II. Theoretical Considerations, Macromolecules 6 (6) (1973) 908–914.

[66] M.-L. Cheng, Y.-M. Sun, Effect of thermal history on the free volume properties of semi-crystalline poly(3-hydroxybutyrate- co -3-hydroxyvalerate) membranes

by positron annihilation lifetime spectroscopy, Journal of Polymer Science Part B: Polymer Physics 47 (9) (2009) 855–865.

[67] G. Nter Dlubek, J. Rgen Pionteck, K. Rätzke, J. Kruse, F. Faupel, Temperature Dependence of the Free Volume in Amorphous Teflon AF1600 and AF2400: A Pressure-Volume-Temperature and Positron Lifetime Study, Macromolecules 41 (16) (2008) 6125.

[68] A. R. Siedle, T. J. Kistenmacher, R. M. Metzger, C.-S. Kuo, R. P. Van Duyne, T. Cape, (Tetrathiafulvalene)bis(acetylacetonato)palladium(II), (TTF)Pd(acac)2, a metallotetrathiaethylene containing neutral tetrathiafulvalene, Inorganic Chemistry 19 (7) (1980) 2048–2051.

[69] J. Liu, Q. Deng, Y. C. Jean, Free-volume distributions of polystyrene probed by positron annihilation: comparison with free-volume theories, Macromolecules 26 (26) (1993) 7149–7155.

[70] R. A. L. Vallée, N. Tomczak, L. Kuipers, G. J. Vancso, N. F. van Hulst, Single Molecule Lifetime Fluctuations Reveal Segmental Dynamics in Polymers, Physical Review Letters 91 (3) (2003) 038301.

[71] R. A. L. Vallée, M. Cotlet, M. Van Der Auweraer, J. Hofkens, K. Müllen, F. C. De Schryver, Single-Molecule Conformations Probe Free Volume in Polymers, Journal of the American Chemical Society 126 (8) (2004) 2296–2297.

[72] R. E. Robertson, Free-Volume Theory and Its Application to Polymer Relaxation in the Glassy State, in: J. Bicerano (Ed.), Computational Modeling of Polymers, Marcel Dekker, Midland, MI, 1992, Ch. 6, p. 297.

[73] R. E. Robertson, Effect of free-volume fluctuations on polymer relaxation in the glassy state, Journal of Polymer Science: Polymer Symposia 63 (1) (2007) 173–183.

[74] K. Nakamura, T. Kawabata, Y. Mori, Size distribution analysis of colloidal gold by small angle X-ray scattering and light absorbance, Powder Technology 131 (2) (2003) 120–128.

[75] R. Bienert, F. Emmerling, A. F. Thünemann, The size distribution of 'gold standard' nanoparticles, Analytical and Bioanalytical Chemistry 395 (6) (2009) 1651–1660.

[76] T. J. Dejournett, J. B. Spicer, Photoinduced Silver Precursor Decomposition for Particle Modification in Tungsten Oxide Polymer Matrix Nanocomposites, J. Phys. Chem. C 118 (18) (2014) 9820.

[77] T. J. Woehl, J. E. Evans, I. Arslan, W. D. Ristenpart, N. D. Browning, Direct in Situ Determination of the Mechanisms Controlling Nanoparticle Nucleation and Growth, ACS Nano 6 (10) (2012) 8599–8610.

[78] B. L. Caetano, C. V. Santilli, F. Meneau, V. Briois, S. H. Pulcinelli, In Situ

and Simultaneous UVvis/SAXS and UVvis/XAFS Time-Resolved Monitoring of ZnO Quantum Dots Formation and Growth, The Journal of Physical Chemistry C 115 (11) (2011) 4404–4412.

[79] J. Polte, R. Erler, A. F. Thunemann, S. Sokolov, T. T. Ahner, K. Rademann, F. Emmerling, R. Kraehnert, Nucleation and Growth of Gold Nanoparticles Studied via in situ Small Angle X-ray Scattering at Millisecond Time Resolution, ACS Nano 4 (2) (2010) 1076–1082.

[80] V. K. LaMer, R. H. Dinegar, Theory, Production and Mechanism of Formation of Monodispersed Hydrosols, Journal of the American Chemical Society 72 (11) (1950) 4847–4854.

[81] V. K. LaMer, Nucleation in Phase Transitions., Industrial & Engineering Chemistry 44 (6) (1952) 1270–1277.

[82] W. Ostwald, Ostwald ripening theory, Chemical physics 34 (1900) 495.

[83] I. Lifshitz, V. Slyozov, The kinetics of precipitation from supersaturated solid solutions, Journal of Physics and Chemistry of Solids 19 (1) (1961) 35–50.

[84] C. Z. Wagner, Theory of precipitate change by redissolution, Angew. Phys. Chem. 65 (1961) 581–591.

[85] H. Zheng, R. K. Smith, Y.-w. Jun, C. Kisielowski, U. Dahmen, A. P. Alivisatos,

Observation of Single Colloidal Platinum Nanocrystal Growth Trajectories, Science 324 (5932) (2009) 1309.

[86] R. L. Penn, J. F. Banfield, Morphology development and crystal growth in nanocrystalline aggregates under hydrothermal conditions: Insights from titania, Geochim. Cosmochim. Acta 63 (1999) 1549.

[87] X. Peng, L. Manna, W. Yang, J. Wickham, E. Scher, A. Kadavanich, A. P. Alivisatos, Shape control of CdSe nanocrystals, Nature 404 (2000) 59.

[88] M. José-Yacamán, C. Gutierrez-Wing, M. Miki, . D.-Q. Yang, . K. N. Piyakis, E. Sacher, Surface Diffusion and Coalescence of Mobile Metal Nanoparticles, J. Phys. Chem. B 109 (2005) 9703.

[89] M. A. Watzky, R. G. Finke, Nanocluster Size-Control and "Magic Number" Investigations. Experimental Tests of the " Living-Metal Polymer " Concept and of Mechanism-Based Size-Control Predictions Leading to the Syntheses of Iridium(0) Nanoclusters Centering abou, Chem. Mater. 9 (1997) 3083.

[90] C. Besson, E. E. Finney, R. G. Finke, A Mechanism for Transition-Metal Nanoparticle Self-Assembly, Journal of American Chemical Society 127 (2005) 8179.

[91] M. A. Watzky, E. E. Finney, R. G. Finke, Transition-Metal Nanocluster Size vs Formation Time and the Catalytically Effective Nucleus Number:

A Mechanism-Based Treatment, Journal of the American Chemical Society 130 (36) (2008) 11959–11969.

[92] S. Yao, Y. Yuan, C. Xiao, W. Li, Y. Kou, P. J. Dyson, N. Yan, H. Asakura, K. Teramura, T. Tanaka, Insights into the Formation Mechanism of Rhodium Nanocubes, The Journal of Physical Chemistry C 116 (28) (2012) 15076–15086.

[93] D. Walton, Nucleation of Vapor Deposits, The Journal of Chemical Physics 37 (10) (1962) 2182–2188.

[94] A. Milchev, Nucleation phenomena in electrochemical systems: kinetic models, ChemTexts 2 (2016) 4.

[95] J. Robins, T. Rhodin, Nucleation of metal crystals on ionic surfaces, Surface Science 2 (1964) 346–355.

[96] J. Hamilton, P. Logel, Nucleation and growth of Ag and Pd on amorphous carbon by vapor deposition, Thin Solid Films 16 (1) (1973) 49–63.

[97] V. Robinson, J. Robins, Nucleation kinetics of gold deposited onto UHV cleaved surfaces of NaCl and KBr, Thin Solid Films 20 (1) (1974) 155–175.

[98] J. A. Venables, G. D. T. Spiller, M. Hanbucken, Nucleation and growth of thin films, Rep. Prog. Phys. 47 (1984) 399–459.

[99] M. Zinke-Allmang, L. C. Feldman, M. H. Grabow, Clustering on surfaces, Surface Science Reports 16 (8) (1992) 377–463.

[100] F. Spaepen, A microscopic mechanism for steady state inhomogeneous flow in metallic glasses, Acta Metallurgica 25 (4) (1977) 407–415.

[101] H. A. Sturges, THE CHOICE OF A CLASS INTERVAL CASE I. COMPUTATIONS INVOLVING A SINGLE SERIES, Journal of American Statistical Association 21 (1926) 65.

[102] A. Baldan, Review Progress in Ostwald ripening theories and their applications to nickel-base superalloys Part I: Ostwald ripening theories, Journal of Materials Science 37 (11) (2002) 2171–2202.

[103] F. W. Zeng, D. Zhang, J. B. Spicer, Effect of Polymer Structure on Precursor Diffusion and Particle Formation in Polymer Matrix Nanocomposites, Journal of Inorganic and Organometallic Polymers and Materials 28 (5) (2018) 1850.

[104] C. R. Henry, Growth, Structure and Morphology of Supported Metal Clusters Studied by Surface Science Techniques, Crystal Research and Technology 33 (7-8) (1998) 1119–1140.

[105] K. Routledge, M. Stowell, Nucleation kinetics in thin film growth. I. Computer simulation of nucleation and growth behaviour, Thin Solid Films 6 (6) (1970) 407–421.

[106] M. J. Stowell, Capture numbers in thin film nucleation theories, Philosophical Magazine 26 (2) (1972) 349–360.

[107] C. R. Henry, M. Meunier, Power laws in the growth kinetics of metal clusters on oxide surfaces, Vacuum 50 (1-2) (1998) 157–163.

[108] J. B. Spicer, Y. Dikmelik, Elastic wavefield interactions with solute species during precipitation processes in solids, Acta Materialia 57 (5) (2009) 1459–1465.

[109] D. Turnbull, Phase Changes, in: Solid State Physics: Advances in Research and Applications, Academic Press, New York, 1956, Ch. 3, p. 226.

[110] F. Wang, V. N. Richards, S. P. Shields, W. E. Buhro, Kinetics and Mechanisms of Aggregative Nanocrystal Growth, Chemistry of Materials 26 (2014) 5.

[111] E. E. Finney, R. G. Finke, Is There a Minimal Chemical Mechanism Underlying Classical Avrami-Erofe'ev Treatments of Phase-Transformation Kinetic Data?, Chem. Mater 21 (2009) 4692–4705.

[112] S. P. Shields, V. N. Richards, W. E. Buhro, Nucleation Control of Size and Dispersity in Aggregative Nanoparticle Growth. A Study of the Coarsening Kinetics of Thiolate-Capped Gold Nanocrystals, Chem. Mater 22 (2010) 3212–3225.

[113] H. Sawada, Fluoropolymer Nanocomposites, in: Handbook of Fluoropolymer Science and Technology, John Wiley & Sons, Inc., Hoboken, NJ, USA, 2014, pp. 57–79.

[114] R. I. Jaffee (Ed.), Refractory Metals and Alloys IV: Research and Development - Google Books, Science, 1967.

[115] M. Attarian Shandiz, A. Safaei, S. Sanjabi, Z. Barber, Modeling size dependence of melting temperature of metallic nanoparticles, Journal of Physics and Chemistry of Solids 68 (7) (2007) 1396–1399.

[116] P. Puri, V. Yang, Effect of Particle Size on Melting of Aluminum at Nano Scales, J. Phys. Chem. C 111 (2007) 11776.

[117] B. Chen, G. H. Ten Brink, G. Palasantzas, B. J. Kooi, Size-dependent and tunable crystallization of GeSbTe phase- change nanoparticles, Scientific Reports 6 (2016) 39546.

[118] W. Lu, B. Wang, K. Wang, X. Wang, J. G. Hou, Synthesis and Characterization of Crystalline and Amorphous Palladium Nanoparticles, Langmuir 19 (2003) 5887.

[119] F. Grillo, H. V. Bui, J. A. Moulijn, M. T. Kreutzer, J. Ruud Van Ommen, Understanding and Controlling the Aggregative Growth of Platinum Nanoparticles in Atomic Layer Deposition: An Avenue to Size Selection, Journal of Physical Chemistry Letters 8 (2017) 975.

[120] Y. Min, M. Akbulut, K. Kristiansen, Y. Golan, J. Israelachvili, The role of

interparticle and external forces in nanoparticle assembly, Nature Materials 7 (7) (2008) 527–538.

[121] J. Spicer, K. See, Y. Katsumi, D. Zhang, J. Brupbacher, T. Vargo, Linear and Nonlinear Optical Properties of Palladium Nanoparticle Reinforced Fluoropolymer Composites, in: NSTI-Nanotech 2006, Vol. 1, 2006, pp. 789–792.

[122] Y. Jean, J. Zhang, H. Chen, Y. Li, G. Liu, Positron annihilation spectroscopy for surface and interface studies in nanoscale polymeric films, Spectrochimica Acta Part A: Molecular and Biomolecular Spectroscopy 61 (7) (2005) 1683–1691.

[123] V. N. Bagratashvili, A. O. Rybaltovsky, N. V. Minaev, P. S. Timashev, V. V. Firsov, V. I. Yusupov, Laser-induced atomic assembling of periodic layered nanostructures of silver nanoparticles in fluoro-polymer film matrix, Laser Physics Letters 7 (5) (2010) 401–404.

[124] K. Setoura, Y. Okada, S. Hashimoto, CW-laser-induced morphological changes of a single gold nanoparticle on glass: observation of surface evaporation, Phys. Chem. Chem. Phys. 16 (16) (2693) 26938–26945.

[125] F. Hubenthal, M. Alschinger, M. Bauer, D. Blazquez Sanchez, N. Borg, M. Brezeanu, R. Frese, C. Hendrich, B. Krohn, M. Aeschliman, F. Trager, Irradiation of supported gold and silver nanoparticles with continuous-wave, nanosecond, and femtosecond laser light: a comparative study, in: P. Lugli,

L. B. Kish, J. Mateos (Eds.), Proc. SPIE 5838, Nanotechnology II, 2005, p. 224.

[126] G. Baffou, H. Rigneault, Femtosecond-pulsed optical heating of gold nanoparticles, PHYSICAL REVIEW B 84.

[127] P. Keblinski, D. G. Cahill, A. Bodapati, C. R. Sullivan, T. A. Taton, Monitoring iron oxide nanoparticle surface temperature in an alternating magnetic field using thermoresponsive fluorescent polymers, Citation: Journal of Applied Physics 100 (2006) 7–334.

[128] T. Teranishi, M. Eguchi, M. Kanehara, S. Gwo, Controlled localized surface plasmon resonance wavelength for conductive nanoparticles over the ultraviolet to near-infrared region, J. Mater. Chem. 21 (2011) 10238.

[129] L. Urech, T. Lippert, Photoablation of Polymer Materials, in: Photochemistry and Photophysics of Polymer Materials, John Wiley & Sons, Inc., Hoboken, NJ, USA, 2010, pp. 541–568.

[130] K. Lee, S. Jockusch, N. J. Turro, R. H. French, R. C. Wheland, M. F. Lemon, A. M. Braun, T. Widerschpan, P. Zimmerman, 157-nm pellicles for photolithography: mechanistic investigation of the deep-UV photolysis of fluorocarbons, in: B. W. Smith (Ed.), Proceedings of SPIE, Vol. 5377, 2004, p. 1598.

[131] V. N. Vasilets, I. Hirata, H. Iwata, Y. Ikada, Photolysis of a fluorinated poly-

mer film by vacuum ultraviolet radiation, Journal of Polymer Science Part A: Polymer Chemistry 36 (13) (1998) 2215–2222.

[132] J. Scheirs, J.-L. Gardette, Photo-oxidation and photolysis of poly(ethylene naphthalate), Polymer Degradation and Stability 56 (3) (1997) 339–350.

[133] C. F. Bohren, D. R. Huffman, Absorption and scattering of light by small particles, Wiley, 1998.

[134] V. Myroshnychenko, J. Rodruez-Fernadez, I. Pastoriza-Santos, A. M. Funston, C. Novo, P. Mulvaney, L. M. Liz-Marza, F. Javier Garcá De Abajo, Modelling the optical response of gold nanoparticlesw, Chem. Soc. Rev. 37 (2008) 1792.

[135] M. Hlaing, B. Gebear-Eigzabher, A. Roa, A. Marcano, D. Radu, C.-Y. Lai, Absorption and scattering cross-section extinction values of silver nanoparticles, Optical Materials 58 (2016) 439–444.

[136] F. W. Zeng, D. Zhang, J. B. Spicer, Palladium Nanoparticle Formation Processes in Fluoropolymers by Thermal Decomposition of Organometallic Precursors, Physical Chemistry Chemical Physics 20 (2018) 24389.

[137] Qiang Liu, Zhi-Min Cui, Zhuo Ma, , Shao-Wei Bian, W.-G. Song*, Highly Active and Stable Material for Catalytic Hydrodechlorination Using Ammonia-Treated Carbon Nanofibers as Pd Supports, Journal Of Physical Chemistry C 112 (4) (2008) 1199.

[138] Y. Bi, G. Lu, Catalytic CO oxidation over palladium supported NaZSM-5 catalysts, Applied Catalysis B: Environmental 41 (3) (2003) 279–286.

[139] A. Molnar, Efficient, Selective, and Recyclable Palladium Catalysts in Carbon-Carbon Coupling Reactions, Chemical Reviews 111 (3) (2011) 2251–2320.

[140] J. Magano, J. R. Dunetz, Large-Scale Applications of Transition Metal-Catalyzed Couplings for the Synthesis of Pharmaceuticals, Chemical Reviews 111 (3) (2011) 2177–2250.

[141] K. C. Nicolaou, P. G. Bulger, D. Sarlah, Palladium-Catalyzed Cross-Coupling Reactions in Total Synthesis, Angewandte Chemie International Edition 44 (29) (2005) 4442–4489.

[142] A. Klinkova, A. Ahmed, R. M. Choueiri, J. R. Guest, E. Kumacheva, Toward rational design of palladium nanoparticles with plasmonically enhanced catalytic performance, RSC Advances 6 (2016) 47907.

[143] Q. Xiao, S. Sarina, A. Bo, J. Jia, H. Liu, D. P. Arnold, Y. Huang, H. Wu, H. Zhu, Visible Light-Driven Cross-Coupling Reactions at Lower Temperatures Using a Photocatalyst of Palladium and Gold Alloy Nanoparticles, ACS Catalysis 4 (2014) 1725.

[144] W. H. Lee, J. W. Suk, H. Chou, J. Lee, Y. Hao, Y. Wu, R. Piner, D. Akin-

wande, K. S. Kim, R. S. Ruoff, Selective-Area Fluorination of Graphene with Fluoropolymer and Laser Irradiation, Nano Letters 12 (2012) 2374.

[145] D. Fragouli, V. Resta, P. P. Pompa, A. M. Laera, G. Caputo, L. Tapfer, R. Cingolani, A. Athanassiou, Patterned structures of in situ size controlled CdS nanocrystals in a polymer matrix under UV irradiation, Nanotechnology 29 (2009) 155302.

[146] M. Watanabe, H. Takamura, H. Sugai, Preparation of Ultrafine Fe-Pt Alloy and Au Nanoparticle Colloids by KrF Excimer Laser Solution Photolysis., Nanoscale research letters 4 (6) (2009) 565–573.

[147] K. Vora, S. Kang, S. Shukla, E. Mazur, Fabrication of disconnected threedimensional silver nanostructures in a polymer matrix, Applied Physics Letters 100 (6) (2012) 063120.

[148] A. Chahadih, H. El Hamzaoui, R. Bernard, L. Boussekey, L. Bois, O. Cristini, M. Le Parquier, B. Capoen, M. Bouazaoui, Direct-writing of PbS nanoparticles inside transparent porous silica monoliths using pulsed femtosecond laser irradiation., Nanoscale research letters 6 (1) (2011) 542.

[149] F. Zaera, Tungsten Hexacarbonyl Thermal Decomposltlon on Nl(100) Surfaces, J. Phys. Chem 96 (1992) 4609–4615.

[150] K. Gesheva, T. Ivanova, G. Bodurov, APCVD Transition Metal Oxides - Func-

tional Layers in Smart windows , Journal of Physics: Conference Series 559 (2014) 012002.

[151] M. Sun, N. Xu, Y. W. Cao, J. N. Yao, E. G. Wang, Nanocrystalline tungsten oxide thin film: Preparation, microstructure, and photochromic behavior, J. Mater. Res. 15 (2000) 927.

[152] J. Tauc, R. Grigorovici, A. Vancu, Optical Properties and Electronic Structure of Amorphous Germanium, physica status solidi (b) 15 (2) (1966) 627–637.

[153] C. Di Valentin, F. Wang, G. Pacchioni, Tungsten Oxide in Catalysis and Photocatalysis: Hints from DFT, Topics in Catalysis 56 (15-17) (2013) 1404–1419.

[154] C. Janáky, K. Rajeshwar, N. de Tacconi, W. Chanmanee, M. Huda, Tungsten-based oxide semiconductors for solar hydrogen generation, Catalysis Today 199 (2013) 53–64.

[155] X. Gao, X. Su, C. Yang, F. Xiao, J. Wang, X. Cao, S. Wang, L. Zhang, Hydrothermal synthesis of WO3 nanoplates as highly sensitive cyclohexene sensor and high-efficiency MB photocatalyst, Sensors and Actuators B: Chemical 181 (2013) 537–543.

[156] P. Grua, J. P. Morreeuw, H. Bercegol, G. Jonusauskas, F. Vallée, Electron kinetics and emission for metal nanoparticles exposed to intense laser pulses, Physical Review B 68 (3) (2003) 035424.

[157] V. Pustovalov, A. Smetannikov, V. Zharov, Photothermal and accompanied phenomena of selective nanophotothermolysis with gold nanoparticles and laser pulses, Laser Physics Letters 5 (11) (2008) 775–792.

[158] H. Inouye, K. Tanaka, I. Tanahashi, K. Hirao, Ultrafast dynamics of nonequilibrium electrons in a gold nanoparticle system, Physical Review B 57 (18) (1998) 11334–11340.

[159] J. Olson, S. Dominguez-Medina, A. Hoggard, L.-Y. Wang, W.-S. Chang, S. Link, Optical characterization of single plasmonic nanoparticles., Chemical Society reviews 44 (1) (2015) 40–57.

[160] Y. Li, L. Song, Y. Qiao, Experimental and theoretical realization of enhanced light scattering spectroscopy of gold nanorods, Applied Physics Letters 106 (2) (2015) 021907.

[161] W. Albrecht, T.-S. Deng, B. Goris, M. A. van Huis, S. Bals, A. van Blaaderen, Single Particle Deformation and Analysis of Silica-Coated Gold Nanorods before and after Femtosecond Laser Pulse Excitation., Nano letters 16 (3) (2016) 1818–25.

[162] S. L. And, M. A. El-Sayed*, Spectral Properties and Relaxation Dynamics of Surface Plasmon Electronic Oscillations in Gold and Silver Nanodots and Nanorods, Journal of Physical Chemistry B 103 (1999) 8410.

[163] F. Ghasempour, R. Azimirad, A. Amini, O. Akhavan, Visible light photoinactivation of bacteria by tungsten oxide nanostructures formed on a tungsten foil, Applied Surface Science 338 (2015) 55–60.

[164] Z. Wen, W. Wu, Z. Liu, H. Zhang, J. Li, J. Chen, Ultrahigh-efficiency photocatalysts based on mesoporous PtWO3 nanohybrids, Physical Chemistry Chemical Physics 15 (18) (2013) 6773.

[165] S. K. Deb, Optical and photoelectric properties and colour centres in thin films of tungsten oxide, Philosophical Magazine 27 (4) (1973) 801–822.

[166] R. Vemuri, M. Engelhard, C. Ramana, Correlation between Surface Chemistry, Density, and Band Gap in Nanocrystalline WO3 Thin Films, ACS Applied Materials & Interfaces 4 (3) (2012) 1371–1377.

[167] J. Zhu, M. Vasilopoulou, D. Davazoglou, S. Kennou, A. Chroneos, U. Schwingenschlögl, Intrinsic Defects and H Doping in WO3, Scientific Reports 7 (1) (2017) 40882.

[168] K. Yumashev, A. Malyarevich, N. Posnov, I. Denisov, V. Mikhailov, M. Artemyev, D. Sviridov, Optical transient bleaching of photochromic polytungstic acid, Chemical Physics Letters 288 (2-4) (1998) 567–575.

[169] K. V. Yumashev, A. M. Malyarevich, N. N. Posnov, I. A. Denisov, M. V. Artem'ev, D. V. Sviridov, V. P. Mikhailov, Nonlinear spectroscopy of photo-

coloured polytungstic acid nanocomposites, Quantum Electronics 28 (8) (1998) 710–714.

[170] M. E. Lines, Influence of d orbitals on the nonlinear optical response of transparent transition-metal oxides, Physical Review B 43 (14) (1991) 11978–11990.

[171] C. Xu, W. W. Webb, Measurement of two-photon excitation cross sections of molecular fluorophores with data from 690 to 1050 nm, J. Opt. Soc. Am. B 13 (3).

[172] J. Allpress, R. Tilley, M. Sienko, Examination of substoichiometric WO3x crystals by electron microscopy, Journal of Solid State Chemistry 3 (3) (1971) 440–451.

[173] J. M. Berak, M. Sienko, Effect of oxygen-deficiency on electrical transport properties of tungsten trioxide crystals, Journal of Solid State Chemistry 2 (1) (1970) 109–133.

[174] B. Dasgupta, Y. Ren, L. M. Wong, L. Kong, E. S. Tok, W. K. Chim, S. Y. Chiam, Detrimental Effects of Oxygen Vacancies in Electrochromic Molybdenum Oxide, The Journal of Physical Chemistry C 119 (19) (2015) 10592–10601.

[175] H. Chen, N. Xu, S. Deng, D. Lu, Z. Li, J. Zhou, J. Chen, Gasochromic effect and relative mechanism of WO3 nanowire films, Nanotechnology 18 (2007) 205701.

[176] B. W. Faughnan, R. S. Crandall, M. A. Lampert, Model for the bleaching of

WO3 electrochromic films by an electric field, Applied Physics Letters 27 (5) (1975) 275–277.

[177] C. G. Granqvist, Electrochromic tungsten oxide films: Review of progress 1993-1998, Solar Energy Materials & Solar Cells 60 (2000) 201.

[178] A. Georg, W. Graf, R. Neumann, V. Wittwer, Mechanism of the gasochromic coloration of porous WO3 films, Solid State Ionics 127 (3-4) (2000) 319–328.

[179] C. Castañeda, F. Tzompantzi, A. Rodríguez-Rodríguez, M. Sánchez-Dominguez, R. Gómez, Improved photocatalytic hydrogen production from methanol/water solution using CuO supported on fluorinated TiO2, J Chem Technol Biotechnol 93 (2018) 1113.

[180] D. Chen, X. Hou, H. Wen, Y. Wang, H. Wang, X. Li, R. Zhang, H. Lu, H. Xu, S. Guan, J. Sun, L. Gao, The enhanced alcohol-sensing response of ultrathin WO3 nanoplates, Nanotechnology 21 (3) (2010) 035501.

[181] W. J. Koros, J. Wang, R. M. Felder, Oxygen permeation through FEP Teflon and Kapton polyimide, Journal of Applied Polymer Science 26 (8) (1981) 2805–2809.

[182] M. V. Limaye, J. S. Chen, S. B. Singh, Y. C. Shao, Y. F. Wang, C. W. Pao, H. M. Tsai, J. F. Lee, H. J. Lin, J. W. Chiou, M. C. Yang, W. T. Wu, J. J. Wu,

M. H. Tsai, W. F. Pong, Correlation between electrochromism and electronic structures of tungsten oxide films, RSC Advances 4 (2014) 5036.

[183] B. Hammer, J. K. Norskov, Why gold is the noblest of all the metals, Nature 376 (1995) 238.

[184] . Sheng-Yang Huang, . Chin-Da Huang, , . Boh-Tze Chang, . Chuin-Tih Yeh*, Chemical Activity of Palladium Clusters: Sorption of Hydrogen, The Journal of Physical Chemistry B 110 (2006) 21783.

[185] M. Pozzo, D. Alfè, Hydrogen dissociation and diffusion on transition metal (=Ti, Zr, V, Fe, Ru, Co, Rh, Ni, Pd, Cu, Ag)-doped Mg(0001) surfaces, International Journal of Hydrogen Energy 34 (4) (2009) 1922–1930.

[186] H. Zhang, A. Cloud, The Permeability Characteristics of Silicone Rubber, in: 2006 SAMPE Fall Technical Conference: Global Advances in Materials and Process Engineering, Society for the Advancement of Material and Process Engineering, Dallas, 2006.

Curriculum Vitae

Fan W. Zeng

267-616-6447 fanwzeng@jhu.edu

Education

Johns Hopkins University Baltimore, MD

Ph.D., Materials Science and Engineering 2018

Johns Hopkins University Baltimore, MD

MSc, Materials Science and Engineering, JHU Gordon Croft Fellow 2013 – 2015

Emory & Henry College Emory, VA

BSc, Physics, Chemistry (with honors), and Mathematics 2007 – 2011

Research & Work Experience

Advanced Thermal Battery Inc. (APL) Westminister, MD

Research Specialist July 2018 – Present

- Research and develop high voltage thermal batteries

Johns Hopkins University Baltimore, MD

Graduate Researcher 2013 – Present

- Synthesize, characterize, and modify polymer matrix nanocomposite using thermal and optical methods
- Developed non-destructive laser ultrasonic methods to measure the elastic moduli of nuclear graphites

Oak Ridge National Lab, Ceramics Science & Technology Oak ridge, TN

Curriculum Vitae

Research Associate 2011 – 2012

- Studied the mechanical properties and fatigue response of piezoceramic multilayer actuators for heavy-duty diesel engine fuel injectors

University of California, Berkeley, MS&E Berkeley, CA

NSF Summer Intern June – Aug. 2010

- Investigated the magnetic behaviors of ferromagnet-antiferromagnet bilayers for spin valve applications

Emory & Henry College, Dept. of Chemistry Emory, VA

Research Assistant 2009 – 2011

- Studied the interface fracture of organosilicate glasses in various corrosive environments to better understand the influence of the package-induced stress on computer chips

Teaching and Leadership Experience

Johns Hopkins University Baltimore, MD

Students Mentor 2013 – 2016

- Mentored high school, undergraduate, and master students

Publications

• **F. W. Zeng**, D. Zhang, J. B. Spicer, Palladium Nanoparticle Formation Processes in Fluoropolymers by Thermal Decomposition of Organometallic Precursors, Physical Chemistry Chemical Physics, 20, 24389 (2018).

Curriculum Vitae

• L. R. Olasov, **F. W. Zeng**, J. B. Spicer, N. C. Gallego, C. I. Contescu, Modeling the effects of oxidation-induced porosity on the elastic moduli of nuclear graphites, Carbon, 141, 304 (2018).

• **F. W. Zeng**, D. Zhang, J. B. Spicer, Effect of Polymer Structure on Precursor Diffusion and Particle Formation in Polymer Matrix Nanocomposites, Journal of Inorganic and Organometallic Polymers and Materials 28, 1850 (2018).

• J. B. Spicer, **F. W. Zeng**, L. R. Olasov, Subsurface, thermoelastic line source excitation of a transversely isotropic half space, Wave Motion 72, 87 (2017).

• **F. W. Zeng**, C. I. Contescu, N. C. Gallego, J. B. Spicer, Theory and application of laser ultrasonic shear wave birefringence measurements to the determination of microstructure orientation in transversely isotropic, polycrystalline graphite materials, Carbon 115, 460 (2017).

• J. B. Spicer, L. R. Olasov, **F. W. Zeng**, K. Han, N. C. Gallego, C. I. Contescu, Laser ultrasonic assessment of the effects of porosity and microcracking on the elastic moduli of nuclear graphites, Journal of Nuclear Materials 471, 80 (2016).

• J. B. Spicer, **F. W. Zeng**, Line source representations for shear wave birefringence measurements in transversely isotropic materials using laser ultrasonics, Wave Motion 61, 1 (2016).

• **F. W. Zeng**, S. M. Gates, M. W. Lane, Corrosion in low dielectric constant Si-O based thin films: Buffer concentration effects, AIP Advances 4, 057112 (2014).

Curriculum Vitae

• **F. W. Zeng**, H. Wang, H-T Lin, Fatigue and failure responses of lead zirconate titanate multilayer actuator under unipolar high-field electric cycling, J. Appl. Phys. 114, 024101 (2013).

• K. Zhang, **F. W. Zeng**, H. Wang, H-T Lin, Biaxial flexural strength of poled lead zirconate titanate under high electric field with extended field range, Ceramics International 39, 2023 (2013).

• K. Zhang, **F. W. Zeng**, H. Wang, H-T Lin, Strength properties of aged poled lead zirconate titanate subjected to electromechanical loadings, Smart Materials Structure 21, 117001 (2012).

Conference Proceedings

• J. B. Spicer, **F. W. Zeng**, N. C. Gallego, C. I. Contescu, Ultrasonics Symposium (IUS), 2017 IEEE International, 1-4.

• **F. W. Zeng**, J. B. Spicer, Nanotechnology (IEEE-NANO), 2017 IEEE 17th International Conference on, 436-438.

• J. B. Spicer, **F. W. Zeng**, N. C. Gallego, C. I. Contescu, CARBON 2016 - The World Conference on Carbon.

• T. J. DeJournett, K. Han, L. R. Olasov, **F. W. Zeng**, B. Lee, J. B. Spicer, Nanoengineering: Fabrication, Properties, Optics, and Devices XII 9556, 95560V.

• **F. W. Zeng**, K. Han, L. R. Olasov, N. C. Gallego, C. I. Contescu, J. B. Spicer, Thermosense: Thermal Infrared Applications XXXVII 9485, 948511.

Curriculum Vitae

• J. B. Spicer, **F. W. Zeng**, K. Han, L. R. Olasov, N. C. Gallego, C. I. Contescu, Ultrasonics Symposium (IUS), 2014 IEEE International, 232-235.

Presentations and Invention

Conference Presentations: six oral presentations at national conferences.

Invention disclosure: **F. W. Zeng**, D. Zhang, J. B. Spicer, 2016, In situ Formation of Nanoparticles in Polymer Matrices: Particle Size Distribution and its Connection to Free Volume of Polymers.